SEARCH FOR AN INFRARED ELECTRO-OPTIC EFFECT IN THIN HIGH TEMPERATURE SUPERCONDUCTING FILMS

By

ANDREW C. WINT

A DISSERTATION PRESENTED TO THE GRADUATE SCHOOL
OF THE UNIVERSITY OF FLORIDA IN PARTIAL FULFILLMENT
OF THE REQUIREMENTS FOR THE DEGREE OF
DOCTOR OF PHILOSOPHY

UNIVERSITY OF FLORIDA

2004

ACKNOWLEDGMENTS

Throughout my time as a graduate student here at the University of Florida, many special people have had a profound impact on my development—both as an experimentalist and as a person. It gives me enormous pleasure to pay homage to those who have challenged, inspired and encouraged me during this exciting period of my academic life.

Firstly, I would like to express my sincere gratitude to my advisor, Professor David B. Tanner, for allowing me to be a part of his research team, and for his belief and confidence in me. I have benefited greatly from his timely advice and his willingness to help whenever his help was needed.

I am also greatly indebted to Professors A. F. Hebard, K. Ingersent, C. J. Stanton and P. Holloway for serving on my supervisory committee.

I would also like to thank my colleagues L. Gasprov, N. Tache, J. Hwang, V. Boychev, A. Ugawa, M. Chen, K. Kamarás, C.D. Porter, K. Woo, M. Nikolou, H. Tashiro, N. Margankunte, H. Zhang, V. Long, L. Booshehri and N. Nemes for their insightful discussions and inspiration during my graduate work.

It is my great pleasure to thank Conductus for supplying the thin $YBa_2Cu_3O_{6+x}$ films on sapphire substrates, and Z. Zhang and R. Hadfield for supplying similar films on magnesium oxide substrates which were used in this work.

I would also like to acknowledge the technical staff at the machine shop, electronics shop and cryogenics lab who were always very helpful.

It would be remiss of me not to mention the two most important people, my parents, whose selfless sacrifice, love and encouragement have made it possible for me to be here doing this work.

Finally, I would like to thank the NSF(Grant No. CTS-0082969) for its financial support of this project.

TABLE OF CONTENTS

page

ACKNOWLEDGMENTS ii

ABSTRACT vi

CHAPTER

1 INTRODUCTION 1

2 OPTICAL THEORY 4

2.1 Introduction 4
2.2 Linear Isotropic Homogeneous Conducting Media 4
2.2.1 Wave Propagation 4
2.2.2 Extraction of Optical Constants 7
2.3 Stratified Media 11
2.4 Anisotropic Media 14
2.5 Drude-Lorentz Model 20
2.6 Sum Rules 21

3 INTERFEROMETRIC SPECTROSCOPY 23

3.1 Introduction 23
3.2 Basic Theory 23
3.2.1 Interferogram and Spectrum 24
3.2.2 Truncation and Apodization 26
3.2.3 Sampling 27
3.2.4 Phase Errors 28
3.2.5 Noise 29
3.3 Bruker 113v Spectrometer 32

4 INFRARED PROPERTIES OF HIGH-T_c SUPERCONDUCTORS . . . 37

4.1 Introduction 37
4.2 Generic Trends 38
4.2.1 Normal State Phase Diagram 38
4.2.2 Crystal Structure 38
4.2.3 Doping Effects 39
4.2.4 Optical Anisotropy 40
4.3 Models of Optical Conductivity 41
4.3.1 Two-Component Model 42

4.3.2 One-Component Models . . . 43
4.4 Superconducting State Electrodynamics . . . 45
4.5 Survey of Experimental Results . . . 47
4.5.1 Doping Dependence of Optical Constants . . . 47
4.5.2 Midinfrared Band . . . 49
4.5.3 Relaxation Rate . . . 50
4.5.4 One-Component Analysis . . . 51
4.5.5 c-Axis Conductivity . . . 52
4.6 Conclusion . . . 54

5 SAMPLE PREPARATION AND EXPERIMENTAL TECHNIQUES . . 56

5.1 Introduction . . . 56
5.2 $YBa_2Cu_3O_{6+x}$ Film on MgO . . . 56
5.3 $YBa_2Cu_3O_{6+x}$ Films on Sapphire . . . 57
5.4 Experiment . . . 58
5.4.1 Cryogenic Apparatus . . . 58
5.4.2 Reflectivity Measurements . . . 59
5.4.3 Transmittance Measurements . . . 60

6 FAR-INFRARED STUDIES OF $YBa_2Cu_3O_{6+x}$ FILMS . . . 66

6.1 Introduction . . . 66
6.2 Results and Discussion . . . 67
6.2.1 MgO Substrate . . . 67
6.2.2 Sapphire Substrate . . . 68
6.2.3 $YBa_2Cu_3O_{6+x}$ on MgO . . . 71
6.2.4 $YBa_2Cu_3O_{6+x}$ on Sapphire . . . 72
6.2.5 Two-Fluid Model . . . 73
6.2.6 Free Carrier Relaxation and Condensate . . . 75
6.3 Summary . . . 77

7 FAR-INFRARED ELECTRO-OPTIC STUDIES OF $YBa_2Cu_3O_{6+x}$ FILMS 92

7.1 Introduction . . . 92
7.2 Results and Discussion . . . 93
7.2.1 Electro-optic Transmittance of Film on MgO . . . 93
7.2.2 Electro-optic Transmittance of Film on Sapphire . . . 95
7.2.3 Two-Fluid Simulations . . . 100
7.2.4 Current Density Distributions in Superconducting Thin Films . . . 105
7.3 Summary . . . 111

8 CONCLUSION . . . 113

REFERENCES . . . 116

BIOGRAPHICAL SKETCH . . . 122

Abstract of Dissertation Presented to the Graduate School
of the University of Florida in Partial Fulfillment of the
Requirements for the Degree of Doctor of Philosophy

SEARCH FOR AN INFRARED ELECTRO-OPTIC
EFFECT IN THIN HIGH TEMPERATURE
SUPERCONDUCTING FILMS

By

Andrew C. Wint

December 2004

Chair: David B. Tanner
Major Department: Physics

Infrared spectroscopy is used to investigate the effect of transport currents on the ab-plane superconducting state properties of thin c-axis oriented $YBa_2Cu_3O_{6+x}$ films on sapphire and magnesium oxide substrates.

The films were first characterized in both the normal and superconducting states, through optical reflectivity and transmittance measurements over a wide frequency range (40–350 cm^{-1}) in the far-infrared. We observed fairly high reflectivity and low transmittance in the superconducting state at frequencies below 150 cm^{-1}. This is in contrast to the lower reflectivities and higher transmittances which are observed in the normal state over the same frequency range.

It is well known from nonlinear transport studies on thin superconducting films below their transition temperature, T_c, that large currents exceeding the critical current I_c destroy superconductivity, triggering a transition to the ohmic lossy regime typical of the normal state. We studied the effect of transport currents on the superconducting state transmittance in the far infrared region below 350 cm^{-1}.

The first set of spectra was taken at 75 K— about 10 K below T_c for both films— and a set of spectra was also taken at low temperature (40 K) for the film on sapphire substrate.

The films on magnesium oxide showed no electro-optic response up to very high currents, while at high currents, the film on sapphire showed an increase in transmittance at low frequency accompanied by a suppression of the transmittance at higher frequencies. At lower temperature a similar effect is observed in the film on sapphire, even at currents much lower than the critical value. We believe the changes observed are spurious, and may be attributed to ohmic heating. This has been further verified by simulations of the dielectric response using a simple two-fluid model of the superconducting state with a current dependent superfluid oscillator strength.

CHAPTER 1
INTRODUCTION

High temperature superconductivity (HTSC) in the layered cuprates has been a central issue of contemporary condensed matter physics for more than 17 years [1]. These materials are interesting not only because of their novel electronic properties, but also because of the enormous potential which exists for fabricating many practical devices incorporating them. Infrared, microwave, terahertz and optical spectroscopies have been used to study the nature of charge transfer, the dynamics of free carriers, phonons, the Josephson plasma resonance and many other collective phenomena which are observed in this class of compounds [2, 3]. Despite considerable effort by theorists and experimentalists alike, the pairing mechanism responsible for HTSC in these materials still remains a mystery.

High temperature superconductors appear to be attractive candidates for the fabrication of optical modulators which are used in fiber optic communications. At present, fiber optic transmission rates are limited by the rate at which optical data can be modulated. The current modulation techniques which include direct modulation, electro-absorption modulation, and Mach Zender modulation, limit the transmission rates to about 40 Gbit per second. Direct and electro-absorption modulation are limited by the carrier mobility of gallium arsenide (GaAs). The modulation rate of Mach-Zender modulators is limited by the difficulties in producing rapid high voltage pulses required to switch the electro-optic lithium niobiate ($LiNbO_3$) material used in these modulators. HTSC can easily be switched from a superconducting state to a resistive state by passing a critical amount of current. The resistive state is characterized by high transmission at far infrared frequencies, as compared to the opaque superconducting state. It is believed that

the rate of switching may be as high as a terabit per second. This high rate of switching would vastly improve the transmission rate of current modulators in fiber optic networks.

Another figure of merit of any optical modulator is its extinction ratio. The extinction ratio for a superconducting modulator is the ratio of transmitted light in the resistive state to the transmitted light in the superconducting state. It will be shown that a superconducting modulator based on HTSC films offers no advantage over the current modulators which are available commercially.

This dissertation describes a semi-systematic study of the effects of transport current on the far infrared transmittance spectra of thin superconducting $YBa_2Cu_3O_{6+x}$ films. I have confined the investigations to transmittance measurements below 350 cm^{-1}. There are two main reasons for this. The first is because the effect of the dephasing and subsequent weakening of superconducting order is expected to be seen in the far infrared region. Secondly, the changes are expected to be quite small and optical transmittance is far more sensitive than reflectivity to such small changes.

The next section gives a brief description of the organization of the remaining chapters of this treatise.

This dissertation consists of eight chapters including the introduction. I have tried to organize the chapters in a logical sequence, so that all the concepts needed are easily accessible.

Chapter 2 describes the basic optical theory of the propagation of light through optical media. I shall discuss the various techniques which are used to extract the optical constants of a material from measurements of optical reflectivity and or transmittance. Chapter 3 gives a discussion of the basic theory of interferometric spectroscopy and a description of the interferometer used in this work. A review of our current understanding of the electrodynamics of high

T_c superconductors, both in the normal and superconducting states, is given in chapter 4, where various models used to analyze optical data are introduced.

A brief description of the film preparation techniques and their characterization by a standard 4-probe method is presented in chapter 5. Chapter 6 deals with the results of the optical reflectivity and transmittance measurements and the extracted optical constants for the thin $YBa_2Cu_3O_{6+x}$ films used in this work. In chapter 7 I present the results of electrooptic measurements in the superconducting state of the same films used in chapter 6. The difficulties encountered in interpreting the data are discussed. Finally, chapter 8 concludes this dissertation with a review of the results.

CHAPTER 2
OPTICAL THEORY

2.1 Introduction

The response of a medium to an external oscillatory electromagnetic field is quantified by its complex frequency-dependent response functions. The most commonly used response functions in infrared spectroscopy are the complex conductivity $\tilde{\sigma}(\omega) = \sigma_1(\omega) + i\sigma_2(\omega)$, the complex dielectric function $\tilde{\epsilon}(\omega) = \epsilon_1(\omega) + i\epsilon_2(\omega)$ and the complex index of refraction $\tilde{N}(\omega) = n(\omega) + i\kappa(\omega)$. Any of these complex functions gives a complete description of the absorptive and dispersive nature of the interaction of light and matter. They may easily be extracted from optical reflectivity and/or transmittance of the material as a function of the energy of incident light. The next few sections of this chapter describe how these functions arise in a natural way from the formal theory of the interaction of light with matter. I shall present the theory as applied to both isotropic and anisotropic birefringent media where the functions take the form of tensors.

2.2 Linear Isotropic Homogeneous Conducting Media

This section describes the propagation of light through a linear isotropic homogenous conducting medium [4, 5]. I will also introduce the relevant equations for the reflectivity from and transmittance across a boundary formed between two such semi-infinite media.

2.2.1 Wave Propagation

The propagation of light through a medium is based on two fundamental but equally important sets of equations. The first more fundamental set is the macroscopic Maxwell equations. The validity of these equations is based on the

assumption that the wavelength of light far exceeds the dimensions of the unit cell of the material involved. An assumption of this type is usually satisfied in most cases over the entire range of interest in the infrared region 20 to 45,000 wavenumbers (20–45,000 cm^{-1}). In Gaussian units the Maxwell equations in differential form are given by

$$\nabla \cdot \boldsymbol{D} = 4\pi\rho_f \tag{2.1}$$

$$\nabla \cdot \boldsymbol{B} = 0 \tag{2.2}$$

$$\nabla \times \boldsymbol{E} = -\frac{1}{c}\frac{\partial \boldsymbol{B}}{\partial t} \tag{2.3}$$

$$\nabla \times \boldsymbol{H} = \frac{4\pi}{c}\boldsymbol{J}_f + \frac{1}{c}\frac{\partial \boldsymbol{D}}{\partial t} \tag{2.4}$$

where $\boldsymbol{E}$ and $\boldsymbol{D}$ are the electric field and electric displacement, $\boldsymbol{B}$ and $\boldsymbol{H}$ are the magnetic induction and magnetic field, c is the speed of light in free space and ρ_f and $\boldsymbol{J}_f$ are the free charge and free current densitiy. The second set of equations are the linear constitutive relations between the field vectors given by

$$\boldsymbol{D} = \epsilon_1 \boldsymbol{E} \qquad \boldsymbol{B} = \mu \boldsymbol{H} \qquad \boldsymbol{J}_f = \sigma_1 \boldsymbol{E} \tag{2.5}$$

where ϵ_1 and σ_1 are the frequency dependent dielectric constant and conductivity of the material respectively while μ is the complex permeability of the material which describes its magnetic properties. These relations assume that the electrodynamics of the medium are local. By using the linear constitutive relations in Maxwell's equations and eliminating $\boldsymbol{D}$ and $\boldsymbol{B}$ Maxwell's equations take the form:

$$\nabla \cdot \boldsymbol{E} = \frac{4\pi}{\epsilon_1}\rho_f \tag{2.6}$$

$$\nabla \cdot \boldsymbol{H} = 0 \tag{2.7}$$

$$\nabla \times \boldsymbol{E} = \frac{\mu}{c}\frac{\partial \boldsymbol{H}}{\partial t} \tag{2.8}$$

$$\nabla \times \boldsymbol{H} = \frac{4\pi}{c}\sigma_1 \boldsymbol{E} + \frac{\epsilon_1}{c}\frac{\partial \boldsymbol{E}}{\partial t}. \tag{2.9}$$

In the absence of free charge (2.6), (2.8), and (2.9) after the elimination of $\boldsymbol{H}$ give the wave equation for $\boldsymbol{E}$,

$$\boldsymbol{\nabla^2 E} = \frac{\mu\epsilon_1}{c^2}\frac{\partial^2 \boldsymbol{E}}{\partial^2 t} + \frac{4\pi\mu\sigma_1}{c^2}\frac{\partial \boldsymbol{E}}{\partial t}. \tag{2.10}$$

Consider a monochromatic plane wave of angular frequency ω and wavevector $\boldsymbol{q}$ given by

$$\left\{ \begin{array}{c} \boldsymbol{E} \\ \boldsymbol{H} \end{array} \right\} = \left\{ \begin{array}{c} \boldsymbol{E}_o \\ \boldsymbol{H}_o \end{array} \right\} \exp[i(\boldsymbol{q}\cdot\boldsymbol{r} - \omega t)] \tag{2.11}$$

where $\boldsymbol{E}_o$ and $\boldsymbol{H}_o$ are complex vector amplitudes. Upon substitution of these expressions into Maxwell's equations we obtain the following results, in the absence of free space charges:

$$\boldsymbol{q}\cdot\boldsymbol{E} = 0 \tag{2.12}$$

$$\boldsymbol{q}\cdot\boldsymbol{H} = 0 \tag{2.13}$$

$$\boldsymbol{q}\times\boldsymbol{E} = \frac{\omega\mu}{c}\boldsymbol{H} \tag{2.14}$$

$$i\boldsymbol{q}\times\boldsymbol{H} = -i\frac{\omega}{c}\boldsymbol{E} + \frac{4\pi}{c}\left[\sigma_1 + i\frac{\omega}{4\pi}(1-\epsilon_1)\right]\boldsymbol{E} = \frac{4\pi}{c}[\boldsymbol{J}_d + \boldsymbol{J}_f + \boldsymbol{J}_p] \tag{2.15}$$

where Eqns. (2.12), (2.13) and (2.14) indicate that the vectors $\boldsymbol{E}$, $\boldsymbol{H}$ and $\boldsymbol{q}$ form an orthogonal triplet, while $\boldsymbol{J}_d$, $\boldsymbol{J}_f$ and $\boldsymbol{J}_p$ represent the displacement, free and polarization currents respectively in Eqn. (2.15). It follows from the latter equation that the properties of the medium can easily be described by a complex conductivity $\tilde{\sigma}(\omega) = \sigma_1(\omega) + i\sigma_2(\omega)$ where $\sigma_2(\omega) = \omega(1-\epsilon_1(\omega))/4\pi$ or complex dielectric function $\tilde{\epsilon}(\omega) = \epsilon_1(\omega) + i\epsilon_2(\omega)$ where $\epsilon_2(\omega) = 4\pi\sigma_1(\omega)/\omega$. It follows that Eqn. (2.15) may be rewritten in terms of these complex functions as

$$i\boldsymbol{q}\times\boldsymbol{H} = -i\frac{\omega}{c}\tilde{\epsilon}\boldsymbol{E} = -i\frac{\omega}{c}\boldsymbol{E} + \frac{4\pi}{c}\tilde{\sigma}\boldsymbol{E} \tag{2.16}$$

After combining (2.16) with (2.14) assuming nonmagnetic media for which $\mu = 1$ we obtain the relation $q^2 = (\frac{\omega}{c})^2\tilde{\epsilon}$. It is easy enough to define a complex refractive

index $\tilde{N}$ which leads to the dispersion relation:

$$q = \frac{\omega}{c}\tilde{N} = \frac{\omega}{c}(n + i\kappa) = \frac{\omega}{c}\sqrt{\tilde{\epsilon}}. \tag{2.17}$$

The field amplitudes of $\boldsymbol{E}$ and $\boldsymbol{H}$ are then related by

$$H = \sqrt{\tilde{\epsilon}}E = \tilde{N}E. \tag{2.18}$$

Whenever a plane wave is incident normally on a conducting medium both $\boldsymbol{E}$ and $\boldsymbol{H}$ are attenuated as $e^{-\frac{\omega}{c}\kappa r}e^{i(\frac{\omega}{c}nr-\omega t)}$. This is a damped wave with a skin depth $\delta = c/\omega\kappa$. Since the power dissipated per unit volume is proportional to the square of the field amplitude, the corresponding length scale for power loss is the absorption coefficient $\alpha = 2\omega\kappa/c = 2/\delta$.

Finally the power flux or average rate of flow of energy per unit area given by the Poynting vector,

$$\langle \boldsymbol{S} \rangle = \frac{c}{8\pi}\Re(\boldsymbol{E} \times \boldsymbol{H}^*) \tag{2.19}$$

which is parallel to the wave vector $\boldsymbol{q}$ of the wave for an isotropic medium. The physical significance of the real part of the optical conductivity σ_1 can easily be seen from the relation for the power dissipated per unit volume. Using Ohm's law we can see that the power dissipated per unit volume is given by

$$\frac{dP}{dV} = \frac{1}{2}\Re(\boldsymbol{J} \cdot \boldsymbol{E}^*) = \frac{1}{2}\Re\{\sigma\boldsymbol{E} \cdot \boldsymbol{E}^*\} = \frac{1}{2}\sigma_1 \mid \boldsymbol{E} \mid^2 . \tag{2.20}$$

The real part of the conductivity is thus a measure of the absorptive properties of the medium.

2.2.2 Extraction of Optical Constants

In many cases the first step towards the extraction of the optical constants of a material involves measuring the optical reflectivity $\mathcal{R}(\omega)$ of a thick single crystal. Here, the material is thick enough that all light incident upon it is either totally reflected or absorbed with little or no transmission (i.e., the crystal is thicker than

the penetration depth δ). The difficulty encountered is that the reflectivity is desired over the entire frequency from $\omega = 0$ to $\omega = \infty$, so that Kramers-Kronig analysis can be carried out. This section concentrates on the extraction of the frequency dependent optical constants from the optical reflectivity measured over a wide frequency range on thick single crystals at normal incidence. For the sake of brevity we shall not consider the corresponding formalism which deals with light incident on a material at oblique incidence, since normal incidence is always assumed in all cases in this work.

Consider a plane wave in medium 1 with a complex index $\tilde{N}_1$ which is incident normally on the boundary between itself and a second linear isotropic conducting medium of complex index $\tilde{N}_2$. Let (E_i, H_i),(E_r, H_r) and (E_t, H_t) represent the incident, reflected and transmitted electric and magnetic field amplitudes at the boundary respectively— which are all parallel to the surface. The boundary conditions mandate that the resultant electric and magnetic fields at the boundary be continuous in the absence of surface currents. We have the following equations:

$$\begin{aligned} E_i + E_r &= E_t \\ H_i - H_r &= H_t. \end{aligned} \tag{2.21}$$

From the relation between E and H given in equation (2.18) it is easy to write the second equation in (2.21) in terms of E and the refractive indices using

$$\begin{aligned} H_i &= \tilde{N}_1 E_i \\ H_r &= \tilde{N}_1 E_r \\ H_t &= \tilde{N}_2 E_t. \end{aligned} \tag{2.22}$$

This allows us to calculate the complex amplitude reflection coefficients for the reflected and transmitted fields, and hence the fraction of the incident power which

is reflected and transmitted. The amplitude reflection coefficients are given by

$$\begin{aligned} \tilde{r} &= \frac{E_r}{E_i} = \frac{\tilde{N}_1 - \tilde{N}_2}{\tilde{N}_1 + \tilde{N}_2} = r(\omega)e^{i\phi_r(\omega)} \\ \tilde{t} &= \frac{E_t}{E_i} = \frac{2\tilde{N}_1}{\tilde{N}_1 + \tilde{N}_2}. \end{aligned} \tag{2.23}$$

The first equation in (2.23) is written in exponential form in terms of a frequency dependent amplitude and phase—the significance of this will be explained later. In the laboratory the actual measured quantity is the reflectivity $\mathcal{R}(\omega)$ or the fraction of the incident power reflected where medium 1 is free space with $\tilde{N}_1 = 1$ and medium 2 has index $\tilde{N}_2 = n + i\kappa$. The observed laboratory reflectivity is given by

$$\mathcal{R}(\omega) = \tilde{r}\tilde{r}^* = r(\omega)^2 = \frac{(1-n^2)+\kappa^2}{(1+n^2)+\kappa^2}. \tag{2.24}$$

It is possible now to rewrite the first equation in (2.23) in terms of the reflectivity $\mathcal{R}(\omega)$, the phase change upon reflection $\phi(\omega)$, and the complex refractive index on reflection.Then (2.23) becomes

$$\sqrt{\mathcal{R}}e^{i\phi} = \tilde{r} = \frac{(1-n)-i\kappa}{(1+n)+i\kappa} \tag{2.25}$$

where

$$\tan\phi = -\frac{2\kappa}{1-n^2-\kappa^2}. \tag{2.26}$$

The reflectivity $\mathcal{R}(\omega)$ and phase $\phi(\omega)$ are related through causality by the Kramers-Kronig relations [6, 7]

$$\phi(\omega) = \frac{\omega}{\pi}\int_0^\infty \frac{\ln\mathcal{R}(\omega) - \ln\mathcal{R}(\omega')}{\omega'^2 - \omega^2}\,\mathrm{d}\omega' \tag{2.27}$$

or

$$\phi(\omega) = \frac{1}{2\pi}\int_0^\infty \ln\left|\frac{\omega'-\omega}{\omega'+\omega}\right| \frac{d\ln\mathcal{R}(\omega')}{d\omega'}\,\mathrm{d}\omega'. \tag{2.28}$$

The final result is that once $\mathcal{R}(\omega)$ and $\phi(\omega)$ are known its is easy enough to invert eqn. (2.25) to obtain $n(\omega)$ and $\kappa(\omega)$ which gives

$$n(\omega) = \frac{1 - \mathcal{R}(\omega)}{1 + \mathcal{R}(\omega) - 2\sqrt{\mathcal{R}(\omega)}\cos\phi(\omega)} \tag{2.29}$$

$$\kappa(\omega) = \frac{2\sqrt{\mathcal{R}(\omega)}\sin\phi(\omega)}{1 + \mathcal{R}(\omega) - 2\sqrt{R(\omega)}\cos\phi(\omega)} \tag{2.30}$$

We may also define the transmittance across a boundary between two semi-infinite media of complex indices $\tilde{N}_1$ and $\tilde{N}_2$. The fraction of the incident power transmitted across the boundary, for light incident from a medium 1 with complex index $\tilde{N}_1$ and passing into a medium $\tilde{N}_2$ is the transmittance

$$\mathcal{T}(\omega) = \frac{|\tilde{N}_2|}{|\tilde{N}_1|}|\tilde{t}^2| = \frac{4|\tilde{N}_1||\tilde{N}_2|}{|\tilde{N}_1 + \tilde{N}_2|^2}. \tag{2.31}$$

Eqns. (2.17) provide useful relationships between the different optical constants

$$\begin{aligned} \epsilon_1 &= n^2 - \kappa^2, \\ \epsilon_2 &= 2n\kappa, \\ \sigma_1 &= \omega\epsilon_2/4\pi, \\ \sigma_2 &= \omega(1 - \epsilon_1)/4\pi, \\ \delta &= c/\omega\kappa, \\ \alpha &= 2\omega\kappa/c. \end{aligned} \tag{2.32}$$

We have discussed the use of Kramers-Kronig analysis to extract the optical constants of a thick single crystal provided the optical reflectivity is known over a broad frequency range. The reflectivity as measured in the laboratory is usually only known over a finite frequency range, and various extrapolations of the reflectivity are usually employed at the high and low frequency ends of the reflectivity spectra. These extrapolations usually introduce errors in the optical constants extracted using this technique. A further difficulty involves the fact that thick single crystals are not always available, and the optical reflectivity under such

circumstances cannot be used along with the Kramers-Kronig analysis to extract the needed optical constants. The next section briefly deals with the theory of stratified media which is more relevant to the current work which deals with thin films on transparent substrates.

2.3 Stratified Media

A stratified medium is any medium whose optical properties are constant throughout each plane perpendicular to a particular direction [8]. A common example of stratified media is multilayers which are formed from a succession of thin plane parallel films. The analysis of the optical characteristics of stratified media is very different from that of thick single crystals which was discussed previously. In this section the basic theory of the optical response of stratified media will be presented.

Consider a single layer of thickness d and complex refractive index $\tilde{N}_2$ nested between two semi-infinite media of indices $\tilde{N}_1$ and $\tilde{N}_3$ (Figure 2–1). Light is incident normally from the left. The amplitudes of the incident, reflected and transmitted electric fields are E_1, E_1' and E_3 respectively. The corresponding magnetic fields (not shown in the diagram) point in such a way that the Poynting vectors of the various waves point in the directions of their wavevectors $\mathbf{q}$ in the diagram. The fields E_2 and E_2' are the resultant electric fields of the forward and backward travelling waves in the medium.

The electric and magnetic vectors are parallel to both interfaces of the layer. The boundary conditions require the resultant tangential electric and magnetic fields at each interface to be continuous. At the left interface the boundary conditions give

$$\begin{aligned} \text{Electric}: \quad E_1 + E_1' &= E_2 + E_2' \\ \text{Magnetic}: \quad \tilde{N}_1 E_1 - \tilde{N}_1 E_1' &= \tilde{N}_2 E_2 - \tilde{N}_2 E_2'. \end{aligned} \tag{2.33}$$

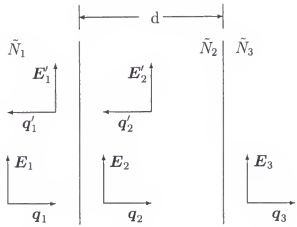

Figure 2–1: The resultant electric fields and their associated wavevectors of a plane wave incident normally on a single layer of thickness d.

Similarly at the right interface the boundary conditions give

$$\begin{aligned} \text{Electric}: \quad & E_2 e^{iq_2 d} + E_2' e^{-iq_2 d} &&= E_3 \\ \text{Magnetic}: \quad & \tilde{N}_2 E_2 e^{iq_2 d} - \tilde{N}_2 E_2' e^{-iq_2 d} &&= \tilde{N}_3 E_3. \end{aligned} \tag{2.34}$$

Here the complex wave vector $q_2 = (2\pi/\lambda_0)\tilde{N}_2$; where λ_0 is the free space wavelength. In order to simplify the notation I shall denote the complex phase shift $q_2 d$ by δ_2. After eliminating the amplitudes E_2 and E_2' we can rewrite the remaining two equations in matrix form as

$$\begin{bmatrix} 1 \\ \tilde{N}_1 \end{bmatrix} + \begin{bmatrix} 1 \\ -\tilde{N}_1 \end{bmatrix} \frac{E_1'}{E_1} = \begin{bmatrix} \cos\delta_2 & -\dfrac{i}{\tilde{N}_2}\sin\delta_2 \\ -i\tilde{N}_2 \sin\delta_2 & \cos\delta_2 \end{bmatrix} \begin{bmatrix} 1 \\ \tilde{N}_3 \end{bmatrix} \frac{E_3}{E_1}. \tag{2.35}$$

Eqn. (2.34) maybe rewritten in a more compact form as

$$\begin{bmatrix} 1 \\ \tilde{N}_1 \end{bmatrix} + \begin{bmatrix} 1 \\ -\tilde{N}_1 \end{bmatrix} r = \mathsf{M}_2 \begin{bmatrix} 1 \\ \tilde{N}_3 \end{bmatrix} t. \tag{2.36}$$

The reflection coefficient is

$$r = \frac{E_1'}{E_1} \tag{2.37}$$

and the transmission coefficient is given by

$$t = \frac{E_3}{E_1}. \tag{2.38}$$

The matrix M_2 is known as the transfer matrix

$$\mathsf{M}_2 = \begin{bmatrix} \cos\delta_2 & \frac{-i}{\tilde{N}_2}\sin\delta_2 \\ -i\tilde{N}_2\sin\delta_2 & \cos\delta_2 \end{bmatrix}. \tag{2.39}$$

The elements of this matrix are functions of the complex refractive index of the layer $\tilde{N}_2$ and the layer thickness d.

It is easy enough to generalize this formulation to a case where there are N layers numbered $2, 3, 4, \ldots N+1$ with complex indices $\tilde{N}_2, \tilde{N}_3, \tilde{N}_4, \ldots \tilde{N}_{N+1}$ and thicknesses $d_2, d_3, d_4, \ldots d_{N+1}$. This forms a multilayer whose transfer matrix is the product of the transfer matrices of the individual layers. By applying the boundary conditions at each interface it can be shown that the multilayer satisfies a similar matrix equation which becomes

$$\begin{bmatrix} 1 \\ \tilde{N}_1 \end{bmatrix} + \begin{bmatrix} 1 \\ -\tilde{N}_1 \end{bmatrix} r = \mathsf{M}_2\mathsf{M}_3\mathsf{M}_4\cdots\mathsf{M}_{N+1} \begin{bmatrix} 1 \\ \tilde{N}_{N+2} \end{bmatrix} t = \mathsf{M} \begin{bmatrix} 1 \\ \tilde{N}_{N+2} \end{bmatrix} t; \tag{2.40}$$

where the M_is are the various transfer matrices of the layers and M is their product. The matrix M completely characterizes the optical response of the multilayer and gives an expression for the amplitude reflection and transmission coefficients of a multilayer. If we denote the elements of the transfer matrix M of the multilayer by A, B, C, and D respectively such that

$$\mathsf{M}_2\mathsf{M}_3\mathsf{M}_4\cdots\mathsf{M}_{N+1} = \mathsf{M} = \begin{bmatrix} A & B \\ C & D \end{bmatrix}, \tag{2.41}$$

then the reflection and transmission coefficients become

$$r = \frac{\tilde{N}_1 A + \tilde{N}_{N+2}\tilde{N}_1 B - C - \tilde{N}_{N+2} D}{\tilde{N}_1 A + \tilde{N}_{N+2}\tilde{N}_1 B + C + \tilde{N}_{N+2} D} \tag{2.42}$$

$$t = \frac{2\tilde{N}_1}{\tilde{N}_1 A + \tilde{N}_{N+2}\tilde{N}_1 B + C + \tilde{N}_{N+2} D}. \tag{2.43}$$

The reflectivity $\mathcal{R}(\omega)$ and transmittance $\mathcal{T}(\omega)$ then become

$$\mathcal{R}(\omega) = rr^* = |r|^2 \tag{2.44}$$

and

$$\mathcal{T}(\omega) = \left|\frac{\tilde{N}_{N+2}}{\tilde{N}_1}\right| tt^* = \left|\frac{\tilde{N}_{N+2}}{\tilde{N}_1}\right| |t|^2. \tag{2.45}$$

These equations are quite complicated even for a single layer. If the optical constants of $N-1$ layers are accurately known for an N layer system, it is not possible to analytically invert these equations if we know the reflectivity and transmittance over the same frequency range. It is possible however to invert the reflectivity and transmittance of a single layer using the technique outlined in [9].

2.4 Anisotropic Media

The first part of this chapter dealt with linear isotropic homogeneous media; where, Maxwell's equations combined with the linear constitutive relations allowed wave solutions in the media. The media were assumed to be isotropic so that the optical excitations were independent of the direction of the electric field in the crystal and the vectors $\boldsymbol{D}$ and $\boldsymbol{E}$ were parallel. We now consider the case where the medium is electrically anisotropic so that $\boldsymbol{D}$ and $\boldsymbol{E}$ are not necessarily parallel [10].

We begin with Maxwell's equations for a conducting medium:

$$\nabla \times \boldsymbol{H} = \frac{4\pi}{c}\boldsymbol{J}_f + \frac{1}{c}\frac{\partial \boldsymbol{D}}{\partial t}, \qquad \nabla \times \boldsymbol{E} = -\frac{1}{c}\frac{\partial \boldsymbol{B}}{\partial t}, \tag{2.46}$$

and consider the propagation of a monochromatic damped plane wave of frequency ω and wave vector $\boldsymbol{q} = \omega(\tilde{N}/c)\hat{\boldsymbol{s}}$. Here $\tilde{N}$ represents the complex refractive index of the medium, and $\hat{\boldsymbol{s}}$ represents the unit vector in the wave normal direction. The complex field vectors $\boldsymbol{E}$, $\boldsymbol{D}$, $\boldsymbol{H}$, $\boldsymbol{B}$, and $\boldsymbol{J}$ vary as,

$$\exp\left[i\omega\left(\frac{\tilde{N}}{c}\boldsymbol{r}\cdot\hat{\boldsymbol{s}} - t\right)\right].$$

Substituting this result into Eqn. (2.45) gives

$$\tilde{N}\hat{\boldsymbol{s}}\times\boldsymbol{H} = -\boldsymbol{D} + \frac{4\pi}{i\omega}\boldsymbol{J}_f, \qquad \tilde{N}\hat{\boldsymbol{s}}\times\boldsymbol{E} = \boldsymbol{B} \tag{2.47}$$

We can easily eliminate $\boldsymbol{H}$ from Eqns. (2.46) using the constitutive equation $\boldsymbol{B} = \mu\boldsymbol{H}$, so that we get

$$\mu\left[\boldsymbol{D} + \frac{4\pi i}{\omega}\boldsymbol{J}_f\right] = \tilde{N}^2[\boldsymbol{E} - \hat{\boldsymbol{s}}(\hat{\boldsymbol{s}}\cdot\boldsymbol{E})] \tag{2.48}$$

For an arbitrary choice of orthogonal cartesian axes in an anisotropic crystal, the components of the electric displacement vector $\boldsymbol{D}$ and the electric field vector $\boldsymbol{E}$ are connected by a dielectric tensor ϵ_{ij}; while the components of the free current density $\boldsymbol{J}_f$ are related to the $\boldsymbol{E}$ field components by a conductivity tensor σ_{ij}. In the linear regime the constitutive relations become

$$\left.\begin{aligned} D_x &= \epsilon_{xx}E_x + \epsilon_{xy}E_y + \epsilon_{xz}E_z, \\ D_y &= \epsilon_{yx}E_x + \epsilon_{yy}E_y + \epsilon_{yz}E_z, \\ D_z &= \epsilon_{zx}E_x + \epsilon_{zy}E_y + \epsilon_{zz}E_z, \end{aligned}\right\} \tag{2.49}$$

and

$$\left.\begin{aligned} J_x &= \sigma_{xx}E_x + \sigma_{xy}E_y + \sigma_{xz}E_z, \\ J_y &= \sigma_{yx}E_x + \sigma_{yy}E_y + \sigma yzE_z, \\ J_z &= \sigma_{zx}E_x + \sigma_{zy}E_y + \sigma_{zz}E_z. \end{aligned}\right\} \tag{2.50}$$

The nine quantities ϵ_{xx}, ϵ_{xy}, ... are constants of the medium and constitute the dielectric tensor while the constants σ_{xx}, σ_{xy}, ... form the conductivity tensor.

These relations take a simple form if we use principal axes where the tensors are diagonal. The principal axes of both tensors coincide for crystals of higher symmetry classes (of at least orthorhombic symmetry). The constitutive equations then take the simple form

$$\left.\begin{aligned} D_x = \epsilon_x E_x, \quad D_y = \epsilon_y E_y, \quad D_z = \epsilon_z E_z, \\ J_x = \sigma_x E_x, \qquad J_y = \sigma_y, \quad J_z = \sigma_z E_z. \end{aligned}\right\} \tag{2.51}$$

After substituting eqn. (2.50) into eqn. (2.47) and introducing a set of complex dielectric constants

$$\tilde{\epsilon}_j = \epsilon_j + \frac{4\pi i}{\omega}\sigma_j \qquad (j = x, y, z) \tag{2.52}$$

(2.47) gives

$$E_j = \frac{\tilde{N}^2 s_j (\boldsymbol{E} \cdot \hat{\boldsymbol{s}})}{\tilde{N}^2 - \mu\tilde{\epsilon}_j}. \tag{2.53}$$

Equation (2.52) represents a set of linear homogeneous equations in E_j which have a non trivial solution if the complex refractive index $\tilde{N}$, the components of the complex dielectric constant $\tilde{\epsilon}_j$, and the components of the vector $\hat{\boldsymbol{s}}$ satisfy Fresnel's equation,

$$\frac{s_x^2}{\frac{1}{\tilde{N}^2} - \frac{1}{\mu\tilde{\epsilon}_x}} + \frac{s_y^2}{\frac{1}{\tilde{N}^2} - \frac{1}{\mu\tilde{\epsilon}_y}} + \frac{s_z^2}{\frac{1}{\tilde{N}^2} - \frac{1}{\mu\tilde{\epsilon}_z}} = 0. \tag{2.54}$$

Let us now consider the case of a uniaxial crystal. Such a crystal has an optical axis which lies along a direction of high symmetry. The optical axis is one of the principal axes of the crystal. Since the crystal is uniaxial all other orthogonal axes which lie in a plane normal to it are optically equivalent. A transverse wave whose electric field is polarized parallel to this axis travels as an *e*-wave. Similarly a transverse wave whose electric field is polarized perpendicular to the optic axis travels as an *o*-wave. Let us choose the z-axis of our cartesian coordinate system to

lie along the optic axis, then for a uniaxial crystal we have

$$\begin{aligned} \tilde{\epsilon}_z &= \tilde{\epsilon}_e = \tilde{N}_e^2 \qquad (e\text{-wave}) \\ \tilde{\epsilon}_x = \tilde{\epsilon}_y &= \tilde{\epsilon}_o = \tilde{N}_o^2 \qquad (o\text{-wave}) \end{aligned} \tag{2.55}$$

where $\tilde{\epsilon}_o$ and $\tilde{N}_o$ are the dielectric function and refractive index corresponding to the o-wave and $\tilde{\epsilon}_e$ and $\tilde{N}_e$ are the corresponding functions for the e-wave.

The theory of the reflectivity from and transmission through a uniaxial layer has already been developed by [11, 12]. Consider light of frequency ω which is incident from a medium 1 with refractive index $\tilde{N}_1$ on a thin uniaxial layer of thickness Δz and indices $\tilde{N}_o = \sqrt{\tilde{\epsilon}_o}$ and $\tilde{N}_e = \sqrt{\tilde{\epsilon}_e}$ at an angle of incidence θ_1 (see Fig. 2–2). It finally passes into a third medium of complex index $\tilde{N}_2$ at an angle θ_2. The xy-plane is the reflecting surface and (α, β, γ) are the direction cosines of the optic axis which satisfy the relations: $\alpha^2 + \beta^2 + \gamma^2 = 1$ and $-1 \leq \alpha, \beta, \gamma \leq 1$. The incident, reflected and transmitted electric fields have a z dependence given by

$$\begin{aligned} &s - polarization \\ &\quad incident \;:\; (0, 1, 0)e^{iq_1 z} \\ &\quad reflected \;:\; (r_{sp}\cos\theta_1, r_{ss}, r_{sp}\sin\theta_1)e^{-iq_1 z} \\ &\quad transmitted \;:\; (t_{sp}\cos\theta_2, t_{ss}, -t_{sp}\sin\theta_2)e^{iq_2(z-\Delta z)}, \end{aligned} \tag{2.56}$$

$$\begin{aligned} &p - polarization \\ &\quad incident \;:\; (\cos\theta_1, 0, -\sin\theta_1)e^{iq_1 z}, \\ &\quad reflected \;:\; (r_{pp}\cos\theta_1, r_{ps}, r_{pp}\sin\theta_1)e^{-iq_1 z}, \\ &\quad transmitted \;:\; (t_{pp}\cos\theta_2, t_{ps}, -t_{pp}\sin\theta_2)e^{iq_2(z-\Delta z)}. \end{aligned} \tag{2.57}$$

The wave vectors used in these equations are $q_{1,2} = (\omega/c)\tilde{N}_{1,2}\cos\theta_{1,2}$.

The form of fields in the layer can be found in [11]. Let us consider the special case of normal incidence where $\theta_1 = 0 = \theta_2$ and where the surrounding media are

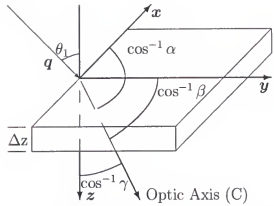

Figure 2–2: A slab of anisotropic crystal with parallel faces. The laboratory axes are labelled, $\boldsymbol{x}$, $\boldsymbol{y}$, $\boldsymbol{z}$, with the upper and lower faces parallel to the xy-plane. Light is incident on the upper plane, $z = 0$ and exits at $z = \Delta z$. Principal axes of the crystal are denoted by a, b, and c; only the c-axis is shown with its orientation in the lab frame given by its direction cosines. The plane of incidence is the xz-plane.

the same $\tilde{N}_1 = \tilde{N}_2$. In this case the reflection and transmission coefficients become

$$r_{ss} = \frac{\alpha^2 r_o + \beta^2 r_e}{\alpha^2 + \beta^2}, \qquad r_{pp} = \frac{\alpha^2 r_e + \beta^2 r_o}{\alpha^2 + \beta^2},$$

$$r_{sp} = r_{ps} = \frac{\alpha\beta}{\alpha^2 + \beta^2}(r_e - r_o), \tag{2.58}$$

$$t_{ss} = \frac{\alpha^2 t_o + \beta^2 t_e}{\alpha^2 + \beta^2}, \qquad t_{pp} = \frac{\alpha^2 t_e + \beta^2 t_o}{\alpha^2 + \beta^2},$$

$$t_{sp} = t_{ps} = \frac{\alpha\beta}{\alpha^2 + \beta^2}(t_e - t_o). \tag{2.59}$$

The reflection and transmission coefficients r_o, r_e, t_o and t_e are those for a slab of thickness Δz and are given by

$$r_o = \frac{s_o(1 - e^{2iK_o\Delta z})}{1 - (s_o)^2 e^{2iK_o\Delta z}},$$

$$r_e = \frac{s_e(1 - e^{2iK_e\Delta z})}{1 - (s_e)^2 e^{2iK_e\Delta z}}, \tag{2.60}$$

$$t_o = \frac{(1 + s_o)(1 - s_o)e^{iK_o\Delta z}}{1 - (s_o)^2 e^{2iK_o\Delta z}},$$

$$t_e = \frac{(1 + s_e)(1 - s_e)e^{iK_e\Delta z}}{1 - (s_e)^2 e^{iK_e\Delta z}}, \tag{2.61}$$

where $K_o = k\tilde{N}_o$, $K_e = k\tilde{N}_o\tilde{N}_e/\tilde{N}_\gamma$ where the single bounce reflectivities are

$$s_0 = \frac{\tilde{N}_1 - \tilde{N}_o}{\tilde{N}_1 + \tilde{N}_o},$$

$$s_e = \frac{\tilde{N}_1 - \tilde{N}_o\tilde{N}_e/\tilde{N}_\gamma}{\tilde{N}_1 + \tilde{N}_o\tilde{N}_e/\tilde{N}_\gamma} \tag{2.62}$$

with

$$\tilde{N}_\gamma^2 = \tilde{\epsilon}_\gamma = \tilde{\epsilon}_o + \gamma^2(\tilde{\epsilon}_e - \tilde{\epsilon}_o). \tag{2.63}$$

These equations allow us to calculate the reflectances $\mathcal{R}_{s,p}$, and transmittances $\mathcal{T}_{s,p}$ of s and p-polarized light where

$$\mathcal{R}_s = |r_{ss}|^2 + |r_{sp}|^2, \qquad \mathcal{T}_s = |t_{ss}|^2 + |t_{sp}|^2,$$

$$\mathcal{R}_p = |r_{pp}|^2 + |r_{ps}|^2, \qquad \mathcal{T}_p = |t_{pp}|^2 + |t_{ps}|^2. \tag{2.64}$$

In the case where we have unpolarized light at normal incidence the reflectance and transmittances become averages,

$$\mathcal{R} = \frac{1}{2}(\mathcal{R}_s + \mathcal{R}_p) = \frac{1}{2}(|r_o|^2 + |r_e|^2),$$

$$\mathcal{T} = \frac{1}{2}(\mathcal{T}_s + \mathcal{T}_p) = \frac{1}{2}(|t_o|^2 + |t_e|^2). \tag{2.65}$$

The generalization to a multilayered sample consisting of a single anisotropic layer and several isotropic layers follows directly. It can be seen from Eqns. (2.64) that the total reflectivity and transmittance is the average of the reflectivity/transmittance of two slabs with reflection and transmission coefficients (r_o, r_e) and (t_o, t_e). In a multilayerd system the matrix theory would be modified, there would be two sets of matrix equations, one for a material of index $\tilde{N}_o$ with a number of isotropic layers and the other set for a material of index $\tilde{N}_o\tilde{N}_e/\tilde{N}_\gamma$ and the same set of isotropic layers. The resulting reflectivity and transmittance would then be the average of the reflectivities and transmittances of both sets of multilayers.

2.5 Drude-Lorentz Model

The extraction of the optical constants of the stratified media composing a multilayer usually involves assuming a particular model of the dielectric response, and fitting the reflectivity or transmittance of the multilayer by varying the parameters of the model. The most common model of the dielectric response used in the infrared region is the Drude-Lorentz model. This model although ad-hoc has proven to be useful in describing the optical characteristics of many materials.

The basic model assumes that the dielectric function can be written as a sum of three terms as

$$\epsilon = \tilde{\epsilon}_D + \tilde{\epsilon}_L + \epsilon_\infty. \tag{2.66}$$

The Lorentz term $\tilde{\epsilon}_L$ represents the response of bound atomic electrons which are bound to their cores by harmonic forces in the presence of viscous damping which represents the dissipative losses of the medium. This term is used to describe the bound-carrier interband transitions, phonons, magnons, and many other infrared active processes. The Lorentz term is given by

$$\tilde{\epsilon}_L = \sum_j \frac{\omega_{pj}^2}{\omega_j^2 - \omega^2 - i\gamma_j\omega}, \tag{2.67}$$

where ω_j, ω_{pj}, and γ_j are the center frequency, plasma frequency and damping constant respectively of the j^{th} Lorentzian. The plasma frequency ω_{pj} is related to the number density n_j, and the effective band mass of bound carriers m_j^*, by $\omega_{pj}^2 = 4\pi n_j e^2/m_j^*$. The plasma frequency is sometimes written as $\omega_{pj} = \sqrt{S_j}\omega_j$ where S_j is an oscillator strength which represents the contribution of the j^{th} oscillator to the static dielectric constant.

The first term in (2.65) is the Drude term. It describes the response of carriers which are essentially free. Typically this is the optical response of a metal. The Drude term describes intraband processes where the free carriers scatter from impurities, phonons, or scattering processes between the carriers themselves. The

Drude term has the form

$$\tilde{\epsilon}_D = -\frac{\omega_{pD}^2}{\omega(\omega + i/\tau)}, \tag{2.68}$$

where ω_{pD} is the Drude plasma frequency defined by $\omega_{pD}^2 = 4\pi n e^2/m^*$ where n is the density of free carriers, m^* is the effective mass of the free carriers and τ is the relaxation time of the carriers associated with scattering. The real part of the Drude conductivity is

$$\sigma_{1D} = \frac{1}{4\pi}\frac{\omega_{pD}^2\tau}{1+\omega^2\tau^2} = \frac{\sigma_0}{1+\omega^2\tau^2}; \tag{2.69}$$

in the d.c limit the conductivity reduces to

$$\sigma_0 = \frac{\omega_{pD}^2\tau}{4\pi} = \frac{ne^2\tau}{m^*}. \tag{2.70}$$

2.6 Sum Rules

One of the most important tools used in the analysis of optical data are the sum rules. The sum rule states that the total area under the real part of the conductivity is conserved. This is simply a statement of charge conservation which becomes

$$\int_0^\infty \sigma_1(\omega)\,\mathrm{d}\omega = \frac{\omega_p^2}{8} = \frac{\pi}{2}\frac{ne^2}{m_e}. \tag{2.71}$$

In many cases it is not feasible to integrate over the entire frequency range and it is often carried out up to some finite upper frequency limit ω_c. This integral gives the effective number of carriers N_{eff} per atom which participate in the optical process up to that frequency and is usually referred to as a partial sum rule. This sum rule is

$$\int_0^{\omega_c} \sigma_1\,\mathrm{d}\omega = \frac{\pi}{2}\frac{n_a e^2}{m^*}N_{eff}(\omega_c); \tag{2.72}$$

where m^* is the effective mass and n_a is the density of formula units.

Sum rules are very important in understanding the superconducting state electrodynamics of the high temperature superconductors (HTSC). The superconducting state is marked by a depression of the low frequency conductivity below the normal state conductivity above T_c. The missing spectral weight appears as a delta function at the origin which represents the response of the condensate. This effect is expressed by the Ferrel-Glower-Tinkham (FGT) sum rule

$$\rho_s = \int_0^\infty [\sigma_1(\omega, T > T_c) - \sigma_1(\omega, T < T_c)]\, \mathrm{d}\omega, \tag{2.73}$$

where ρ_s represents the superfluid density. The sum rules have also been applied to the study of the redistribution of spectral weight with doping in the cuprates. This will be discussed in greater detail in chapter 4.

CHAPTER 3
INTERFEROMETRIC SPECTROSCOPY

3.1 Introduction

One of the most versatile tools available to any spectroscopist who is interested in the optical characteristics of materials in the solid state is the Fourier-transform interferometric spectrometer. The purpose of any spectroscopic instrument is to extract the frequency spectrum of the light field [13–16]. This process can be accomplished in different ways depending on the technique used. In a grating instrument the spectrum is measured by scattering light from a periodic grating. Each frequency component is scattered in a different direction and the separation is done by using a slit to isolate the desired component. The spectrum can then be determined by passing each frequency component in turn onto a suitable detector. This technique is quite time consuming and inefficient because of the necessity of sequential sampling. A far more efficient technique involves the use of a two-beam Michelson-type interferometer. The spectral components in the interferometer are mapped onto a set of sine functions of the retardation, and can easily be extracted by computing the Fourier transform of the detector signal. The purpose of this chapter is to present the basic theory of Fourier spectroscopy, and also to give a brief description of the interferometric spectrometer used in this work— the Bruker 113v.

3.2 Basic Theory

The concepts which are relevant to the understanding of the modern interferometric spectrometer will be presented in this section. I shall discuss the ideal spectrometer as well as some of the problems which are encountered in practice.

3.2.1 Interferogram and Spectrum

Figure 3–1 shows a simple Michelson interferometer. Light emitted by a source is incident on a beamsplitter where it is partly transmitted into one arm and partly reflected into the other. The beams travel to the end mirrors and are reflected, and return to the beamsplitter where they recombine. The combined beams travel to a detector. The light from a broadband source can be represented by a TEM wave having Fourier components $\boldsymbol{E}(\nu)\mathrm{e}^{i\boldsymbol{k}\cdot\boldsymbol{r}}$, here $|\boldsymbol{k}| = 2\pi\nu$, where ν is the frequency of light in units of cm^{-1} which is related to the wavelength λ in cm by $\nu = 1/\lambda$. If

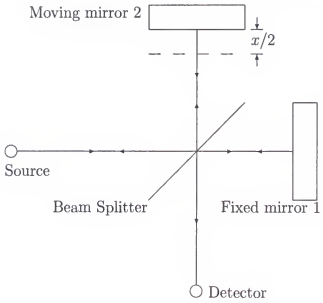

Figure 3–1: A simple Michelson interferometer. The vertical arm labelled 2 is $x/2$ longer than the horizontal one labelled 1; light in the vertical arm has an extra path difference of x.

ν is in cm^{-1} then $|\boldsymbol{r}|$ is in cm. As the wave passes through the interferometer its phase advances and is modified by the beamsplitter which has amplitude reflection and transmission coefficients $r_b\mathrm{e}^{i\phi_r}$ and $t_b\mathrm{e}^{i\phi_t}$; and the end mirrors with reflection coefficients $r_1\mathrm{e}^{i\phi_1}$ and $r_2\mathrm{e}^{i\phi_2}$. The resultant field at the detector is a superposition of the fields from both arms

$$\boldsymbol{E} = \boldsymbol{E}_1 + \boldsymbol{E}_2 \tag{3.1}$$

where

$$\boldsymbol{E}_1 = \boldsymbol{E}_s(\nu) t_b \mathrm{e}^{\mathrm{i}\phi_t} r_1 \mathrm{e}^{\mathrm{i}\phi_1} r_b \mathrm{e}^{\mathrm{i}\phi_r} \mathrm{e}^{2\pi\mathrm{i}\nu R} \tag{3.2}$$

and

$$\boldsymbol{E}_2 = \boldsymbol{E}_s(\nu) r_b \mathrm{e}^{\mathrm{i}\phi_r} r_2 \mathrm{e}^{\mathrm{i}\phi_2} t_b \mathrm{e}^{\mathrm{i}\phi_t} \mathrm{e}^{2\pi\mathrm{i}\nu R} \mathrm{e}^{2\pi\mathrm{i}\nu x} \tag{3.3}$$

where R is the common optical path length of both rays and x is the additional path difference of ray 2. An ideal interferometer has identical arms with ($r_1 \mathrm{e}^{\mathrm{i}\phi_1} = r_2 \mathrm{e}^{\mathrm{i}\phi_2} = -1$) and an ideal beamsplitter for which $r_b = t_b = 1/\sqrt{2}$. The signal at the detector is

$$S(x) = 2\pi \int_0^\infty |\boldsymbol{E}|^2 \, \mathrm{d}\nu = \pi \int_0^\infty p(\nu)[1 + \cos(2\pi\nu x)] \, \mathrm{d}\nu \tag{3.4}$$

where $p(\nu) = |\boldsymbol{E}_s(\nu)|^2$ is the spectral power density of the field. The first term in the integral gives the total power in the field. It can be seen that in the ideal case the detector signal at zero path difference $S(0)$ is twice that at infinite path difference $S(\infty)$ since the second term in the integral vanishes due to rapid oscillations of the cosine function. Since we are not interested in the first term, subtracting out the first term and rewriting the integral in complex notation, and extending to negative frequencies we have

$$I(x) = S(x) - S(\infty) = \frac{\pi}{2} \int_{-\infty}^\infty p(\nu) \mathrm{e}^{2\pi\mathrm{i}\nu x} \, \mathrm{d}\nu. \tag{3.5}$$

$I(x)$ is called the interferogram which is the Fourier transform of the spectrum $p(\nu)$. The spectral power density may easily be recovered by taking the inverse transform,

$$\frac{\pi}{2} p(\nu) = \int_{-\infty}^\infty I(x) \mathrm{e}^{-2\pi\mathrm{i}\nu x} \, \mathrm{d}x, \tag{3.6}$$

so that $I(x)$ and $p(\nu)$ form a Fourier transform pair

$$I(x) \rightleftharpoons \frac{\pi}{2} p(\nu). \tag{3.7}$$

3.2.2 Truncation and Apodization

In reality it is impossible to measure an interferogram out to infinite path differences. The interferogram must be truncated at some point in space. This is achieved by multiplying the interferogram by a function $A(x)$ which serves to cut off the interferogram at some point.

The function $A(x)$ is usually chosen to be a nonzero symmetric function on the interval $-\frac{1}{2}L \leq x \leq \frac{1}{2}L$ or a one-sided function on $0 \leq x \leq L$. The truncated interferogram becomes

$$I'(x) = I(x) \cdot A(x) \rightleftharpoons \tilde{p}(\nu) \star \tilde{a}(\nu); \tag{3.8}$$

so that the calculated spectrum is the true spectrum convolved with the transform of the truncation function. The convolution integral on the right is defined as

$$\tilde{p}(\nu) \star \tilde{a}(\nu) = \int_{-\infty}^{\infty} \tilde{p}(\nu')\tilde{a}(\nu - \nu')\,\mathrm{d}\nu'. \tag{3.9}$$

In general both $\tilde{p}(\nu)$ and $\tilde{a}(\nu)$ may be complex since $I(x)$ and or $A(x)$ may not be symmetric functions and so possess complex transforms. If the width of $A(x)$ is L then the with of its transform $\tilde{a}(\nu)$ is of the order $1/L$, and thus the resolution of the interferometer is limited by the maximum path difference of the interferogram. Consider a simple case where the truncation function is a window function

$$W(x, L) = \begin{cases} 0, & |x| > \frac{1}{2}L \\ 1, & |x| \leq \frac{1}{2}L \end{cases} \tag{3.10}$$

$$W(x, L) \rightleftharpoons w(\nu, 1/L) = L \sin(\pi\nu L)/(\pi\nu L).$$

The window function is not a convenient truncation function because its transform is the sinc function which has very large side lobes on either side of the principal maximum. These large side lobes may cause intensity errors in the vicinity of very sharp spectral features. In order to combat this undesirable situation, the window

function is usually multiplied by an apodization function, whose transform when convolved with the sinc function serves to suppress the side lobes at the expense of resolution.

There are many apodization functions which are used in practice. The choice of apodization function intimately depends on the desired resolution and accuracy. Table 3–1 lists a few such apodization functions and their corresponding transforms.

Table 3–1: Apodization functions and their corresponding transforms.

	$A(x)$	$a(\nu)$	Half width
Unapodized	1	$L\,\mathrm{sinc}(y)$	$1.22/L$
Triangular	$1-(2\lvert x\rvert/L)$	$\frac{1}{2}L\,\mathrm{sinc}^2(y/2)$	$1.80/L$
Cosine	$\cos(\pi x/L)$	$\frac{1}{2}L[\mathrm{sinc}(y+\frac{1}{2})+\mathrm{sinc}(y-\frac{1}{2})]$	$1.58/L$
Happ-Genzel	$a+b\cos(2\pi x/L)$	$L\,(\mathrm{sinc}(y)\{a-[by^2/(y^2-\pi^2)]\}$	$1.82/L$
Quartic	$[1-(2x/L)^2]^2$	$4(2\pi)^{\frac{1}{2}}LJ_{\frac{5}{2}}(y)/y^{\frac{5}{2}}$	$1.92/L$

All $A(x)=0$ for $\lvert x\rvert > \frac{1}{2}L$; $y=\pi\nu L$

3.2.3 Sampling

In practice the interferogram is recorded by digital computer which performs the actual transform. The interferogram is usually sampled and the spectrum calculated at a large number of discrete equally spaced points. The integral transform is then replaced by a sum. Mathematically, the sampling of the interferogram can be expressed as the product of a Dirac comb and the actual interferogram. The comb and its transform are given by

$$()(x,\Delta x)=\sum_{j=-\infty}^{\infty}\delta(x-j\Delta x)\rightleftharpoons(1/\Delta x)()(\nu,1/\Delta x). \tag{3.11}$$

The interferogram is then sampled at points $j\Delta x$; the sampled interferogram becomes

$$I(x)\cdot()(x,\Delta x)\rightleftharpoons(1/\Delta x)\tilde{p}(\nu)\star()(\nu,1/\Delta x); \tag{3.12}$$

where

$$\tilde{p}(\nu) \star ()(\nu, 1/\Delta x) = \sum_{j=-\infty}^{\infty} I(j\Delta x)\{\exp[-2\pi i j(\Delta x)\nu]\}\Delta x. \tag{3.13}$$

The periodicity of the complex exponential gives rise to a number of interesting consequences. It can easily be seen from equation 3.13 that for a fixed value of j if ν is increased to $\nu + 1/\Delta x$ the exponential remains unchanged. The sum implies that the convolution with the comb generates infinitely many periodic replicas of $\tilde{p}(\nu)$ having a period $1/\Delta x = 2\nu_m$; which is known as aliasing (folding). This implies that if the maximum frequency in the spectrum ν_m is less than half the period of the comb the periodic spectra or aliases won't overlap and there will be no error associated with the sampling; this statement is usually referred to as Nyquist's theorem.

It is often the case that one is interested in a spectral range which is narrower than the range from 0 to ν_m; for instance if we are interested in a spectral bandwidth $\nu_l \leq \nu \leq \nu_m$ where $\nu_l \neq 0$. It is then possible to increase the sampling interval Δx of the interferogram beyond $1/(2\nu_m)$ to $1/2(\nu_m - \nu_l)$. This speeds up the time required to scan the interferogram. The range of the spectrum can easily be reduced by optical or mathematical filtering [17]. An interferogram which is oversampled simply wastes computer time; while undersampling leads to errors in the calculated spectra due to spectral folding.

3.2.4 Phase Errors

In an ideal interferometer the measured interferofram is symmetric about the zero path difference (ZPD) or "white-light" position. It therefore follows that the transform of a two-sided interferogram extending from $-L/2$ to $L/2$ gives a purely real spectrum. An asymmetric interferogram may arise in a number of different ways. The simplest example of a phase error occurs when the arms of the interferometer are not identical so that $\phi_1 \neq \phi_2$. Differences in the absolute reflectivity do not affect the phase. Other possible causes of phase error include

the electrical phase shift associated with the detector and also sampling error. The transform of an asymmetric interferogram is a complex function of frequency. The main purpose of any phase correction procedure is to recover the original spectrum.

It can easily be shown that in the presence of a phase error $\phi(\nu)$ the interferogram becomes

$$I(x) = \frac{\pi}{2} \int_{-\infty}^{\infty} p(\nu) \mathrm{e}^{(2\pi i \nu x + i\phi(\nu))} \, \mathrm{d}\nu \tag{3.14}$$

so that

$$p(\nu)\mathrm{e}^{\mathrm{i}\phi(\nu)} = \int_{-\infty}^{\infty} I(x)\mathrm{e}^{-2\pi i \nu x} \, \mathrm{d}x. \tag{3.15}$$

The error may be easily corrected by multiplying the transform of the interferogram by $\mathrm{e}^{-\mathrm{i}\phi(\nu)}$ which gives the correct spectrum $p(\nu)$. This multiplicative procedure was first proposed by Mertz [18]. Another technique involves taking the magnitude of the calculated spectrum

$$|p(\nu)\mathrm{e}^{\mathrm{i}\phi(\nu)}| = \sqrt{p_1^2(\nu) + p_2^2(\nu)}$$

where $p_1(\nu) = p(\nu)\cos\phi(\nu)$ and $p_2(\nu) = p(\nu)\sin\phi(\nu)$ are the real and imaginary parts of the spectrum calculated from a two-sided interferogram extending from $-L$ to L. Other techniques of phase correction have been proposed by other authors [19, 20]. In practical terms the phase correction is usually carried out by measuring a short two-sided interferogram which extends from $-L_1/2$ to $L_1/2$. The complex transform of this low resolution interferogram allows the phase $\phi(\nu)$ to be determined.

3.2.5 Noise

One of the great advantages of Fourier transform spectroscopy over conventional grating spectroscopy is the advantage in the signal-to-noise ratio which achieved due to multiplexing. This fact was first pointed out by Fellgett [21]. The reduction of noise in the calculated spectrum is always a welcomed feature in any

spectroscopic technique. An advantage of this kind is not always realized, as it depends strongly on the type of noise which is present in the spectrum.

Noise in transform spectroscopy may arise in a variety of ways. The radiation field invariably contributes noise and so does the detector and its associated electronics. Noise may be characterized as additive or multiplicative. The noise which is produced by a detector and its electronic components tend to add to the interferometric signal; provided that the electronics have strictly linear characteristics; this is called additive noise. The radiation field produces multiplicative noise. There are two main categories of multiplicative noise namely; photon noise and signal noise [22, 23]. Photon noise is associated with the quantum nature of the light field. The number of photons N arriving at a given point will fluctuate randomly by $\pm\sqrt{N}$ and therefore gives rise to photon noise. Signal noise is produced by fluctuations in the source output or else by scintillation of the intervening medium between the source and the detector. Either type of noise may have a frequency independent power spectrum—white noise—or a frequency dependent power spectrum. A common example of frequency dependent noise is amplifier noise (also called $1/f$ noise) which diverges as $1/f$, where f is the frequency.

The relationship between random noise on the interferogram and noise on the corresponding spectrum as well as the Fellgett advantage can easily be derived. The sampled interferogram may be viewed as a sum of a noiseless interferogram and a noisy interferogram $B(x)$

$$B(j\Delta x) = E_j[I_0 + I(j\Delta x)]^n. \tag{3.16}$$

Here it is assumed that the noise scales as the nth power of the detector signal, where I_0 is the dc component which was neglected earlier. E_j is a statistically

random parameter whose ensemble averages satisfy the following relations

$$\begin{aligned} \langle E_j E_{j'}^* \rangle &= E^2 \delta_{jj'} \\ \langle E_j \rangle &= 0 \end{aligned} \tag{3.17}$$

The dc component I_0 is related to the average value of the spectrum by $I_0 = \bar{p}(\nu_k) N \Delta\nu$, where N is the number or sampling points and $\Delta\nu = 1/L$ where L is the length of the interferogram. The ensemble average of the noise on the spectrum becomes

$$b^2 = \langle |b_k|^2 \rangle = E^2 (\Delta x)^2 \sum_j [I_o + I(j\Delta x)]^{2n}. \tag{3.18}$$

When $N \gg 1$,

$$b^2 \approx E^2 (\Delta x)^2 N I_0^{2n} \tag{3.19}$$

so that

$$b = E[\bar{p}(\nu_k)]^n N^{n-1/2} (\Delta\nu). \tag{3.20}$$

The comparison if the signal-to-noise ratio of an inteferometer and that of a grating monochromator of equal resolution $\Delta\nu$ can easily be obtained. The signal-to-noise ratio of the interferometer is

$$(\mathrm{SNR})_i = \frac{p(\nu_k)}{b} = \frac{p(\nu_k)\Delta\nu}{E[\bar{p}(\nu_k)\Delta\nu]^n} N^{-n+\frac{1}{2}} \tag{3.21}$$

and that for a grating monochromator is given by

$$(\mathrm{SNR})_m = \frac{p(\nu_k)\Delta\nu}{E[p(\nu_k)\Delta\nu]^n}. \tag{3.22}$$

The ratio of these two expressions gives

$$\frac{(\mathrm{SNR})_i}{(\mathrm{SNR})_m} \approx N^{-n+1/2} = \begin{cases} N^{1/2} & n = 0 \quad \text{detector noise} \\ 1 & n = \frac{1}{2} \quad \text{photon noise} \\ N^{-1/2} & n = 1 \quad \text{source noise.} \end{cases} \tag{3.23}$$

This last equation clearly indicates that the Fellgett advantage is obtained only for the $n = 0$ case where the noise is the thermal detector noise (Johnson noise). One interesting consequence of this observation is that at higher frequencies in the near infrared to ultraviolet regions of the spectrum where phonon noise is the dominant source of noise the signal-to-noise ratio of an interferometer offers no advantage over the corresponding grating monochromator. The Felleget advantage is only obtained in the infrared region where the dominant noise source is thermal detector noise. Another way of seeing the Fellgett advantage is in terms of the measurement time. The noise parameter E is directly proportional to $t^{-1/2}$, where t is the time taken to measure a single data point on the interferometer or a single point in the spectrum on a grating monochromator. Then it is easy to see that by substituting $E = Kt^{-1/2}$ into equations (3.23) with $n = 0$ and (3.22) respectively that the signal-to-noise ratio in terms of the measurement time becomes

$$(\mathrm{SNR})_i = \frac{p(\nu_k)\Delta\nu}{K[\bar{p}(\nu_k)\Delta\nu]^n} T^{1/2} \tag{3.24}$$

and

$$(\mathrm{SNR})_m = \frac{p(\nu_k)\Delta\nu}{E[p(\nu_k)\Delta\nu]^n} t_m^{1/2} \tag{3.25}$$

where $T = Nt$ is the total measurement time for the inteferometer. This shows that the signal-to-noise ratio of the monochromator is only equal to that of the interferometer if the time taken to measure a single spectral point with the monochromator is equal to the total measurement time of the interferometer.

3.3 Bruker 113v Spectrometer

The far infrared measurements which will be presented later, were performed using the Bruker 113v fast-scan Fourier transform interferometric spectrometer. It covers a frequency range from about 20–5000 cm^{-1}; where the far infrared range lies between 20–600 cm^{-1}. Figure 3–2 is a schematic diagram of the Bruker 113v. The spectrometer consists of four main chambers: the source chamber, the

interferometer chamber, the sample chamber and the detector chamber. During the measurement the entire spectrometer is evacuated to prevent absorption by carbon dioxide and water vapor.

The source chamber houses two different lamps; a mercury arc lamp which is used in the far infrared range and a globar source for the mid infrared range. Light from these sources is channelled by a series of mirrors through an automated aperture to the main interferometer.

The interferometer chamber consists of a two-sided scanning mirror, optical filter, control interferometer and beamsplitters. There are 5 beamsplitters which together cover the entire spectral range. Three of them are different thicknesses of mylar which are used over different spectral ranges in the far infrared and the fourth is a composite germanium-potassium bromide (Ge/KBr) beamsplitter which is used in the mid infrared. The final beamsplitter, also used in the far infrared, is made of metal-mesh, but is rarely used because of the losses associated with it. The control interferometer serves the important purpose of ensuring that the interferogram is properly sampled. It is two interferometers rolled into one. As the scanning mirror moves the control interferometer generates two interference patterns. It has a white light source and a helium-neon (He-Ne) laser source each of which produces its own interference pattern. The laser wavelength is accurately known and so the zero-crossings of its interference pattern is used to mark when the interferogram is sampled. The white light interference pattern is sharply peaked at at zero path difference and this position marks where the sampling begins on each scan of the moving mirror. This is the technique which is used to digitize the interferogram. The two-sided mirror introduces twice the path difference of the simple Michelson interferometer discussed earlier for a given mirror displacement. After passing through the main interferometer the light passes into the sample chamber.

Transmittance measurements are usually made on samples mounted in the front of the sample chamber at the transmittance focus i in the figure, while reflectivity measurements are usually done in the back of the chamber where the sample focus lies at the point j. The sample stages which are used for each type of measurement are not shown in the figure. Finally, the light enters the detector chamber.

Signal detection is performed by a liquid helium-cooled silicon bolometer which is shown in fig. 3–3. This detector which is used in the far-infrared spectral range, consists of three main parts: 1) the actual detector, 2) a liquid helium can which is in contact with the detector and which serves to cool it, and 3) a preamplifier which amplifies the signal. The detector is maintained at cold operating temperature by evacuating the detector chamber and filling the helium can with liquid helium. Certain design characteristics ensure that the detector remains cold for long periods; among these are the outer nitrogen can which is filled with nitrogen and a thermal radiation shield which surrounds the detector chamber. At optimum performance the detector remains cold for nineteen to twenty hours. Light which is focused on the detector is amplified by the preamplifier and sent on to an anolog to digital converter of interferometer for digitization. The most notable feature of a bolometer of this type is the very high signal-to-noise ratio which is obtained in the far-infrared region compared to other detectors which operate over a similar frequency range.

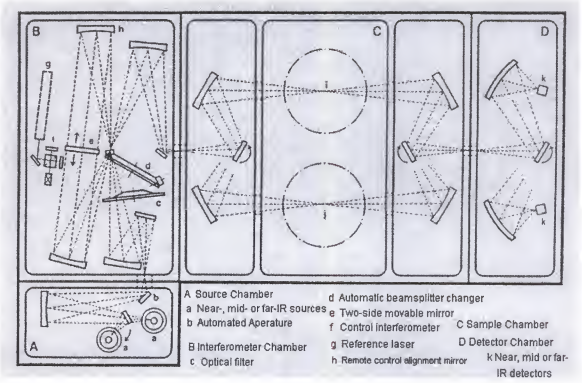

Figure 3–2: Schematic diagram of Bruker 113-v Fourier transform spectrometer.

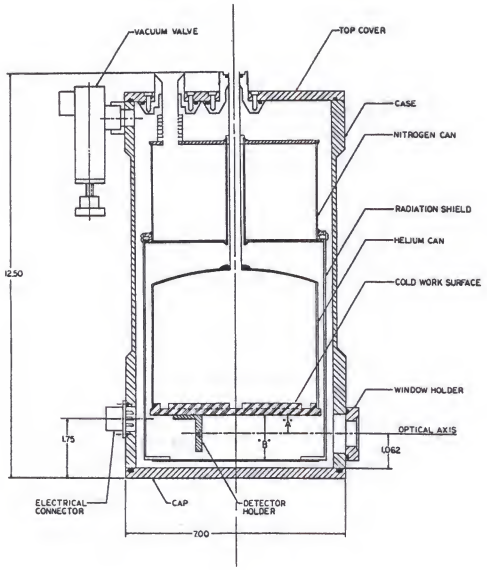

Figure 3–3: Helium cooled bolometer detector. All dimensions are in inches.

CHAPTER 4
INFRARED PROPERTIES OF HIGH-T_c SUPERCONDUCTORS

4.1 Introduction

The issue of superconductivity in the cuprates is by no means a simple one. The interpretation of the results of various experiments on the cuprates have often been the subject of intense debate; and have spawned several theories relating to the underlying mechanism of superconductivity in these materials. In spite of an unprecedented effort, the mechanism of high-T_c superconductivity in the cuprates still remains a mystery.

Infrared spectroscopy still remains a premier experimental tool in the investigations of the electrodynamics of the high-T_c superconductors. Immense progress in the growth of high quality single crystals and thin film specimens has led to a closer convergence amongst the spectroscopic results of different groups. The physics of highly correlated electronic systems—of which the cuprates are a member—are reflected in the optical constants at fairly low frequencies which can be probed by infrared (IR), optical, terahertz (THz) and microwave spectroscopies. A combination of model independent analysis of infrared data based on the sum rules, combined with comprehensive studies of many different families of the cuprates by IR-THz/optical spectroscopies have served to highlight universal trends in the optical response. The main purpose of this chapter is to briefly review the generic optical features of the cuprates and to present some of the techniques commonly used to analyze optical data.

4.2 Generic Trends

4.2.1 Normal State Phase Diagram

Superconductivity in the cuprates appears when the parent antiferromagnetic insulating phase is doped. This introduces a moderate density of charge carriers. Doping is achieved either by chemical substitution (eg. $La_2CuO_4 \rightarrow La_{2-x}M_xCuO_4$ where $M = Ba, Sr, Ca$); or by doping with oxygen ($La_2CuO_4 \rightarrow La_2CuO_{4+\delta}$).

The generic trends of the evolution of the optical response of the cuprates in the normal state with temperature and doping can be inferred from the normal state phase diagram [24]. There are a number of common elements which are worth mentioning. It is found that: 1) the undoped insulating compounds all show antiferromagnetism with a Néel temperature which decreases with doping; and becomes conducting upon further doping; 2) superconductivity occurs for doping levels beyond a critical level; 3) a transition temperature which first increases with doping (underdoped region), reaches a maximum at optimal doping and finally decreases with further doping (overdoped region); 4) in the underdoped regime the superconducting state is preceded by a pseudogap whose onset temperature decreases with increasing doping; 5) a fairly narrow temperature region above the transition temperature T_c which is associated with the formation of a bosonic resonance and the onset of high in-plane coherence.

These features are all generic features of the hole-doped cuprates except La-214 where the pseudogap is quite weak [25] and the Cu spin relaxation shows no sign of a spin gap at lower temperature [26, 27]. The pseudogap and bosonic mode are still in dispute in the electron-doped cuprates such as $Nd_{2-x}Ce_xCuO_4$.

4.2.2 Crystal Structure

The cuprates possess a layered structure which is often classified as a perovskite crystal structure. This is a label given to a generic class of crystals whose structure resembles that of $SrTiO_3$ (such as $YBa_2Cu_3O_7$) and a derived one K_2NiF_4

(La_2CuO_4 structure) [28]. The salient structural feature of the cuprates is the presence of n copper oxide planes CuO_2 separated by by the so-called charge reservoirs. Superconductivity is thought to be associated with the CuO_2 planes while the charge reservoirs play a secondary role. The $La_{2-x}Sr_xCuO_4$ (La-214) and $Nd_{2-x}Sr_xCuO_4$ (Nd-214) materials all have a single CuO_2 plane and are usually called the single-layered compounds; they are usually characterized by the lowest transition temperatures at optimal doping. The most frequently studied cuprates $YBa_2Cu_3O_{6+x}$ (Y-123) and $Bi_2Sr_2CaCu_2O_{8+x}$ (Bi-2212) have $n = 2$ CuO_2 planes per unit cell and higher T_cs than the single-layered compounds. Many different families of the cuprates may be synthesized with $n = 1, 2, 3, 4$ and the transition temperature increases with the number of planes n up to $n = 3$. The transition temperature saturates or even decreases for higher n.

The undoped cuprates are usually described as Mott-Hubbard insulators. The large coulomb repulsion between Cu ions splits the Cu 3d band into an upper and lower Hubbard band with a gap U. The energy U is the cost of creating a doubly occupied Cu site in the upper Hubbard band. Another important energy scale is the hopping matrix element t. If the spins on adjcent sites are oppositely oriented they can hop from one site to the next effectively lowering the energy of the system by an amount proportional to $-t^2/U$. This is equivalent to an exchange interaction $J = 4t^2/U$ which leads to antiferromagnetism. The oxygen 2p band lies inside the Hubbard gap so that the charge transfer gap E_g is less than U. The cuprates are thus referred to as charge transfer insulators [29]. The optical conductivity in the CuO_2 (ab plane) thus shows an absorption edge which lies between 1–2 eV owing to excitations between the O 2p to the Cu $3d_{x^2-y^2}$ states.

4.2.3 Doping Effects

The evolution of the low frequency electronic state of the cuprates with doping has been studied by several groups in the infrared [30, 31]. The main feature of

the process is that doping leads to the development of free-carrier absorption and a very broad absorption band in the mid-infrared region below the charge transfer gap. These two bands develop at the expense of the charge transfer excitations which weaken with doping. The free carrier band develops more rapidly than the mid infrared band which softens with doping. In many cases the bands merge and can hardly be distinguished at high doping levels.

At moderate doping levels, the free-carrier spectral weight which is proportional to n/m^* increases linearly with doping, [30, 32] where n is the carrier density and m^* is their effective mass. Close to optimal doping further doping does not increase the electronic spectral weight and the ratio n/m^* saturates. This is not a generic feature as a different effect has been reported for Bi-2212. It has been found that the spectral weight of Bi-2212 continues to increase in the overdoped regime [33].

4.2.4 Optical Anisotropy

The strongly layered crystal structure of the cuprates give rise to anisotropy in the observed electronic properties in the infrared. The in-plane response as measured by optical reflectivity in the normal state along the CuO_2 planes displays conducting behavior while the c-axis response perpendicular to the planes almost universally displays insulating behavior. This behavior is observed in all families as a fairly large ab-plane reflectivity at low frequencies ($\omega < 100$ cm^{-1}) and the appearance of a plasma edge in the reflectivity in the near infrared to visible frequency range ($\omega \approx 1 - 2$ eV); while the c-axis reflectivities are lower and show no such plasma edge above the spin gap temperature. The ab-plane phonon modes observed in the parent compound are also strongly suppressed with increased doping due to screening by the free carriers. By contrast the c-axis reflectivity spectra are dominated by a large number of infrared active phonons at all doping levels, which are also observed in the parent compound.

There are many physical quantities of interest which display anisotropy in the cuprates,including dc resistivity [34–36], optical conductivity, and penetration depths in the superconducting state. The degree of anisotropy depends strongly on the particular family being studied. The existence of copper oxide chains in YBCO implies that the ab-plane electronic and optical properties are also anisotropic [37, 38]; ab-plane anisotropy has also been observed in Bi-2212 [39–41]. These features have been studied by polarization measurements along the a and b-axes by several groups above. The observed anisotropy is not confined to the normal state; the superfluid density is also anisotropic and varies from family to family. In most cuprates the condensate plasma frequency extracted from the ab-plane optical conductivity lies between 4000 and 10000 cm^{-1}; while the corresponding c-axis plasma frequencies range between 1 and 1000 cm^{-1}. This gives rise to strong anisotropy in the calculated penetration depths extracted from optical measurements (note: the penetration depths are just the reciprocal of the condensate plasma frequency in cm^{-1} so the c-axis penetration depths are always larger than the in-plane values). For Y-123 there is superfluid density associated with the chains so that the b-axis penetration depths λ_b are smaller than the corresponding a-axis values λ_a. Light polarized along the a-axis probes only the CuO_2 planes while light polarized along the b-axis probe both the chains and planes.

4.3 Models of Optical Conductivity

Over the last decade and a half a number of models have been used to analyze the in-plane reflectivity and transmittance data of the cuprates. Each model has its advantages and its disadvantages. The dynamical conductivity obtained from Kramers Kronig analysis when fitted to any of these models allows for the extraction of various optical parameters which give important information

about the low energy excitations and the electronic state of the cuprates. A brief description of the commonly used models will be given in this section.

4.3.1 Two-Component Model

One of the earliest models used to fit the normal state optical conductivity of the cuprates is the two-component model [2, 40, 42]. The model arose out of the observation that doping led to the transfer of spectral weight into the charge transfer gap of the parent compounds. At light to moderate doping levels sharp features are observed in the mid-infrared region together with a Drude-like band at low frequencies ($\omega < 500$ cm^{-1}). Two resonances were observed in the mid infrared; a very broad resonance at 0.5 eV which softened with doping together with a second resonance at 0.25 eV. The feature at 0.25 eV was close to the anti-ferromagnetic exchange energy J [43]. The mid infrared absorption has also been attributed to polaron modes [44–46]. The two component model assumes a dielectric function of the form

$$\tilde{\epsilon}(\omega) = -\frac{\omega_{pD}^2}{\omega^2 + i\omega/\tau} + \sum_j \frac{\omega_{pj}^2}{(\omega_j^2 - \omega^2 - i\omega\gamma_j)} + \epsilon_\infty = \tilde{\epsilon}_D(\omega) + \tilde{\epsilon}_{mid-ir}(\omega) + \epsilon_\infty \quad (T > T_c). \tag{4.1}$$

The first term in eq. (4.1) represents the Drude free-carrier response with plasma frequency ω_{pD} and relaxation rate $1/\tau$. The sum represents additional contributions to the dielectric response in the mid infrared which are modeled with Lorentzian oscillators with center frequency ω_j, plasma frequency ω_{pj} and line width γ_j. Finally ϵ_∞ includes the high frequency contribution from processes above the measured range. A two-component model is always questionable at higher doping levels of the cuprates, where the Drude and midinfrared bands are sometimes not clearly resolved.

In the superconducting state, a two-fluid model is used where a fraction f_s of the free carriers condense to form superfluid, and the remaining fraction $(1 - f_s)$

represents the response of thermally excited quasiparticles which still exhibit a Drude response. The two fluid conductivity is written as

$$\tilde{\sigma}(\omega) = (1 - f_s)\frac{\omega_{pD}^2 \tau}{4\pi(1 - i\omega\tau)} + f_s \frac{\omega_{pD}^2}{4\pi}\left[\pi\delta(\omega) + \frac{i}{\omega + i0^+}\right] + \tilde{\sigma}_{mid-ir}(\omega). \tag{4.2}$$

The mid-infrared conductivity σ_{mid-ir} usually shows little or no temperature dependence. The superfluid response in the dc limit which gives zero resistivity in the superconducting state is represented by the delta function $\delta(\omega)$ in the conductivity.

4.3.2 One-Component Models

The extended Drude model. In many cases the infrared conductivity of the cuprates below the charge transfer region is fitted with an extended Drude model [47-49]. The model assumes that the low frequency conductivity is due to a single type of charge carrier with a frequency dependent scattering rate. The conductivity can be extended beyond the simple Drude form by making the damping term complex and frequency dependent such that $1/\tau = M(\omega) = M'(\omega) + iM''(\omega)$, where $M(\omega)$ is a complex memory function. This model has been extensively used to study the carrier dynamics of the cuprates. The memory function maybe rewritten as $M(\omega, T) = 1/\tau(\omega, T) - i\omega\lambda(\omega, T)$ so that the conductivity becomes

$$\tilde{\sigma}(\omega, T) = \frac{1}{4\pi}\frac{\omega_p^2}{M(\omega, T) - i\omega} = \frac{1}{4\pi}\frac{\omega_p^2}{1/\tau(\omega, T) - i\omega[1 + \lambda(\omega, T)]}. \tag{4.3}$$

The quantities $1/\tau(\omega, T)$ and $\lambda(\omega, T)$ are the frequency dependent scattering rate and effective mass enhancement due to interactions of the carries with a cloud of excitations. They are related to $\tilde{\sigma}(\omega)$ through the relations

$$1/\tau(\omega) = \frac{\omega_p^2}{4\pi}\Re\left(\frac{1}{\tilde{\sigma}(\omega)}\right), \tag{4.4}$$

i.e., the scattering rate is proportional to real part of the reciprocal conductivity; while the mass enhancement factor $\lambda(\omega)$ varies as the imaginary part of the same

response function

$$1 + \lambda(\omega) = -\frac{\omega_p^2}{4\pi}\frac{1}{\omega}\Im\left(\frac{1}{\tilde{\sigma}(\omega)}\right). \tag{4.5}$$

Marginal Fermi liquid. Another very commonly used model is the marginal Fermi liquid model due to Varma et al [50, 51]. The model assumes that the charge carriers interact with a fairly flat spectrum of excitations over the interval $T < \omega < \omega_c$ where ω_c is a high frequency cutoff. The dielectric response for this model can be written as

$$\tilde{\epsilon}(\omega) \approx -\frac{\omega_p^2}{\omega[\omega - 2\Sigma(\omega/2)]} \tag{4.6}$$

where Σ is the quasiparticle self-energy, given by

$$\Sigma = 2\lambda\omega \log\left(\frac{\pi T - i\omega}{\omega_c}\right) - i\pi^2\lambda T; \tag{4.7}$$

here T is the temperature λ is a coupling constant and ω_c is the cutoff frequency. The limiting forms of this expression go as

$$-\Im\Sigma(\omega) \sim \begin{cases} \pi^2\lambda T, & \omega < T \\ \pi\lambda\omega, & \omega > T. \end{cases} \tag{4.8}$$

Since the imaginary part of the self-energy is effectively the scattering rate, eq. (4.8) predicts linear variation of the dc resistivity, which is observed in most transport studies of the cuprates. In a similar fashion the real part of the self-energy gives the mass enhancement of the carriers;

$$\frac{m^*(\omega)}{m_b} = 1 - \frac{2}{\omega}\Re\Sigma\left(\frac{\omega}{2}\right), \tag{4.9}$$

where m^* is the frequency dependent renormalized mass and m_b is the band mass which appears in the plasma frequency $\omega_p = 4\pi ne^2/m_b$.

Nested Fermi liquid. The anomalous optical properties of the normal state of the cuprates have been described in terms of Fermi surface nesting by Virosztek

and Ruvalds [52, 53]. This nested Fermi liquid approach attributes the anomalous normal state properties to carriers which lie on parallel regions of the two dimensional Fermi surface which are spanned by common nesting wavevectors. This nesting causes qualitative changes in the susceptibility and self-energy of the carriers. It is assumed that the dominant scattering process is electron-electron or hole-hole scattering, for which the imaginary part of the complex self-energy (which is the scattering rate) becomes

$$-\Im\Sigma(\omega) = \alpha \max(\beta T, |\omega|); \tag{4.10}$$

here α is a dimensionless coupling constant and β is a constant of the order of unity. The above equation predicts a similar temperature and frequency dependence of the scattering rate as the marginal Fermi liquid model. Therefore the scattering rate is linear in the higher energy scale ω or T. The model also predicts a strong mass renormalization at low frequency,

$$\frac{m^*}{m} = 1 + \frac{2\alpha}{\pi} \ln\left[\frac{\omega_c}{\max(\beta T, \omega)}\right], \tag{4.11}$$

where ω_c is a cutoff frequency.

4.4 Superconducting State Electrodynamics

Superconductivity in the cuprates occurs when the temperature is lowered below the transition temperature T_c. The superconducting state is a macroscopic quantum state, where are certain fraction of the carriers condense to form superfluid. This idea was first proposed by London and London in connection with conventional superconductors [54]. The density of the condensed carriers n_s is related to the magnetic penetration depth λ_L as

$$\lambda_L = \sqrt{m^* c^2 / 4\pi n_s e^2}. \tag{4.12}$$

In a simple London superconductor the real and imaginary parts of the complex conductivity are $\sigma_1(\omega) = (n_s e^2/m^*)\frac{\pi}{2}\delta(0)$, and $\sigma_2(\omega) = (n_s e^2/m^*\omega)$ where the area under the delta function is proportional to the density of superconducting electrons. The simple London theory assumes local electrodynamics where the penetration depth λ_L is much greater than the superconducting coherence length ξ [55]. This condition is satisfied in the cuprates where for YBCO at optimal doping and a T_c of the order of 93 K the ab-plane penetration depth $\lambda_{ab} \approx 1500$ Å while the ab-plane coherence length $\xi_{ab} \approx 15$ Å [28].

These simple expressions for the conductivity assume complete condensation of all the Drude charge carriers below T_c. It predicts a vanishing real conductivity σ_1 at all nonzero frequencies—a clearly untenable state of affairs. The two fluid model eq. (4.2) rectifies this by assuming that below T_c the total Drude oscillator strength is shared between the condensate and the thermally excited quasiparticles. Both the simple London theory and the two fluid model fail to describe the energy gap 2Δ in the density of states which is the centerpiece of the BCS theory of conventional superconductors. The gap in conventional superconductors could be observed by infrared spectroscopy in the dirty limit where the scattering rate far exceeds the gap, $1/\tau \gg 2\Delta$. At low temperatures where the quasiparticle excitations are frozen out and $\sigma_1(\omega) = 0$ for $\omega < 2\Delta$ the gap appears as an absorption edge in $\sigma_1(\omega)$ at the gap frequency $\omega = 2\Delta$.

Many of the early infrared studies of the cuprates in the superconducting state assigned a gap frequency to certain features, such as a shoulder observed in the reflectance, or to the minimum in the extracted conductivity at far infrared frequencies. These assignments have since been discredited by the observation that the cuprates are in the clean limit normal skin effect regime, where $(1/\tau \ll 2\Delta; \xi_0 \ll l \ll \lambda_L)$ ie. the scattering rate is much smaller than the gap and the mean free path l lies between the coherence length and penetration depth. This

means that when condensation occurs the majority of the spectral weight of the conductivity will be transferred to the delta function at the origin [42, 56]. The gap feature if present will be very weak as there is little spectral weight left for excitations above the gap.

4.5 Survey of Experimental Results

4.5.1 Doping Dependence of Optical Constants

One of the first systematic studies of the effect of doping on the in-plane low frequency carrier response was due to Orenstein *et al.* on microtwinned crystals of $YBa_2Cu_3O_{6+x}$ [30]. Later, Uchida *et al.* [31] performed similar ab-plane reflectivity measurements at room temperature on $La_{2-x}Sr_xCuO_4$ single crystals. The results of these latter measurements and the extracted optical conductivity $\sigma(\omega)$ are shown in fig. (4-1). The next few sections highlight some of the characteristics which are common to all doped cuprates.

Optical reflectivity . The reflectivity shows a number of characteristic features which are worth mentioning. Firstly, the undoped phase, $x = 0$, shows a reflectivity typical of an insulator; with a phonon mode near 0.09 eV which precedes a very broad flat reflectivity at higher frequency. The structure which appears in the reflectivity, peaked at 2 eV has been assigned to the Cu-O charge transfer band. Then, with doping the reflectivity grows in the midinfrared, and a reflectivity edge develops at the expense of the charge transfer band which weakens. The 0.09 eV phonon mode is also masked with doping. Finally the plasma minimum at $\approx$ 1 eV is almost insensitive to doping and in fact displays a slight softening in the overdoped regime $x = 0.34$. The plasma minimum corresponds to the zero crossing of the real part of the dielectric function $\epsilon_1(\omega)$. The plasma minimum lies between the midinfrared and charge transfer bands; the midinfrared band makes a negative contribution to $\epsilon_1(\omega)$ while the charge transfer band makes a positive contribution.

The softening of the plasma minimum is an indication of a decrease of the spectral weight associated with these bands in the strongly overdoped regime.

Optical conductivity. The corresponding optical conductivity extracted from the reflectivity is shown in fig (4-1). The insulating character of the undoped compound is clearly seen in the absorption edge which begins at about 1 eV and is peaked at $\approx$ 2 eV and is attributed to charge-transfer processes. At light doping the charge-transfer band is weakened and a peak centered at about 0.5 eV in the midinfrared develops. As the doping increases a smaller feature at $\approx$ 1.5 eV is seen.

The peak in the midinfrared band softens and strengthens with increased doping, as does the Drude, peak and becomes just a shoulder at $x = 0.15$ which corresponds to optimal doping. The peak merges with the the Drude conductivity centered at $\omega = 0$ in the overdoped regime and a clear separation between the two bands can no longer be made.

Oscillator strength sum rule. The observed changes in the conductivity may be further quantified by considering the effective electron number $N_{eff}(\omega)$ per copper atom contributing to the optical processes up to a frequency ω. This is given by the partial sum rule

$$N_{eff}(\omega) = \frac{2m_e V_{cell}}{\pi e^2} \int_0^{\omega} \sigma_1(\omega')\, \mathrm{d}\omega' \tag{4.13}$$

here m_e is the free electron mass and V_{cell} is the unit cell volume. Fig. (4.2) shows the results of the calculation for $La_{2-x}Sr_xCuO_4$ from Uchida *et al.* [31].

In undoped samples most of the spectral weight is accumulated at energies exceeding the charge-transfer gap, while below $\omega = 1.5\ eV$ $N_{eff}(\omega)$ is flat and almost zero. As doping increases the spectral weight at low frequency increases rapidly as states appear in the gap region. For $x < 0.1$, $N_{eff}(\omega < 1.5\ eV)$ increases faster than x. This is greater than what is expected if one assumes each Sr ion produces a single hole per unit cell with effective mass equal to the free electron

mass. This has been observed in other cuprates [57]. It is evident from the figure that doping affects primarily the states below 3 eV and that spectral weight is transferred from the charge-transfer band to the midinfrared and Drude bands. At doping levels up to 0.2 eV the spectral weight converges at 3 eV, but at higher doping there is an overall decrease. This is in accord with the observation that the spectral weight in the high-T_c materials saturates or even decreases above optimal doping [33]. The reason for this strange behavior is still a mystery.

4.5.2 Midinfrared Band

The midinfrared conductivity has been extracted from optical reflectivity by several authors. Kamarás *et al.* [42] extracted the midinfrared conductivity of Y-123 by employing a two-component fit to the reflectivity at temperatures above T_c and subtracting the Drude component from the total conductivity, and compared it with the total conductivity below T_c. A similar procedure was employed by Reedyk *et al.* to Bi-2212 [58]. Tanner *et al.* [59] used an iterative procedure to extract the free carrier and midinfrared components of Bi-2212, and Gao [9] extracted the midinfrared band of La-214 in a similar way.

The midinfrared band displays a number of common features which are worth mentioning: 1) the band displays an edge which lies in the far infrared between 80–150 cm^{-1} below which the conductivity vanishes 2) a notch-like structure usually between 400–500 cm^{-1} whose strength varies with temperature 3) a broad maximum somewhere between 750 cm^{-1} to 1000 cm^{-1} which shows a fairly large enhancement below T_c as compared to the weak temperature dependence of the band for $\omega > 1500$ cm^{-1}. The notch-like structure has been attributed to a phonon mode resulting from the coupling of bound carriers in the midinfrared to phonons—the charged phonon model. It has been found that the temperature dependence of the midinfrared band may be fitted with a set of Lorentzians by fixing their center frequencies and oscillator strengths while varying the line widths linearly with

temperature as

$$\gamma(T) = \gamma(0) + k_B T. \tag{4.14}$$

This behavior has been investigated by Thomas *et al.* [60] from optical measurements on the cuprate semiconductor Nd_2CuO_{4-x} where a similar behavior is observed. This linear temperature dependence was modelled by considering the interactions of bound electrons with bosons in the antiferromagnetic lattice. A similar temperature variation is observed in the Drude relaxation rate below.

4.5.3 Relaxation Rate

One of the attractive features of infrared spectroscopy is the ability to probe quasiparticle dynamics in the superconducting state. A two-component fit in the normal state combined with a two-fluid fit in the superconducting state allows one to study the variation of the carrier relaxation rate with temperature. Such an analysis of the ab-plane response has been done for Y-123 [42, 30, 61], La-214 [9, 62], and Bi-2212 [41, 63]. In all cases the width of the Drude peak narrows with temperature in a linear fashion as expected from transport measurements. There is little or no temperature dependence of the Drude plasma frequency, so that changes in the observed resistivity can be attributed entirely to a depression if the relaxation rate with decreasing temperature.

Liu [41] has carried out systematic studies of the carrier relaxation rate as a function of doping. The results of such studies are that the carrier scattering rate remains linear in the normal state for underdoped cuprates even at temperatures below the observed pseudogap temperature T^* where characteristic deviations are observed in the ab-plane dc resistivity.

The superconducting state is characterized by a suppression of the quasiparticle scattering rate below T_c. This is a general trend. It is widely believed that a gap is formed in the excitation spectrum responsible for scattering the charge carriers which depresses the scattering rate. One possible candidate is a gap seen

in the spin excitation spectrum (spin gap) by a variety of techinques including: inelastic neutron scattering INS, angle resolved photo emission spectroscopy ARPES, and dc transport, already in the normal state. It is widely believed that this close correlation between the charge and spin response in the cuprates is intimately related to superconductivity.

4.5.4 One-Component Analysis

The one-component analysis—the extended Drude model— has frequently been used to analyze the conductivity of the cuprates [49, 64]. The frequency dependent scattering rate $1/\tau(\omega)$, at room temperature, is found to be almost linear over a very wide frequency range.

A fundamental feature of the one-component analysis of the conductivity is the observation that as the temperature is lowered below room temperature a gap-like depression is observed in the frequency dependent scattering rate of underdoped cuprates. Such a gap is usually associated with a gap which opens up in the underlying bosonic spectrum. A detailed study of the temperature and doping dependence of the ab-plane scattering rate and c-axis conductivity has provided valuable insights into the normal state phase diagram.

There are two separate temperature scales associated with gap formation in the normal state. The upper onset temperature T^* corresponds to the onset of a depression of the c-axis conductivity and is also seen in as a gap in the Knight shift [65] in NMR measurements. A normal state gap of $d_{x^2-y^2}$ spmmetry is also observed at the same temperature by ARPES, which is similar to that observed in the superconducting state [66, 67]. This gap in the density of states is a true gap. It also appears as a weaker depression of the low frequency ab-plane scttering rate extracted from the extended Drude model. The lower temperature scale T_s is usually a few degrees above T_c in underdoped samples and is marked by a reduction in the NMR relaxation rate $1/T_1T$. The temperature T_s is associated

with the observation of a 41 meV neutron resonance in Y-123 at optimal doping. This represents a true spin gap which corresponds to an ordered spin state. The scattering rate shows a much stronger depression below T_s than that observed just below T^*; charge transport then becomes coherent. It is found that the pseudogap temperatures merge with T_c in the optimal to overdoped regions of the phase diagram, where only one gap structure below T_c is then observed. In contrast, Bi-2212 appears to exhibit a pseudogap even in the overdoped state. The scattering rate at high frequency also becomes superlinear. The linear scattering rate at high frequency is independent of temperature in the underdoped case, develops a weak temperature dependence at optimal doping, and becomes strongly temperature dependent in the overdoped regime where it becomes superlinear. A review of the current state of affairs with respect to the normal state phase diagram can be found in the most recent review by Basov *et al.*

Finally, the appearance of superconductivity does not lead to any marked changes in the gap feature in the scattering rate. The feature increases in depth without any noticeable shift in frequency. This highlights the marked similarities between the normal and superconducting states, and the unconventional nature of the gap feature seen in these materials.

4.5.5 c-Axis Conductivity

The evolution of the c-axis conductivity with doping has been investigated by Uchida *et al.* [68] for La-214, and Cooper *et al.* [32], Homes *et al.* [69, 70] and Bernhard *et al.* [71] for Y-123. The c-axis conductivity has a large number of phonon modes which remain relatively strong up to very high doping levels. There are a number of features worth mentioning; which are distinctly different from the corresponding evolution of the in-plane conductivity with doping: 1) there are no features in the conductivity of the insulating parent compounds which can be identified with a charge transfer gap, 2) for La-214 doping leads to a transfer of

spectral weight from the 5–6 eV range to lower frequencies which forms a broad peak near 2 eV, and a region of lower conductivity below 0.25 eV which does not show a Drude upturn until it is overdoped 3) the 2 eV peak position does not soften with doping 4) the overall magnitude of the electronic conductivity is much smaller than the corresponding ab-plane conductivity, so phonons remain quite strong even into the overdoped regime.

The variation of the electronic contribution to the c-axis conductivity with temperature has been studied by the above authors. It has been found that in the underdoped cuprates the electronic c-axis conductivity is fairly flat at room temperature, but develops a gap at lower frequencies below the pseudogap temperature T^*. The conductivity is semiconducting, and the depth of the gap structure increases with decreasing temperature. A transition into the superconducting state leads to a further depression of the gap. It is observed that the conductivity remains finite down to the lowest temperatures. This pseudogap structure is much harder to discern in La-214 than in Y-123 owing to the smaller magnitude of conductivities in La-214.

At higher doping levels corresponding to optimally and overdoped regimes the conductivity become more metallic in character. A Drude upturn can now be discerned at low frequency and the conductivity first increases with decreasing temperature above T_c at low frequency and then decreases in the superconducting state as the condensate forms. This is similar to what is observed for the ab-place conductivity. A fit of the conductivity to an extended Drude model shows that the scattering rate along the c-axis is so large as to cause the transport along the c-axis to be incoherent. The mean free paths for c-axis transport would be comparable to the unit cell dimensions in the cuprates. The gap feature which is observed in the underdoped case above T_c now appears below T_c.

4.6 Conclusion

There appear to be a number of features which are common to the carrier dynamics of the cuprates at low frequencies. The growth of spectral weight in the mid and far infrared spectral regions with doping and the appearance of superconductivity are the most salient features. The analysis of optical data within the framework of a variety of models, over a wide doping and temperature range have allowed a fairly precise characterization of the normal state phase diagram.

At this point there is no comprehensive theory of the superconducting state. Two-fluid studies of the ab-plane quasiparticle dynamics below T_c have revealed a strong suppression of the quasiparticle scattering rate. This can be compared with the corresponding depression of the frequency dependent scattering rate which begins even in the normal state in underdoped samples. There is a sizeable quasiparticle spectral weight in the conductivity at low temperatures which has sparked debate about the symmetry of the superconducting gap in these materials. In spite of considerable effort no feature in the measured conductivity can be identified with a gap as was done for conventional superconductors. The issue of high-T_c superconductivity is a work in progress and infrared spectroscopy continues to be of paramount importance.

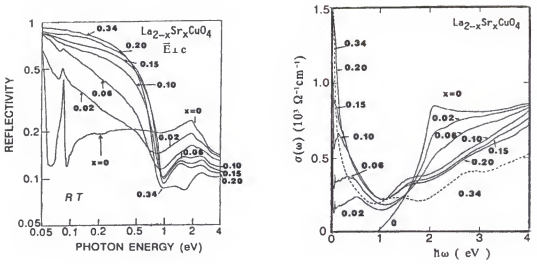

Figure 4–1: Room temperature ab-plane reflectivity and optical conductivity $\sigma(\omega)$ at various doping levels for single crystals of $La_{2-x}Sr_xCuO_4$. Both scales of the reflectivity figure are logarithmic (see ref. [31]).

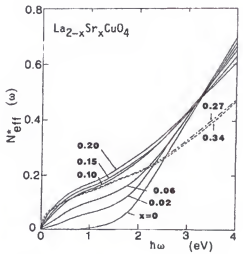

Figure 4–2: Effective number of carriers per unit cell for single $La_{2-x}Sr_xCuO_4$ crystals at various doping levels. The data for the heavily doped samples $x = 0.27$ and $x = 0.34$ are shown as dot-dashed and dashed curves (see ref. [31]).

CHAPTER 5
SAMPLE PREPARATION AND EXPERIMENTAL TECHNIQUES

5.1 Introduction

Two types of $YBa_2Cu_3O_{6+x}$ high-T_c superconducting thin films were investigated in this work; both films are c-axis oriented, with their c-axis perpendicular to the substrate surface. The first film is grown on a sapphire substrate, while the second is grown on a MgO substrate. This chapter deals with the details of the sample preparation processes and the characterization of the films by dc transport. This will be followed by a description of the optical experiments both with and without a transport current flowing through the films.

5.2 $YBa_2Cu_3O_{6+x}$ Film on MgO

The Y-123 films on MgO substrates were prepared by R. Hadfield at NIST. The films were deposited by pulsed laser deposition from a stoichiometric target of Y-123 [72]. The process begins with polished MgO substrates of approximately 15 mils thickness, with length and width 12 mm. Conducting silver paste was used to affix the substrate to a heater block. The deposition was carried out under vacuum with the substrate temperature raised to 770 °C, with a background O_2 pressure of 600 mTorr. A 120 mJ excimer laser operating at a repetition rate of 10 Hz for 54 seconds (two complete passes) was used to ablate the stoichiometric target onto the heated substrate block. The chamber was then flooded with O_2 while the sample was slowly cooled, to ensure optimal doping. The resulting film thickness was measured to be 500 ($\pm$20 Å) using step height profilometry.

The chamber was then vented and two gold electrodes were deposited by dc magnetron sputtering through an aluminum mask. Both electrodes were approximately 2 mm wide and 1200 Å thick and were used as current electrodes

(see fig. 5–3 (b)). The samples were then polished to remove the silver paste from the substrate. A dummy sample consisting of bare MgO substrate was also produced under similar conditions in order to account for the effects of the substrate in the infrared spectra. Finally, two silver electrodes, about 2000 Å thick and 2mm × 2mm were sputtered by the current author to facilitate voltage measurements (see fig. 5–3 (b)). The properties of the samples are summarized in table 5–1.

The measured ab-plane resistivity of one of the $YBa_2Cu_3O_{6+x}$ films is shown in the upper panel of fig. 5–1. The film exhibits a sharp superconducting transition near 86 K, and displays a linear resistivity of the form $\rho(T) = \rho_0 + \alpha T$ above 100 K, where $\alpha = 1.097\ \mu\Omega$ cm/K with an extrapolated intercept $\rho_0 = 38.819\ \mu\Omega$ cm.

The advantages of MgO as a substrate for the growth of thin Y-123 films are twofold. Firstly, the underlying cubic crystal structure of MgO facilitates epitaxial growth of Y-123. The following epitaxial relationship has been found, Y-123 [100](001)‖MgO [100](101) [73]. Secondly, MgO is reasonably transparent in the far infrared up to 330 cm^{-1} at low temperatures, which makes it ideal for optical transmittance measurements.

Table 5–1: $YBa_2Cu_3O_{6+x}$ thin film characteristics.

Thickness (Å)	Area (mm^2)	T_c (K)	ΔT_c (K)	Buffer layer	Substrate
500 Å	12×12	86	1.5	none	MgO
600 Å	10×10	86	1.5	Cerium oxide (200Å)	Sapphire (Al_2O_3)

5.3 $YBa_2Cu_3O_{6+x}$ Films on Sapphire

The Y-123 films on sapphire substrates were supplied by the research group at Conductus. The films were deposited on the R-plane with a thin ≈ 200–300 Å buffer layer of cerium oxide (CeO_2) by thermal evaporation (TE). The film thickness was about 600Å deposited on a 0.3 mm thick sapphire substrate.

There are two main orientations of sapphire which are commonly used to grow Y-123 films; the M-plane $(10\bar{1}0)$ and the R-plane $(1\bar{1}02)$, both referenced with respect to hexagonal axes. The hexagonal (trigonal) crystal structure of sapphire makes it anisotropic. The optic axis lies in the M-plane, but at an angle of 57.5667° to the R-plane [74]. This makes R-cut sapphire inconvenient for the growth of Y-123 films in cases where the dielectric anisotropy is undesirable. The following epitaxial relationships exist for CeO_2 buffered Y-123 films on sapphire substrates: $CeO_2[110](001) \parallel Al_2O_3[10\bar{1}1](1\bar{1}02)$ and Y-123$[100](001) \parallel CeO_2[110](001)$ [75]. The main advantages of sapphire substrates are their hardness, resistance to corrosive chemicals and high thermal conductivity comparable to that of copper at cryogenic temperatures. They are also very transparent at low temperature in the far infrared region below 350 cm^{-1}.

The resistivity of the film as a function of temperature was measured using a standard 4-probe ac technique. The lower panel of fig. 5–1 shows that the superconducting transition is fairly sharp with $T_c = 86$ K. Above 100 K the resistivity follows a liner law $\rho(T) = \rho_o + \alpha T$ similar to that found for the films on MgO substrates but with a higher normal state resistivity. Table 5–1 summarizes the characteristics of the film.

5.4 Experiment

5.4.1 Cryogenic Apparatus

In order to perform infrared spectroscopic measurements at cryogenic temperatures, it is necessary to cool and regulate the temperature of the sample under investigation. The samples are usually glued to the back surface of an oxygen-free copper plate with a tapered hole (see fig. 5–2). Oxygen-free copper has a very low brittle point and high thermal conductivity which makes it ideal for low temperature applications.

There are four main parts of the cooling system: a flow cryostat, helium dewar, transfer line and temperature controller. All parts work in tandem to maintain a stable sample temperature. The sample plates are mounted onto a screw-on attachment which screws into the cryostat cold finger. A small silicon diode thermometer is inserted into a small hole drilled into the sample holder which measures the temperature. To reduce the effects of thermal radiation heating, a metal shield is screwed onto the cold stage of the cryostat. The whole arrangement is inserted into a shroud which is part of the reflectivity or transmittance stage. The shroud is sealed with infrared transparent windows which allow light to reach the sample. The shroud is then evacuated to a pressure 10^{-4} Torr or less. Helium gas is then transferred from the helium dewar to the cryostat through the transfer line. This gas flow cools the cold finger and hence the sample by conduction. The temperature is maintained at a set value by a temperature controller which reads the temperature of the diode thermometer and supplies the requisite power to a heater on the cold finger. Depending on the desired rate of cooling the helium flow rate may be increased or decreased by a flow meter which regulates the flow through the cryostat. The model temperature controller used in this work, the Lakeshore model 330 auto-tuning temperature controller, automatically adjusts the control parameters at each temperature and gives fairly stable temperatures within 0.01 K. The diode thermometer when well calibrated has an accuracy of $\pm$ 1 K.

5.4.2 Reflectivity Measurements

The reflectivity measurements on the Y-123 samples were performed on the Bruker 113-V FTIR spectrometer (see fig. 3–2 p. 35). The measurements were confined to the far infrared range 35–350 cm^{-1}, and to temperatures between 300 and 40 K. The sample was mounted on a holder similar to that shown schematically in fig 5–2(b). An aluminum mirror, consisting of 2000 Å of aluminum deposited on a microscope slide served as a reference. The reference was affixed to a plate

of the same dimensions as the sample holder. Both sample and reference holders were mounted on the cryostat in a way which allowed them to be interchanged in the infrared beam (see fig. 5–2 (a)). An arc lamp (Hg-arc) was used as a light source and a helium cooled bolometer as a detector. The absolute reflectivity is found by dividing the measured spectrum of the sample in the beam by that of the reference mirror in the beam. Although the absolute reflectivity of aluminum is not 100 % it is greater than 99 % over a very wide frequency range extending into the near infrared. The measured reflectivity is corrected by multiplying it by the absolute reflectivity of the reference. The reflectivity of the bare MgO substrate was also measured to account for substrate effects in the data for the film on MgO. Similarly, one of the films on sapphire was etched with nitric acid, and the reflectivity of the CeO_2/sapphire combination was measured. Chapter 6 deals with the difficulties encountered in trying to analyze both the film/CeO_2/sapphire data and the CeO_2/sapphire data for anisotropic R-plane sapphire.

5.4.3 Transmittance Measurements

The transmittance of both films, and their substrates were also measured at the same temperatures and over the same frequency range as the reflectivity. The transmittance is found in a similar manner to the reflectivity. Fig. 5–3 (a) shows the schematic setup for transmittance. The sample, and empty aperture which now serves as a reference, are mounted at right angles on the tip of the rotating cryostat. The absolute transmittance is determined by dividing the measured single beam spectrum of the sample by that of the empty reference hole. The transmittance, unlike the reflectivity is measured at near normal incidence. The angle of incidence for the reflectivity measurements described in the previous section is about 11°.

To investigate the effects of transport currents on the superconducting state electrodynamics, surface electrodes for both current and voltage were sputtered

onto both films. The process used for the deposition, and the arrangement of electrodes for the film on MgO was previously described, and is shown in fig. 5–3 (b). The film on sapphire was also patterned using a small amount of dilute nitric acid and a paper mask cut into the form of a half cross. The geometry of the patterned film is shown in fig. 5–3 (b). The two outer silver electrodes used to carry current were 2 mm wide, 5 mm long and 2000 Å thick. Each of the voltage electrodes is 2mm long, 1mm wide and 2000 Å thick. The center to center distance between the voltage electrodes is about 3 mm. The center to center distance between the voltage electrodes for the film on MgO is about 4 mm. Two current sources were used to supply current, together they covered a range from 1 nA–1 A. The Kiethly model 220 programmable current source covers the lower range 1 nA–100 mA and the model 228 current-voltage source covers the range 4 mA–1 A. Voltage measurements were made with a Kiethly model 195 digital multimeter. Contact was made by soldering gold wire to the electrodes using indium solder and a low temperature soldering iron. Indium is known to produce contacts of much lower resistance than silver epoxy.

The electrooptic transmittance was performed in two separate regimes; near T_c at 75 K and at low temperature—40 K. In order to ensure that the samples were in the superconducting state near T_c the samples were cooled to 80 K and a small current of about 1 μA was passed through the films and the voltage reading on the multimeter was observed. It was found that in both cases there was a voltage reading, which may be related to the possibility that the film may be at a slightly higher temperature than the sample holder. The temperature was further reduced to 75 K and the procedure was repeated. The voltage reading on the multimeter was now zero; implying that the films were in the superconducting state.

The transmittance of the film on MgO was measured as a function of current at 75 K at 25, 75 and 200 mA. The voltage was observed each time. The current

was also increased to 300 mA at which point the substrate cracked. This may be as a result of ohmic dissipation at the contacts which produced a temperature gradient between the film side and backside of the substrate which caused the substrate to crack. The same procedure was carried out for the film on sapphire at 75 K except that the currents passed were 1, 5, 10, 15 and 20 mA, since the critical current was between 10 and 15 mA. The results of both these measurements are presented in chapter 7.

The transmittance of the film on sapphire was also measured as a function of current at 40 K. Four currents of 50, 80, 100 and 150 mA were passed. At 150 mA the voltage began to increase rapidly, far beyond that expected for the resistive state at the same temperature—which appeared to be a sign of contact heating. This will also be discussed in greater detail in chapter 7.

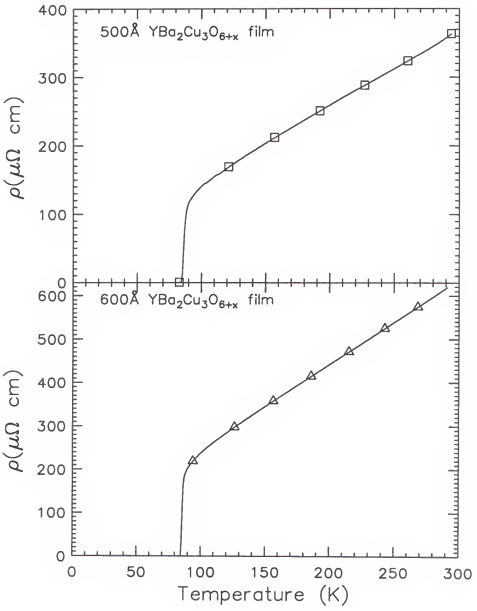

Figure 5–1: The temperature dependent resistivity of two $YBa_2Cu_3O_{6+x}$ films. Upper panel: the ab-plane resistivity as a function of temperature for a 500 Å $YBa_2Cu_3O_{6+x}$ film on a MgO substrate. Lower panel: the ab-plane resistivity of a second $YBa_2Cu_3O_{6+x}$ film, 600 Å thick, on a sapphire substrate.

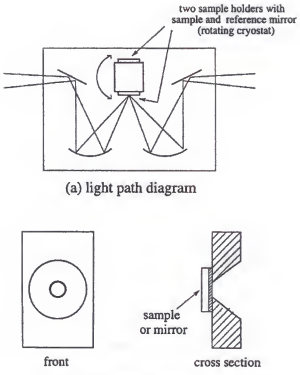

Figure 5–2: Reflectivity stage and sample holders used in this experiment. (a) A schematic diagram of the reflectivity stage and light path showing light incident on rotatable sample holders. (b) A schematic diagram of the oxygen free copper holder used to mount samples.

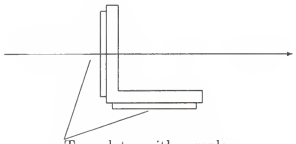

(a)

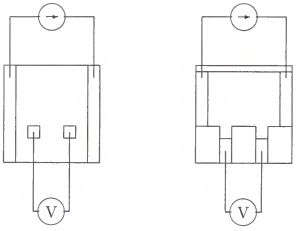

(b) (c)

Figure 5–3: A schematic of the transmittance holder and electrode configuration for transmittance measurements. (a) Schematic diagram of light path for transmittance measurement. (b) Surface electrode configuration used for infrared electrooptic measurements for Y-123 films on MgO. (c) Patterned half-cross and surface electrode arrangement used for infrared electrooptic measurements of Y-123 on sapphire.

CHAPTER 6
FAR-INFRARED STUDIES OF $YBa_2Cu_3O_{6+x}$ FILMS

6.1 Introduction

This chapter deals with a detailed characterization of the far-infrared properties of the two Y-123 thin films which were described in the previous chapter. Both the reflectivity $\mathcal{R}(\omega)$ and transmittance $\mathcal{T}(\omega)$ were measured over a frequency range of 40–350 cm^{-1} and over a temperature range from 40–300 K. The characteristics of both films have been listed in table 5–1 on p. 57; while the dc transport properties are shown in fig. 5–1 on p. 63. The films are highly ab-plane oriented, and the E-field of the incident light lies within the plane. All the optical properties which are reported here are therefore ab-plane averages.

The dielectric properties of the film on magnesium oxide in the normal state above T_c are analyzed within the framework of a simple two-component model. We have been able to obtain fairly good fits to the transmittance by assuming that the low frequency response is dominated by a free-carrier Drude band, while the response at higher frequency is influenced primarily by a very broad midinfrared band which is fitted with a series of Lorentzians. The results obtained from this two-component approach agree very well with the results obtained from the Kramers-Kronig analysis of high quality single crystals. Below T_c the dielectric features of the superconducting state are studied with a two-fluid model. In this model, part of the spectral weight associated with the Drude band is transferred to the condensate, which appears as a pole in the conductivity at zero frequency. The midinfrared band is found to be fairly temperature independent.

The film on sapphire will also be discussed. The chief drawback of the analysis is the difficulty of extracting the optical constants of the film independently of the

substrate. Due to the anisotropy of sapphire, a uniaxial transmittance model similar to that described in section 2.4 is used to fit the substrate transmittance data. The fits to this model are in reasonable agreement with the measured data, over a wide frequency range. The generic features of both the normal and superconducting states of this film on sapphire are shown to be quite similar to those of the film on MgO. The normal state data of this film was fitted using a two-component model, and a two-fluid model was used to analyze the superconducting state data. The results of this analysis will be discussed in later sections.

6.2 Results and Discussion

6.2.1 MgO Substrate

Magnesium oxide possesses complex temperature-dependent lattice vibration spectra in the far-infrared region. We concentrated on the low frequency region below 350 cm^{-1}, as MgO is opaque at all temperatures above this frequency due to a strong infrared active transverse optic (TO) phonon mode near 400 cm^{-1}. The measurements were made at 2 cm^{-1} resolution, and the fringes due to the multiple internal reflections in the substrate were carefully smoothed.

Fig. 6–1 shows the measured reflectivity and transmittance of a 0.3 mm thick MgO substrate at several temperatures. Below 100 cm^{-1} the absorption is small at all temperatures, as the transmittance approaches 60% while the corresponding reflectivity approaches 40%. The transmittance in the region extending from 100 cm^{-1} to about 300 cm^{-1} shows a very marked temperature dependence. The spectra are characterized by structure near 100, 150 and 290 cm^{-1} which have been assigned to two phonon difference band processes which lead to strong absorption at room temperature, and which are frozen out at lower temperatures. In these processes a photon is absorbed, and an acoustic phonon is annihilated with the creation of an optic phonon. The possible assignments which correspond to regions where the phonon densities of states are large are the W-point TA—TO transition

at 90 cm^{-1}, the X′-point LA—LO transition at 95 cm^{-1} and the X-point TA—TO transitions at 150 and 255 cm^{-1}. As the temperature is lowered there is an overall increase in both the the transmittance and the reflectivity as the multiphonon processes are suppressed. The reflectivity near 350 cm^{-1} is fairly insensitive to temperature as is expected for a strong TO mode which dominates the reflectivity above this frequency.

In order to account for the complex MgO absorption processes which appear in the measured spectra for the film on MgO, we fitted the substrate transmittance with a large number of Lorentzians. The frequency dependent dielectric function $\epsilon(\omega)$ was assumed to have the form

$$\epsilon(\omega) = \epsilon_\infty + \sum_j \frac{S_j \omega_j^2}{\omega_j^2 - \omega^2 - i\omega\gamma_j}, \tag{6.1}$$

where ϵ_∞ is the high frequency dielectric constant, S_j is the mode strength, ω_j is the mode frequency and γ_j is the damping constant. The high frequency dielectric constant ϵ_∞ was fixed at 3.01 at all temperatures as was done in ref. [76]. We initially started with the parameters which were suggested by ref. [76] but we found that it was impossible to obtain good fits in the multiphonon spectral region without introducing additional oscillators. This prescription of simulating the multiphonon difference band processes by a large number of Lorentzians allowed us to account for the substrate effects in the film data. Table 6–1 shows the oscillator parameters which were used in the fits to the substrate transmittance data at all temperatures. The mode strengths in eqn. (6.1) are written in terms of a plasma frequency $\omega_{pj} = \omega_j\sqrt{S_j}$ in the table. The lower panel of fig. 6–1 shows the fits to the substrate transmittance data using this procedure.

6.2.2 Sapphire Substrate

In contrast to MgO, sapphire belongs to a trigonal (hexagonal) crystal system. This implies that any macroscopic quantity such as the dielectric constant is

described by a 2nd-rank-tensor which has two independent parts. A complete characterization of the dielectric response requires two independent measurements of $\epsilon(\omega)$; one with the electric field parallel to the crystalline c-axis and the other with the electric vector anywhere in the plane perpendicular to the c-axis, since all such directions are optically equivalent. The particular cut used here—R-cut sapphire— makes it impossible to perform such a characterization by polarized optical measurements. The c-axis (optic axis) makes an angle of 57.5667° with the R-plane. We performed unpolarized reflectance and transmittance measurements below 350 cm^{-1}, since sapphire has a large number of infrared active phonon modes above 380 cm^{-1} and is opaque above this frequency. The basic theory of light propagation through an anisotropic crystal, based on a uniaxial transmittance model at normal incidence was presented in chapter 2. Here, we will concentrate mainly on the transmittance, as these measurements are done at more near normal incidence, which was assumed in the theory.

The measured reflectivity and transmittance of a thin CeO_2 buffer layer (300 Å) on a 0.5 mm thick sapphire substrate are shown in fig. 6–2. The fringes, which have not been smoothed, are due to multiple internal reflections which occur within the sapphire substrate. The figure shows that below 100 cm^{-1} the average reflectivity approaches 40% while the average transmittance approaches 60%. This implies that there is little absorption at very low frequency at all temperatures. A salient feature of all the spectra is the appearance of beats which increase in contrast and extend to higher frequencies as the temperature is lowered. The beats result from a superposition of two oscillatory terms in the reflectivity or transmittance associated with different components of the dielectric tensor. The peak in the reflectivity and the dip in the transmittance at about 272 cm^{-1} corresponds to a single infrared active TO phonon mode in the CeO_2 buffer layer [77–81].

As was observed in the case of MgO the transmittance above 100 cm^{-1} increases drastically as the temperature is lowered from room temperature to 40 K; while the increase in the reflectivity is less drastic over the same temperature range. This drastic suppression of the absorption above 100 cm^{-1} with decreasing temperature, may be related to multiphonon difference-band processes in the sapphire substrate similar to those observed in MgO. The main obstacle to any analysis of the optical data in this frequency range is the lack detailed studies of sapphire over this range [82–85]. The majority of the previous infrared studies were focussed on the phonon modes in the frequency range above 380 cm^{-1} [86–88].

Sapphire belongs to the $D_3^6 d$ space group. Group theory predicts 4 infrared active phonon modes of E_u symmetry for the electric field perpendicular to the c-axis (o-ray), and 2 infrared active modes of A_{2u} symmetry for the E-field parallel to the c-axis (e-ray). We represented the dielectric functions of the o and e waves by Lorentz models of the form

$$\epsilon(\omega)_{o,e} = \epsilon_\infty + \sum_j \frac{S_j \omega_j^2}{\omega_j^2 - \omega^2 - i\omega\gamma_j}, \tag{6.2}$$

where $\epsilon_{o,e}$ is the dielectric function for the o or e wave, ϵ_∞ is the high frequency dielectric constant, S_j is the oscillator strength, ω_j is the mode frequency, and γ_j is the damping constant. We tried to fit the transmittance of CeO_2 on sapphire using the parameters suggested in ref. [79] for CeO_2 and the parameters in ref. [88] for sapphire. All four infrared active phonon modes as well as two electronic bands at higher frequency were included in ϵ_o; while the two predicted modes, and two electronic bands were included in ϵ_e. In addition to these, we added a broad oscillator to ϵ_o at low frequency and centered at 209 cm^{-1} to account for the strong absorption, particularly at higher temperatures. The choice of the center frequency of this extra mode was motivated by the observation of a weak dip in the transmittance at approximately the same frequency. This can be seen most easily

in the 300 and 200 K spectra in the lower panel of fig. 6–2. We found that it was not possible to fit the substrate transmittance without including this broad mode at all temperatures.

The fits to the transmittance are shown in fig. 6–3 along with the measured data, which is repeated here for the sake of comparison. Tables 6–2–6–4 show the parameters which were used in the fits to the sapphire substrate and CeO_2 buffer layer at all temperatures. The fits to the data replicate the beat pattern quite accurately, although the fringe contrast of the fits is greater than the actual data at all temperatures. The difference is larger at lower temperature where the sapphire absorption is lower and the dispersive nature of the substrate dominates. The main reason for this is that the fits assume that the measurement was done at infinite resolution. The actual data was measured at 1 cm^{-1} resolution and so the fringe contrast is lower. In the frequency range between 250 and 270 cm^{-1}, just below the CeO_2 mode the fits differ by 1–2%. This may be obscured by the fringes in fig. 6–3. The fits fall slightly below the data in this frequency range. The difference is less severe at lower temperatures. The fitted transmittance in this region is fairly sensitive to the parameters of the broad mode which was introduced at 209 cm^{-1} to account for the extra absorption at higher temperatures. This difference between the fits and the actual data of the sapphire substrate will lead to errors in the extracted optical constants of the film data.

6.2.3 $YBa_2Cu_3O_{6+x}$ on MgO

The measured reflectance and transmittance of the 500 Å film on MgO are shown in the upper and lower panels of fig. 6–4. The reflectivity falls well below unity at all frequencies in the normal state. As the temperature is lowered the reflectivity below 150 cm^{-1} increases drastically, and approaches unity at the two lowest temperatures in the superconducting state. The reflectivity at all temperatures is fairly flat and featureless, which can be attributed to the strong

free carrier contribution at all temperatures. The free carriers screen the phonons which are normally observed in the substrate and in the film. The transmittance is, however, much lower and never exceeds 10% at any temperature. The spectra, unlike the reflectivity are characterized by significant structure, which is due to the phonons in the MgO substrate. As the temperature is lowered, the transmittance below 100 cm^{-1} is reduced and approaches zero in the superconducting state for $T < T_c$.

6.2.4 $YBa_2Cu_3O_{6+x}$ on Sapphire

Fig. 6–5 shows the raw reflectivity and transmittance of the 600 Å film on sapphire at several temperatures. The spectra have not been smoothed and are characterized by beats below 270 cm^{-1}. The beats are due to multiple internal reflections in the sapphire substrate as was described earlier. The peak in the reflectivity—and dip in the transmittance—at about 272 cm^{-1} corresponds to a phonon mode in the underlying CeO_2 buffer layer. At room temperature the fringe-averaged low frequency reflectivity is about 55%. The overall reflectivity increases at lower temperatures, with the low frequency reflectance showing an upturn which approaches 100% at 40 K in the superconducting state. The onset of superconductivity below T_c may also be inferred from the changes in the low frequency characteristics of the fringe pattern in the reflectivity. The fringe contrast below 100 cm^{-1} is strongly depressed at the two lower temperatures, 80 and 40 K in the superconducting state as compared to the fringe contrast in the normal state. The transmittance at room temperature increases steadily below the infrared edge of transparency of the substrate, up to about 17% at the lowest frequency. There is a reduction of the transmittance below 100 cm^{-1} at lower temperatures with the transmittance approaching zero below T_c. At higher frequency the transmittance is enhanced at low temperature as the substrate becomes more transparent.

6.2.5 Two-Fluid Model

In order to account for the frequency and temperature dependence of the observed transmittance of both films, we have employed a two-component model in the normal state and a two-fluid model in the superconducting state. The models have been outlined in chapter 4.

The two-component model assumes that the complex dielectric function of the film is composed of three terms: a narrow Drude band centered at zero frequency, a number of broad Lorentzians in the midinfrared, and a high frequency contribution. The dielectric function may then be written as:

$$\epsilon(\omega) = \epsilon_D(\omega) + \epsilon_L(\omega) + \epsilon_\infty \qquad (T > T_c), \tag{6.3}$$

where $\epsilon_D(\omega)$ is the Drude term, $\epsilon_L(\omega)$ is a sum of Lorentzians which are centered in the midinfrared and which account for the broad midinfrared absorption, and ϵ_∞ is the high frequency term which accounts for excitations at frequencies exceeding 10,000 cm^{-1}.

In the superconducting state it is assumed that a certain fraction of the Drude carriers condense to form the superconducting condensate, while the effect on the midinfrared band is negligible. We have used a two-fluid model dielectric function of the form:

$$\epsilon(\omega) = (1 - f_s)\epsilon_D(\omega) + f_s\epsilon_S(\omega) + \epsilon_L(\omega) + \epsilon_\infty \quad (T < T_c), \tag{6.4}$$

where $\epsilon_D(\omega)$, $\epsilon_L(\omega)$ and ϵ_∞ are the same as the normal state values in eqn. 6.3, while f_s is the fraction of the free carrier density which condenses and

$$\epsilon_S(\omega) = -\frac{\omega_{pD}^2}{\omega^2} + i\frac{\pi\omega_{pD}^2}{2\omega}\delta(\omega). \tag{6.5}$$

The plasma frequency ω_{pD} here is the same as the the Drude plasma frequency in the normal state.

The fits to the transmittance of the film on MgO, and the film on sapphire are shown in the lower panel of fig. 6–4 and in fig. 6–6 respectively. In each case a single Drude oscillator with plasma frequency ω_{pD} and damping $1/\tau$ and three Lorentzians with parameters $(\omega_{pj}, \omega_j, \gamma_j)$ where ω_{pj}, ω_j and γ_j are the plasma frequency, center frequency and damping of the jth Lorentzian were used to fit the transmittance. We used the parameters suggested by reference [3] for the Lorentzian oscillators and also fixed $\epsilon_\infty = 25$ as was done in ref [9]. We obtained fairly good fits at all temperatures for the film on MgO by varying only ω_{pD}, $1/\tau$ and f_s as well as the damping γ_1 of the lowest midinfrared oscillator while fixing the remaining midinfrared parameters. It was also found that ω_{pD} and γ_1 were fairly independent of temperature, within experimental uncertainty. The parameters which were used to fit the film data in the normal and superconducting states are shown in tables 6–5 and 6–6.

A similar procedure was applied to the film on sapphire, and as can be seen in fig. 6–6 the fits are reasonably good at all temperatures. The fringe pattern of the raw data is nearly centered on the fringe pattern of the fits. In these fits all the midinfrared parameters were fixed, while the Drude plasma frequency ω_{pD}, scattering rate $1/\tau$, and superfluid fraction f_s in the superconducting state were varied to achieve the best least squares fit to the data. It is nearly impossible to fit the fringe pattern very accurately. This can lead to substantial errors in some of the oscillator parameters used to fit the film data. In particular, the damping constant γ_1 of the lower midinfrared oscillator at center frequency 290 cm^{-1} will accumulate substantial errors if it is varied to achieve better fits in this region.

Tables 6–7 and 6–8 shows some of the oscillator parameters which were used to fit the transmittance of the film on sapphire. The Drude plasma frequency of the film on sapphire is almost 40% lower than the plasma frequency of the film on MgO. There are two main reasons for this. One reason for the difference is

associated with the uncertainties in the film thicknesses which are used in the fits. Such uncertainties produce errors in the the plasma frequencies of the oscillators used in the fits. Another possible cause of the discrepancy may simply be the higher quality of the film grown on MgO.

6.2.6 Free Carrier Relaxation and Condensate

The observed changes in the reflectivity and/or transmittance of the films with temperature can be easily understood in terms of the strong temperature dependence of the optical conductivity. Fig. 6–7 shows the real and imaginary parts of the optical conductivity of the film on MgO extracted from the two-component fits to the transmittance. The real part of the optical conductivity $\sigma_1(\omega)$ at frequencies below 200 cm^{-1} increases as the temperature is lowered in the normal state. This transfer of spectral weight to lower frequencies is due to a linear decrease in the free carrier relaxation rate $1/\tau$ with temperature. The transmittance in the normal state is strongly influenced by $\sigma_1(\omega)$ which dominates the inductive response $\sigma_2(\omega)$. The enhanced low frequency conductivity at lower temperatures leads to a corresponding decrease in the low frequency transmittance. At temperatures below T_c the onset of superconductivity is marked by a strong enhancement of $\sigma_2(\omega)$ due to the formation of the condensate. There is a transfer of spectral weight to the origin which forms a delta function in $\sigma_1(\omega)$ which represents the response of the condensate. This redistribution of spectral weight leads to a suppression of $\sigma_1(\omega)$ at low frequencies as predicted by the sum rule. Since the real and imaginary parts of the conductivity are related by causality a delta function in the real part of the conductivity produces a $1/\omega$ dependence in the imaginary part. As $\omega \rightarrow 0$, $\sigma_2(\omega)$ approaches zero in the normal state while it diverges as A/ω in the superconducting state where it now dominates $\sigma_1(\omega)$. The quantity A is related to the strength of the condensate and the London penetration depth. The observed downturn of the transmittance in the superconducting state,

shown in fig. 6–4 is due to the $1/\omega$ dependence of $\sigma_2(\omega)$, which represents the screening effect of the condensate. Fig. 6–8 shows the corresponding conductivities of the film on sapphire. The only difference between this film and the film on MgO are the lower levels of the conductivities of this film. This is associated with the lower free carrier densitiy of this film which is reflected in the lower Drude plasma frequency ω_{pD}.

We have extracted the temperature dependent scattering rate of both films. The scattering rates were calculated from the measured four-probe resistivities using the equation:

$$(1/\tau)_{dc} = \frac{\omega_{pD}^2}{4\pi}\rho_{dc}. \tag{6.6}$$

The results are shown in fig. 6–9 where we have also shown the relaxation rates obtained directly from the two-component fits. The figure shows that the free carrier relaxation rate varies linearly with temperature in the normal state. This is a unique property of the carrier dynamics of the cuprates. The infrared also probes the quasiparticle relaxation rate below T_c which is invisible to dc transport. The symbols in the figure show that the carrier relaxation rate extracted from a two-fluid fit falls faster than linearly below T_c. Such behavior has previously been observed for $YBa_2Cu_3O_{6+x}$ [61] and $Bi_2Sr_2CaCu_2O_8$ [63]. It is widely believed that the suppression of the scattering rate below T_c is related to a gap which opens up in the excitation spectrum which is responsible for scattering the free carriers. The close correspondence in the energy scales of characteristic features which appear in the charge and spin response of the cuprates, suggests that the spin excitation spectrum may be responsible for this unusual behavior. The spin excitation spectrum becomes gapped at a temperature close to T_c in the optimally doped cuprates.

The lower panel of fig. 6–9 shows the temperature dependence of the superfluid fraction $f_s(T)$. Above T_c $f_s = 0$, and increases as the temperature drops below

T_c. The symbols in the figure are the superfluid fractions extracted from the two-fluid fits to the transmittance data in the superconducting state of both films. The solid and dashed curves are fits to the data using an empirical Gorter-Casimir two-fluid model of the form $f_s(T) = f_s(0)(1 - (T/T_c)^4)$, with $T_c = 86$ K. The fits show that even at low temperatures f_s is still much less than unity, with $f_s(0) = 0.66$ for the 500 Å film and 0.52 for the 600 Å film. It means that a sizeable fraction of the carriers do not condense. This is a universal feature of all the cuprates. This residual conductivity which remains at low temperatures in the superconducting state of the cuprates is still the subject of intense debate.

6.3 Summary

We have presented the results of optical reflectivity and transmittance measurements of thin $YBa_2Cu_3O_{6+x}$ films in the far-infrared region below 350 cm^{-1}. The transmittance of both films was fitted with a two-component model, with a Drude free-carrier response in the normal state, and a two-fluid model in the superconducting state. The Drude scattering rates extracted from the fits show a T-linear variation in the normal state and a more rapid drop just below T_c, while the Drude plasma frequency is nearly temperature independent. It was found that fairly good fits could be obtained by fixing the midinfrared absorption at all temperatures. The superfluid fraction extracted from the two-fluid fits below T_c increases with decreasing temperature, but a sizeable fraction of the carriers do not condense even at 40 K.

The fits to the film on sapphire were complicated by the optical anisotropy of the sapphire substrate. Although the fits to the film data were reasonable, the optical anisotropy of the substrate leads to errors in the optical constants extracted from the fits. The uniaxial transmittance model which was used to model the optical anisotropy replicated the broad features of the substrate data.

Although we have presented the results of the far-infrared investigations of just two films; the results are consistent with similar measurements which we performed on other films. A total of three films on MgO and 5 films on sapphire were measured. The generic features of the optical characteristics of all the films investigated were similar to the ones presented here.

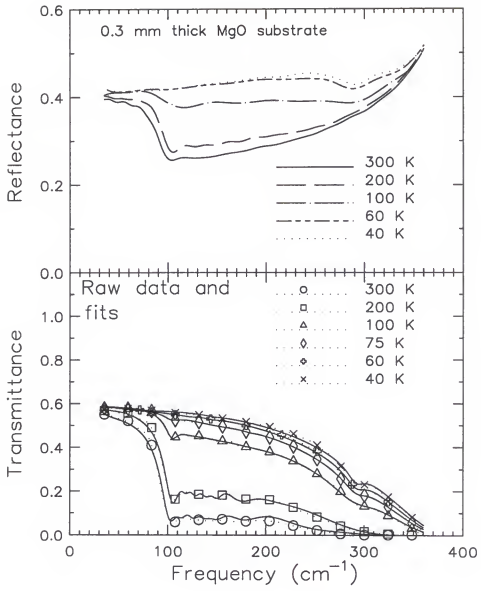

Figure 6–1: The smoothed reflectances and transmittances of MgO. Upper panel: the measured reflectance of a MgO substrate at several temperatures between 40 and 300 K. Lower panel: the solid curves are the fits to the transmittance using a series of Lorentzian oscillators for the dielectric function, while the spectra in dots and symbols are the smoothed transmittance data.

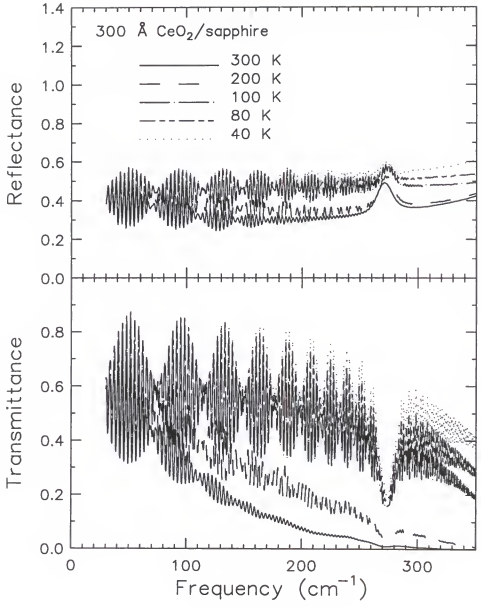

Figure 6–2: The frequency-dependent reflectance and transmittance of cerium oxide on R-cut sapphire (0.5 mm thick) at a few select temperatures.

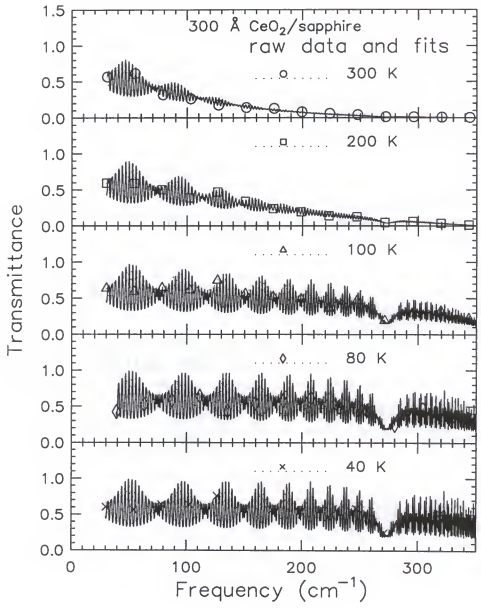

Figure 6–3: The measured transmittance of CeO_2 on sapphire, compared to the fits with a uniaxial transmittance model at several temperatures. The fits are represented by solid lines while the data is in dots and symbols.

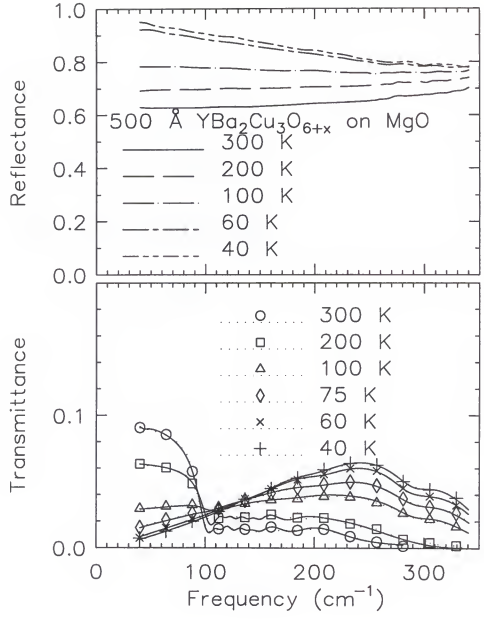

Figure 6–4: Measured reflectance (upper panel) and transmittance in dots and symbols (lower panel) of a 500 Å $YBa_2Cu_3O_{6+x}$ film on a 0.3 mm thick MgO substrate at several temperatures above and below T_c. The solid curves in the lower panel are fits to the measured transmittance using a two-component model.

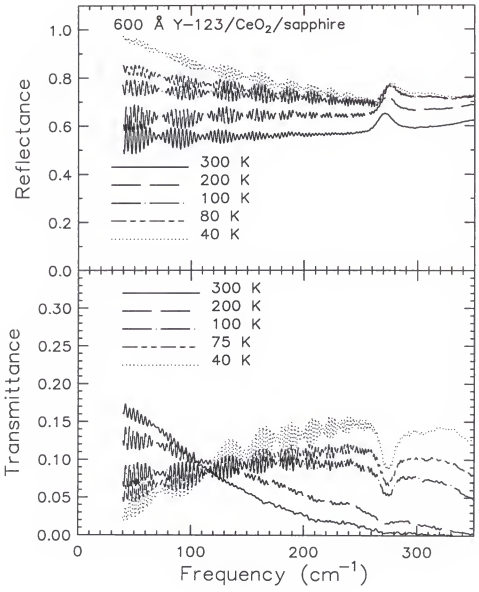

Figure 6–5: The frequency dependent reflectance and transmittance of a 600 Å $YBa_2Cu_3O_{6+x}$ film on a sapphire substrate at a few select temperatures above and below T_c.

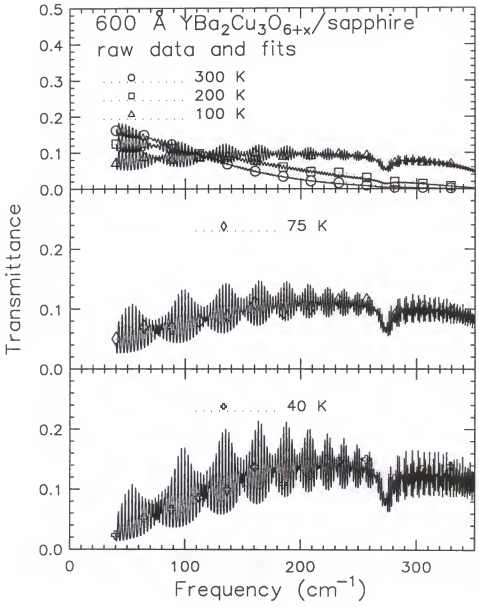

Figure 6–6: Raw transmittance data (dots and symbols), and the corresponding fits (solid lines) at several temperatures above and below T_c for a thin $YBa_2Cu_3O_{6+x}$ film on a sapphire substrate. A uniaxial transmittance model was used to fit the substrate data, and a two-component model was used for the film data.

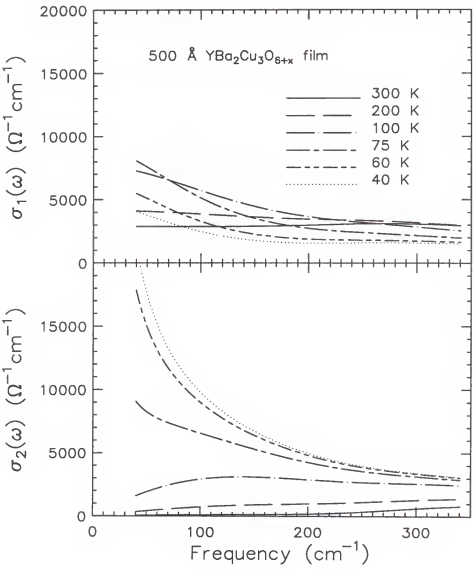

Figure 6–7: The real part (upper panel) and the imaginary part (lower panel) of the complex conductivity of the $YBa_2Cu_3O_{6+x}$ film on MgO at several temperatures. The conductivities were extracted from the fits to the transmittance data.

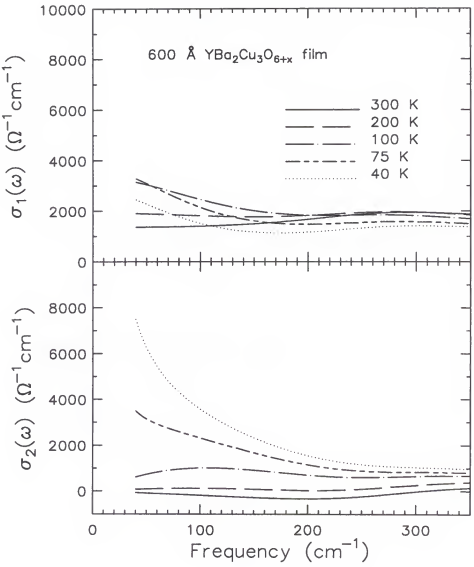

Figure 6–8: The real part (upper panel) and imaginary part (lower panel) of the complex conductivity of the $YBa_2Cu_3O_{6+x}$ film on sapphire at several temperatures. The conductivities were extracted from the fits to the transmittance data.

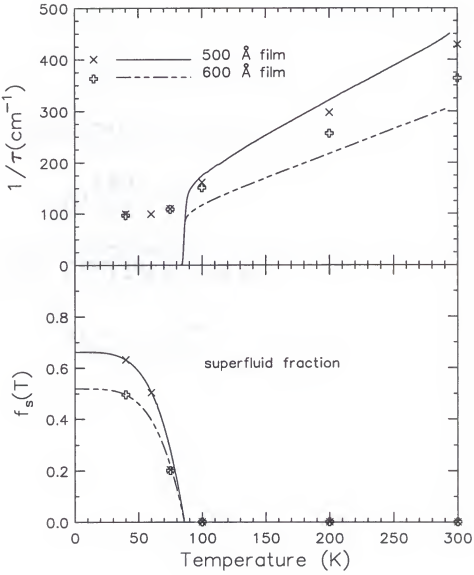

Figure 6–9: The temperature dependent scattering rate and superfluid fraction of the two films discussed in this work. Upper panel: the temperature dependent Drude scattering rate, $1/\tau$, extracted from the fits to the transmittance (in symbols) and estimated from the dc resistivity (solid and dashed lines). Lower panel: the superfluid fraction $f_s(T) = n_s(T)/n$ as a function of temperature. The solid and dashed curves are the best fits to the empirical two-fluid expression $f_s(T) = f_s(0)(1 - (T/T_c)^4)$, where $f_s(0) = 0.66$ (500 Å film) and 0.52 (600 Å film). The symbols are the $f_s(T)$ extracted from the two fluid fits to the transmittance data.

Table 6–1: Parameters giving the best fit to the transmittance of MgO at 40, 75, 100, 200 and 300 K. The last oscillator with plasma frequency ω_{pTO}, center frequency ω_{TO}, and damping constant γ_{TO} is a single TO phonon mode in MgO. The remaining parameters are used to simulate the phonon difference band processes below 400 cm^{-1}.

	300 K	200 K	100 K	75 K	60 K	40 K
$\omega_{p1}(cm^{-1})$	6.4000	3.6510	3.6510	3.7415	5.0472	7.2062
$\omega_1(cm^{-1})$	43.4450	39.4450	39.4450	104.2421	104.2421	66.9503
$\gamma_1(cm^{-1})$	50.0000	28.0000	28.0000	19.3637	69.0000	86.9352
$\omega_{p2}(cm^{-1})$	20.2676	17.0927	6.5638	8.0721	1.5908	1.7637
$\omega_2(cm^{-1})$	102.8884	105.1004	104.2421	146.5179	146.5179	146.5179
$\gamma_2(cm^{-1})$	14.4145	15.6302	15.7608	18.8501	16.4382	23.6710
$\omega_{p3}(cm^{-1})$	14.8581	8.9464	10.5360	7.9131	1.5209	0.3057
$\omega_3(cm^{-1})$	114.4269	118.5110	146.5179	121.8676	121.8676	121.8676
$\gamma_3(cm^{-1})$	14.5488	12.3915	65.6370	526.3826	17.86472	2.2729
$\omega_{p4}(cm^{-1})$	14.7325	10.2064	6.9068	1.3840	0.0024	0.0016
$\omega_4(cm^{-1})$	126.2698	128.2030	121.8676	183.9975	183.9975	183.9975
$\gamma_4(cm^{-1})$	14.6504	13.4457	36.3383	13.6810	118.8062	171.0809
$\omega_{p5}(cm^{-1})$	14.3312	10.2513	10.7502	0.0021	0.0017	0.0022
$\omega_5(cm^{-1})$	137.8251	139.0850	183.9975	243.1730	243.1730	243.1730
$\gamma_5(cm^{-1})$	16.8833	14.7339	82.4147	162.7641	144.6945	194.1924
$\omega_{p6}(cm^{-1})$	17.4937	10.3808	14.6358	12.4206	11.1924	9.6699
$\omega_6(cm^{-1})$	149.9949	150.1191	243.1730	292.1794	292.1794	292.1794
$\gamma_6(cm^{-1})$	21.1419	15.2990	155.0362	28.9699	23.8954	19.9415
$\omega_{p7}(cm^{-1})$	29.8535	20.0011	19.5771	—	—	—
$\omega_7(cm^{-1})$	177.3559	173.9728	292.1794	—	—	—
$\gamma_7(cm^{-1})$	45.1724	38.4291	50.6296	—	—	—
$\omega_{p8}(cm^{-1})$	48.6799	19.2685	—	—	—	—
$\omega_8(cm^{-1})$	256.7527	212.5819	—	—	—	—
$\gamma_8(cm^{-1})$	98.4499	71.1310	—	—	—	—
$\omega_{pTO}(cm^{-1})$	995.0596	1006.7790	1016.8710	1067.0120	1057.5600	1022.4100
$\omega_{TO}(cm^{-1})$	409.0000	423.0998	425.4178	425.3572	419.1264	419.1264
$\gamma_{TO}(cm^{-1})$	5.7792	6.2541	1.6389	1.2655	0.9469	0.8781

$\epsilon_\infty = 3.01$, thickness $d = 0.3\ mm$

Table 6–2: Classical oscillator parameters for cerium oxide between 300 and 40 K.

	300 K	200 K	100 K	80 K	40 K
$\omega_{pTO}(cm^{-1})$	1200	1080	1100	1100	1020
$\omega_{TO}(cm^{-1})$	272	273	273	273	273
$\gamma_{TO}(cm^{-1})$	14	10	10	10	9

$\epsilon_\infty = 5.31$, thickness $d = 300$ Å

Table 6–3: Classical oscillator parameters for sapphire o-ray fits at all temperatures. The extra mode corresponds to a mode introduced at 209 cm^{-1} to account for the extra absorption at higher temperatures.

mode type		300 K	200 K	100 K	80 K	40 K
extra mode	$\omega_{p1}(cm^{-1})$	56.0000	30.500	20.0000	1	—
	$\omega_1(cm^{-1})$	209	209	209	209	—
	$\gamma_1(cm^{-1})$	300	300	300	300	—
phonon	$\omega_{p2}(cm^{-1})$	220.7640	218.9280	216.9101	216.9101	216.9101
	$\omega_2(cm^{-1})$	384.3000	385.0949	385.8426	385.8426	385.8426
	$\gamma_2(cm^{-1})$	4.1000	1.5000	0.3000	0.1000	0.0300
phonon	$\omega_{p3}(cm^{-1})$	732.8450	729.5039	725.6770	725.6770	725.6770
	$\omega_3(cm^{-1})$	438.9000	439.4219	439.8057	439.8057	439.8057
	$\gamma_3(cm^{-1})$	2.6330	1.3000	0.3000	0.1000	0.0300
phonon	$\omega_{p4}(cm^{-1})$	980.8650	978.6532	975.8593	975.8593	975.8593
	$\omega_4(cm^{-1})$	568.2000	568.7346	569.0360	569.0360	569.0360
	$\gamma_4(cm^{-1})$	6.8180	3.5000	0.3000	0.1000	0.0500
phonon	$\omega_{p5}(cm^{-1})$	241.2680	220.9885	197.1609	197.1609	197.1609
	$\omega_5(cm^{-1})$	633.6000	634.6421	635.5070	635.5070	635.5070
	$\gamma_5(cm^{-1})$	6.3360	4.0000	0.3000	0.1000	0.0500
electronic	$\omega_{p6}(cm^{-1})$	69149	67546	70078	70078	70078
	$\omega_6(cm^{-1})$	85723	86559	87439	87439	87439
	$\gamma_6(cm^{-1})$	0.8570	0.8656	0.8656	0.8656	0.8656
electronic	$\omega_{p7}(cm^{-1})$	164651	164651	164651	164651	164651
	$\omega_7(cm^{-1})$	137621	137621	137621	137621	137621
	$\gamma_7(cm^{-1})$	1.3760	1.3762	1.3762	1.3762	1.3762
	ϵ_∞	1.2000	1.3000	1.3000	1.3000	1.3000

thickness $d = 0.5$ mm

Table 6–4: Classical oscillator parameters for sapphire e-ray fits at all temperatures

mode type		300 K	200 K	100 K	80 K	40 K
phonon	$\omega_{p1}(cm^{-1})$	1040.6190	1036.4720	1031.8750	1031.8750	1031.8750
	$\omega_1(cm^{-1})$	399.5000	401.7800	404.1800	404.1800	404.1800
	$\gamma_1(cm^{-1})$	7.9900	6.0000	0.300	0.1000	0.0500
phonon	$\omega_{p2}(cm^{-1})$	729.4160	734.3642	739.5846	739.5846	739.5846
	$\omega_2(cm^{-1})$	584.0000	586.3750	588.8750	588.8750	588.8750
	$\gamma_2(cm^{-1})$	20.4400	17.0000	0.3000	0.2000	0.0500
electronic	$\omega_{p3}(cm^{-1})$	61000	61373	61765	61765	61765
	$\omega_3(cm^{-1})$	82201	83037	83917	83917	83917
	$\gamma_3(cm^{-1})$	0.8220	0.8304	0.8392	0.8392	0.8392
electronic	$\omega_{p4}(cm^{-1})$	165673	165673	165573	165673	165673
	$\omega_4(cm^{-1})$	135082	135082	135082	135082	135082
	$\gamma_4(cm^{-1})$	1.3510	1.3508	1.3508	1.3508	1.3508

$\epsilon_\infty = 1$, thickness $d = 0.5$ mm

Table 6–5: Parameters used in the two-component fits to the transmittance of the film on MgO at three temperatures in the normal state.

mode		300 K	200 K	100 K
Drude	$\omega_{pD}(\mathrm{cm}^{-1})$	8626.7960	8613.1590	8614.8920
	$1/\tau(\mathrm{cm}^{-1})$	428.7089	296.9635	160.8391
mid-ir	$\omega_{p1}(\mathrm{cm}^{-1})$	3000	3000	3000
	$\omega_1(\mathrm{cm}^{-1})$	290	290	290
	$\gamma_1(\mathrm{cm}^{-1})$	250.7474	250.0612	255.9913
mid-ir	$\omega_{p2}(\mathrm{cm}^{-1})$	9800	9800	9800
	$\omega_2(\mathrm{cm}^{-1})$	740	740	740
	$\gamma_2(\mathrm{cm}^{-1})$	1550	1550	1550
chain state	$\omega_{p3}(\mathrm{cm}^{-1})$	14500	14500	14500
	$\omega_3(\mathrm{cm}^{-1})$	3300	3300	3300
	$\gamma_3(\mathrm{cm}^{-1})$	7500	7500	7500

$\epsilon_\infty = 25$

Table 6–6: The parameters used in the fits to the transmittance of the film on MgO at 3 temperatures in the superconducting state. The higher midinfrared oscillator and the chain state from table 6–5 have not been repeated here for the sake of brevity.

mode		75 K	60 K	40 K
	$\omega_{pD}(\mathrm{cm}^{-1})$	8666.3366	8700.3219	8697.9634
	f_s	0.2027	0.5029	0.6313
	$1/\tau(\mathrm{cm}^{-1})$	109.4391	98.9587	99.1675
mid-ir	$\omega_{p1}(\mathrm{cm}^{-1})$	3000	3000	3000
	$\omega_1(\mathrm{cm}^{-1})$	290	290	290
	$\gamma_1(\mathrm{cm}^{-1})$	267.8137	256.9662	256.9662

$\epsilon_\infty = 25$

Table 6–7: Parameters which were used in the two-component fits to the transmittance of the film on sapphire at three temperatures in the normal state.

mode		300 K	200 K	100 K
Drude	$\omega_{pD}(\mathrm{cm}^{-1})$	5432.5140	5434.6850	5486.0090
	$1/\tau(\mathrm{cm}^{-1})$	363.5505	255.8019	150.2427
mid-ir	$\omega_{p1}(\mathrm{cm}^{-1})$	3000	3000	3000
	$\omega_1(\mathrm{cm}^{-1})$	290	290	290
	$\gamma_1(\mathrm{cm}^{-1})$	250	250	250
mid-ir	$\omega_{p2}(\mathrm{cm}^{-1})$	9800	9800	9800
	$\omega_2(\mathrm{cm}^{-1})$	740	740	740
	$\gamma_2(\mathrm{cm}^{-1})$	1550	1550	1550
chain state	$\omega_{p3}(\mathrm{cm}^{-1})$	14500	14500	14500
	$\omega_3(\mathrm{cm}^{-1})$	3300	3300	3300
	$\gamma_3(\mathrm{cm}^{-1})$	7500	7500	7500

$\epsilon_\infty = 25$

Table 6–8: Parameters used in the two-fluid fits to the transmittance of the film on sapphire at two temperatures in the superconducting state. The two midinfrared oscillators and the chain state oscillator which was used in these fits are the same as those in table 6–7.

	75 K	40 K
$\omega_{pd}(\mathrm{cm}^{-1})$	5486.0085	5701.8970
f_s	0.2000	0.4948
$1/\tau(\mathrm{cm}^{-1})$	108.4216	96.3746

$\epsilon_\infty = 25$

CHAPTER 7
FAR-INFRARED ELECTRO-OPTIC STUDIES OF $YBa_2Cu_3O_{6+x}$ FILMS

7.1 Introduction

In this chapter we present the results of electro-optic transmittance measurements on two $YBa_2Cu_3O_{6+x}$ thin films in the frequency range from 40–350 cm^{-1}, and at two temperatures, 75 K and 40 K, in the superconducting state. The details of the experiment have been described in chapter 5. We will also present the results of some simple simulations, using a simple two-fluid model, of the changes in transmittance which are to be expected if the main effect of the current is to transfer spectral weight from the condensate to the Drude band. This will be followed by a discussion of the critical state model [89, 90] which is often used to study critical currents in the cuprates. The model in many cases has given fairly good agreement with flux and current density distributions determined by a variety of imaging techniques [91, 92]. This discussion will facilitate, a basic understanding of the data in some cases, particularly for currents much smaller than the critical current.

The effects of large transport currents on the superconducting state of the cuprates have been studied experimentally by dc transport [93–95], angle resolved photoemission spectroscopy (ARPES) [96] and tunnelling [97]. The main motivation for this study is to investigate whether or not the changes in the superconducting state induced by a transport current can be observed in the far infrared, which probes the low frequency electrodynamics of the charge carriers. The results here will be discussed qualitatively. There are two main obstacles to any quantitative analysis of the results: the first difficulty arises from the absence of a complete theory of superconductivity in the cuprates, and the second is related to ambiguities in assigning the observed changes solely to the effects of the current.

These issues will be discussed in later sections where we will address the problems associated with the inherent inhomogeneity of the current density distribution in the superconducting state and the possible spurious effects of contact heating on the observed changes in the transmittance.

7.2 Results and Discussion

7.2.1 Electro-optic Transmittance of Film on MgO

The results of our electrooptic transmittance measurements on a $YBa_2Cu_3O_{6+x}$ film on MgO at 75 K is shown in fig. 7–1. The contact arrangement which was used for the transport measurements is shown in fig. 5–3 (b) of chapter 5. The fringes in the measured transmittance in part (A) of the figure are due to the multiple internal reflections in the substrate, which have been smoothed in part (B). At each current we measured the corresponding voltage and the transmittance. The results show that at all currents up to 200 mA there is little or no change in the transmittance. At all current levels the voltage was zero which implies that the film remained superconducting over the entire current range. This insensitivity of the transmittance to the applied current at all current levels up to 200 mA, is further highlighted by the fractional change in the transmittance plotted in part (C) of the figure. The fractional change in transmittance is seen to be zero at all currents. We also attempted to measure the transmittance at 300 mA. At this current level the voltage was zero at the start of the transmittance measurements, then, the film switched to the resistive state after a few seconds and the voltage increased rapidly. The substrate cracked and the film was destroyed. It is well known from previous attempts to measure the effects of large transport currents on the electronic density of states of conventional superconductors by tunnelling [98], that it is possible to have resistive switching of a film carrying a transport current even below the critical current I_c. This is attributed to the superconducting state being metastable while carrying a transport current. If the current flows for

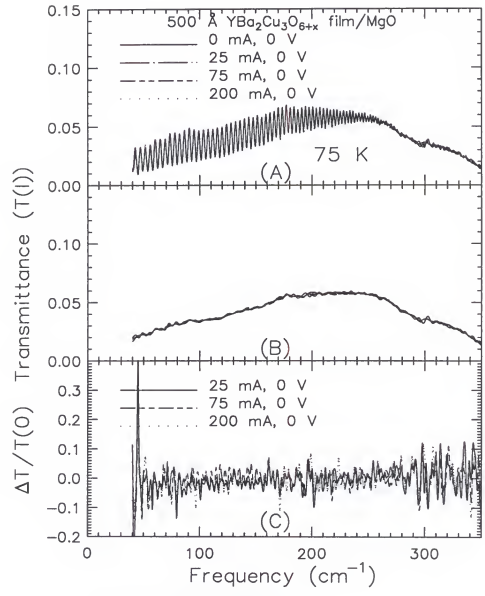

Figure 7–1: The transmittance of a 500 Å $YBa_2Cu_3O_{6+x}$ film as a function of current. (A) The raw transmittance $T(I)$ as a function of current I = 0, 25, 75 and 200 mA. The voltage V is zero at all currents. (B) The smoothed data, with the fringes in (A) at all currents smoothed out. (C) The fractional change $\Delta T/T(0)$ in transmittance with current, expressed as a fraction of the zero-current transmittance $T(0)$, where $\Delta T = T(I) - T(0)$.

a long enough time the film eventually switches to the lossy resistive state even though the current is less than the critical value. This is a possible explanation for the switching observed here at 300 mA. The current density at 300 mA is $J = 5 \times 10^4$ Acm^{-2}, if we assume a uniform current density distribution. The second possibility is related to ohmic losses in the contacts with the film. We estimate the contact resistance of each current contact to be about 0.1 Ω. Although we did not perform a detailed measurement of the contact resistance we simply used a multimeter to measure the resistance across the current leads while the film is in the superconducting state. This gives the resistance of the lead wires and the current contacts. We estimated the lead wire resistance by shorting the leads and measuring their resistance. The lead resistance was then subtracted and the resulting resistance was taken to be the resistance of the current contacts. For a current of 300 mA flowing through a 0.2 Ω resistor the dissipated power is 18 mW. This power is large enough to produce significant heating over the duration of a typical transmittance measurement which is anywhere between 5 to 10 minutes. It is impossible at this point to distinguish which process is responsible for the switching, nonetheless, it appears that the temperature gradient between the surface of the film and the backside of the MgO substrate caused the substrate to crack.

7.2.2 Electro-optic Transmittance of Film on Sapphire

The upper and lower panels of fig. 7–2 show the results of our electrooptic transmittance measurements on the film on sapphire at 75 K. The contact arrangement used for the transport measurements is shown in fig. 5–3(c) in chapter 5. The spectra show that there is little or no change in the measured transmittance up to 10 mA. The measured voltage at 10 mA is zero, which means that the film is still superconducting at this current level. This insensitivity of the measured transmittance to current at 10 mA is most easily seen in the plot of the fractional change

in the lower panel. The fractional change in transmittance is zero over the entire frequency range at this current. The transmittance in the absence of the current is nearly indistinguishable from the 10 mA spectrum. There are tiny differences which are within the experimental uncertainty of the measurement. A very different effect is observed, however, when the current is increased to 15 mA. The measured voltage at this current level was 323.16 mV which means that the sample is in the resistive state. The critical current therefore lies somewhere between 10 and 15 mA. This implies that the critical current density for this film is in the range 3.3×10^3 and 5×10^3 Acm^{-2}. It is interesting to compare this current density with the critical current densities in refs. [94] and [95]. The critical current densities in the latter reference were between 2×10^3 and 2.3×10^6 Acm^{-2} at 77 K. The transition temperatures of all their $YBa_2Cu_3O_{6+x}$ films were between 91 and 93 K. They used a 5 $\mu\mathrm{Vcm}^{-1}$ criterion to determine the critical current density. The current densities J^* in ref. [94] at which there were full transitions to the normal state were always between 10^5 and 10^6 Acm-2. The critical current density corresponding to the transition to the resistive state at 15 mA in this film is about 2 or 3 orders of magnitude lower that the corresponding critical currents in ref. [94]. One possible reason for the discrepancy may be that the film in this experiment was at a temperature much closer to T_c than the measured temperature of 75 K. There are two notable features of the transmittance observed at 15 mA. The first is an increase in the low frequency transmittance below 100 cm^{-1} when compared to the transmittance without current. The second is a depression of the transmittance above 100 cm^{-1} below the zero-current spectrum. The fractional change at this current shows that the low frequency transmittance is enhanced by about 15% at 40 cm^{-1} and is depressed by a similar percentage at 350 cm^{-1}. It is interesting to compare the resistivity calculated from the fits to the film transmittance in chapter 6 at 75 k, to that calculated from the transport measurements here at 15 mA. The

resistivity is calculated from the equation

$$\rho_{dc} = \frac{RA}{l}, \tag{7.1}$$

where $R = V/I$ where V is the measured voltage and I is the current, A is the cross sectional area of the film, and l is the center-to-center distance between the voltage electrodes. The corresponding dc resistivity at 75 K can be calculated from the fits to the film transmittance, if we assume that all the superfluid is completely converted to normal fluid by the current without changing the scattering rate. The relevant equation is:

$$\rho_{fit} = \frac{4\pi(1/\tau)}{\omega_{pD}^2}, \tag{7.2}$$

where $1/\tau$ is the scattering rate and ω_{pD} is the Drude plasma frequency. The calculations give, $\rho_{dc} = 215.44\ \mu\Omega$ cm and $\rho_{fit} = 216.15\ \mu\Omega$ cm. The agreement here is quite good in spite of the the errors inherent in parameters used to fit the film data at 75 K. If this truly represents the normal state, we expect that the resistivity, and hence the fractional change in transmittance at currents larger than 15 mA should saturate (i.e. the resistivity and fractional change should remain constant at the 15 mA values at higher currents). The transmittance at 20 mA exceeds that at 15 mA at low frequency and falls below it at higher frequency. The fractional change at 20 mA in the figure approaches 25% at 40 cm^{-1}. This exceeds the fractional change observed at 15 mA, which means that the fractional change does not saturate at the 15 mA value. The calculated resistivity at 20 mA is $\rho_{dc}(20\text{ mA}) = 237.33\ \mu\Omega$ cm. This resistivity falls on the linear portion of the temperature dependent resistivity plotted in the lower panel of fig. 5–1 in chapter 5. These observations are a signature of heating as neither the resistivity nor the fractional change in transmittance saturate at their 15 mA values. It is well known that currents and increased temperature act as pair breakers and weaken superconductivity. The effects here may be a combination of both. At this point it

is impossible to know how much of the observed changes are due to either process as both produce similar effects.

The 40 K electro-optic spectra shown in fig. 7–3 show quite different results. The transmittance was measured at three currents: 50, 80 and 100 mA. The voltage reading in each case was zero which means that the film remained superconducting up to 100 mA. We also attempted to measure the electrooptic transmittance at 150 mA but during the experiment the voltage suddenly increased from zero, and continued to increase up to a few volts. This was a sign of heating and the transmittance at low frequency below 100 cm^{-1} approached the normal state transmittance at room temperature. This implies that the critical current density, J_c of this film at 40 K exceeds 5×10^4 Acm^{-2}. The critical current densities of the $YBa_2Cu_3O_{6+x}$ films in ref. [95] exceed 10^7 Acm^{-2} at 60 K and is of the same order of magniture at 4.2 K. It is absolutely hopeless to achieve such current densities at 40 K in this experiment without significant heating. The critical current I_c would be of the order of a few Amperes. We have not included the spectrum at 150 mA here as it adds nothing to the current discussion. It can be seen in the lower panel of the figure that the fractional change in the transmittance at 50 mA increases just above 4% below 50 cm^{-1}, and decreases at 350 cm^{-1} by about 3%. At 80 mA the reduction of the fractional transmittance above 300 cm^{-1} is stronger, approaching 11%. The lower frequency fractional transmittance change approaches 15% at this current at 40 cm^{-1}. The 100 mA transmittance clearly shows an enhancement below 100 cm^{-1} along with a further suppression of the high frequency transmittance. It is not at all obvious if the changes here are associated with the current or heating due to losses in the contacts. It is possible that the losses in the contacts caused a temperature rise in the film, and that after a time the film came to a steady-state temperature above 40 K in the superconducting state. This would be consistent with what is observed in the electooptic transmittance measurements

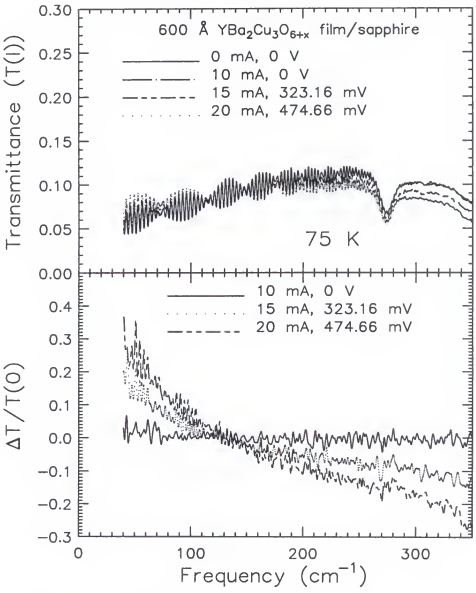

Figure 7–2: The electro-optic transmittance of a thin $YBa_2Cu_3O_{6+x}$ film on sapphire at 75 K. Upper panel: The measured transmittance $T(I)$ at currents $I = 0$, 10, 15 and 20 mA. The measured voltages V are also shown at each current. Lower panel: the fractional change in transmittance $\Delta T/T(0)$ at each current expressed as a fraction of the zero current spectrum $T(0)$, where $\Delta T = T(I) - T(0)$.

along with the absence of a voltage at any of the measured currents. In the next section we shall consider some simple simulations of the expected changes in the transmittance using a simple two-fluid model of the superconducting state with a superfluid fraction which varies with the current.

7.2.3 Two-Fluid Simulations

Currents and magnetic fields modify the superconducting state of the cuprates by breaking apart the Cooper pairs. This leads to a weakening of superconductivity. This concept has been quantified by Usadel, using a single parameter, the depairing energy Γ, in the diffusive limit in conventional BCS superconductors [99]. The Usadel equations extended the equivalence of the effect of fields and currents on the superconducting state to inhomogeneous cases where the modulus of the order parameter varies in space. The Usadel equations have been used to analyze the effects of supercurrent on the density of states of a superconductor studied by electron tunnelling [98]. Despite this, to the current authors knowledge there is no corresponding theory for the effects of a supercurrent on clean limit d-wave superconductors such as the cuprates.

We consider here a simple model where the only effect of a supercurrent is to reduce the superfluid fraction in the two-fluid fits to the transmittance in chapter 6. Let us consider a simple two fluid dielectric function of the form:

$$\epsilon(\omega) = (1 - f_s(I))\epsilon_D(\omega) + f_s(I)\epsilon_S(\omega) + \epsilon_\infty \qquad (T < T_c), \tag{7.3}$$

where all the quantities here are the same as those defined in eqns. (6.4) and (6.5) in chapter 6, but with a superfluid fraction $f_s(I)$ which is a monotonic decreasing function of the supercurrent I. In this simple model the only effect of the supercurrent is to transfer spectral weight from the condensate to the Drude band without affecting the Drude scattering rate. The f sum rule is automatically satisfied by this form of the dielectric function. Although this simple model does

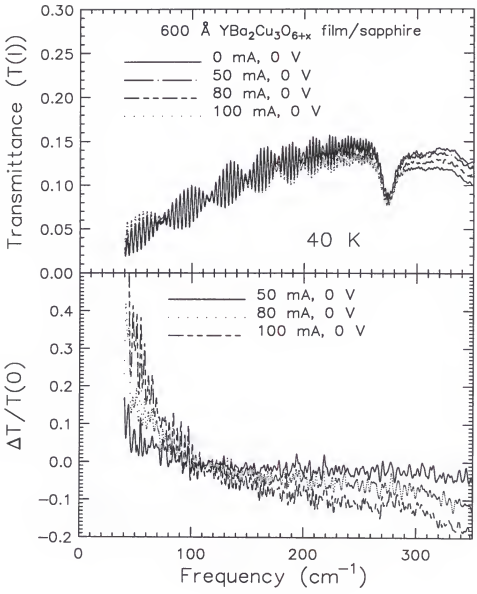

Figure 7–3: The electro-optic transmittance of a thin $YBa_2Cu_3O_{6+x}$ film on sapphire at 40 K. Upper panel: The measured transmittance $T(I)$ at currents $I = 0$, 50, 80, and 100 mA. The measured voltages V shown, are zero at all currents. Lower panel: the fractional change in transmittance $\Delta T/T(0)$ at each current expressed as a fraction of the zero current spectrum $T(0)$, where $\Delta T = T(I) - T(0)$.

not give a functional form of the superfluid function $f_s(I)$ it allows us to calculate the transmittance of the film on its substrate for various values of $f_s(I)$. For the sake of notational simplicity we will denote the zero current superfluid fraction $f_s(0) = f_{so}$. In the two-fluid fits to the film on MgO, and sapphire $f_{so}(75K) \approx 0.2$ at 75 K. The superfluid fraction at 40 K for the film on sapphire $f_{so}(40K) \approx 0.5$.

Simulations for film on MgO. The top panel of fig. 7–4 shows the plots of the simulated transmittance of the 500 Å film on MgO at 75 K, calculated for various values of the superfluid fraction $f_s(I)$. The parameters used for the zero current spectrum are the same as those which were used in the two-fluid fits in chapter 6. The superfluid fraction is decreased by 25%, 50%, 75% and then 100% from the zero current value f_{so} and the transmittance is calculated for each case. Within this simple model, the transmittance at low frequency below 100 cm^{-1} increases, while the transmittance at higher frequencies decreases below the zero-current spectrum as the superfluid fraction decreases. The changes are most easily seen in the lower panel of fig. 7–4 where the corresponding plots of the fractional changes in transmittance are shown. In all cases the fractional change in transmittance at low and high frequencies is always less than less than 12%. The $f_s(I) = 0$ curve would correspond to the spectrum at or above the critical current I_c when superconductivity is completely destroyed. Above this current density, when all the spectral weight of the condensate has been completely depleted, it is not expected that the current will further change the transmittance.

Simulations for film on sapphire. The simulated changes in the transmittance for a film on sapphire at 75 and 40 K are shown in figs. 7–5 and 7–6 respectively. Although the upper panels of both figures do not show the changes very clearly, the lower panels show the plots of the fractional changes, where the fringes have been smoothed. There are a number of features which are common to the simulations at both temperatures. The first apparent observation is an increase in the fractional

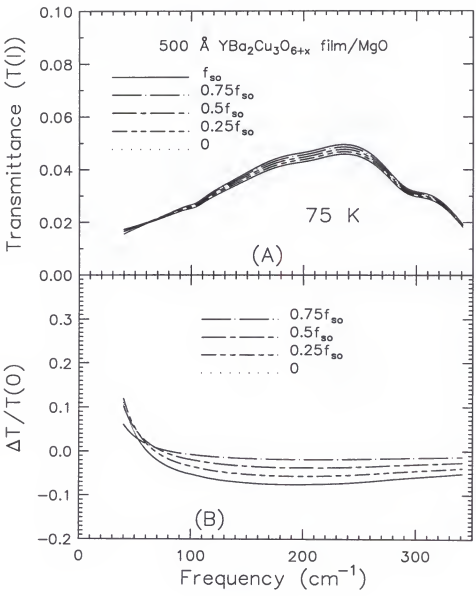

Figure 7–4: Simulations of the changes in the transmittance of a film on MgO at 75 K with decreasing superfluid fraction $f_s(I)$. The calculations were done using the two-fluid model, and assuming that the only effect of the current is to transfer spectral weight from the condensate to the Drude band. (A) The calculated transmittance at several values of the superfluid fraction $f_s(I)$. (B) The fractional change in transmittance calculated from the simulations in part (A), expressed as a fraction of the zero-current transmittance.

change in transmittance at very low frequency—below 50 cm^{-1} at 75 K and below 60 cm^{-1} at 40 K. The fractional increase at 75 K at the lowest frequency 40 cm^{-1} never exceeds 5%. This is in stark contrast to the much stronger enhancement of the transmittance at 40 K which approaches 50% at 40 cm^{-1} for the $f_{so} = 0$ curve. The second feature of the simulations is the reduction of the transmittance at frequencies above 60 cm^{-1} with decreasing superfluid fraction. The suppression of the transmittance at 40 K is much stronger than the corresponding effect at 75 K for similar fractional changes in the superfluid fraction.

A comparison of the experimental electro-optic transmittance spectra at 75 K in fig. 7–2 with the simulations in fig. 7–5 highlight interesting differences. The greatest disparities occur at the two extremes of the spectral range at 40 and 350 cm^{-1}. The enhancement of the low frequency transmittance in the simulations are of the order of 3 to 5% as compared to the electro-optic data where the enhancement is between 15 and 25%. The suppression of the transmittance at 350 cm^{-1} never exceeds 4% in the simulations, but approaches 30% at the highest current (20 mA) in the actual electro-optic data. If the simulations are correct it means that these discrepancies may be related to the effect of heating on the measured spectra, which causes the substrate transmittance to increase at low frequencies and decrease at higher frequencies.

There is much closer agreement between the fractional changes in the transmittance of the measured electro-optic data at 40 K in fig. 7–3 and the simulations in fig. 7–6. The fractional change in transmittance at 100 mA approaches 40% at 40 cm^{-1}, this is very close to the simulated fractional change at $0.5f_{so}$. The reduction of the transmittance at 350 cm^{-1} is about 18% for the 100 mA spectrum but only about 5% for the $0.5f_{so}$ simulation. One has to be wary of trying to make any numerical comparison between the data and the simulations. The parameters which were used to fit the substrate and film are uncertain and may lead to errors in the

simulated changes. The 80 mA fractional change in electro-optic transmittance approaches 17% at 40 cm^{-1}, and the $0.75f_{so}$ simulated change is about 20%. There is also disagreement between the latter two spectra at 350 cm^{-1}. These differences may also be a result of contact heating. We cannot unambiguously assign the changes observed solely to the effect of the current. In the next section we will discuss critical-state theory which has often been used to predict current density distributions in thin superconducting films. It will highlight some of the difficulties in quantifying these electro-optic results.

7.2.4 Current Density Distributions in Superconducting Thin Films

The most notable feature of any superconductor is its ability to carry an electric current where the losses are reduced to an unmeasurably small level. This persists up to some maximum loss-free current density J_c, beyond which the usual losses set in. The loss-free current only flows in a small surface layer in the superconductor at thermal equilibrium. The phase coherence of the superconducting state effectively screens fields and currents from the interior of the superconductor. This phenomenon of diamagnetism is also responsible for the high reflectivities and low transmittance of superconductors which are observed in the far infrared.

The superconductor establishes a Meissner state when either a small external magnetic field or a transport current is applied. In this state the external fields and currents are completely screened from the bulk of the superconductor. The screening occurs because the superconductor sets up Meissner supercurrents of density J_M which flow in a surface layer of thickness of the order λ, the London penetration depth. The maximum Meissner current density is the depairing current density

$$J_0 = \frac{1}{12\sqrt{3}} \frac{c\phi_0}{\pi^2 \xi \lambda^2}, \tag{7.4}$$

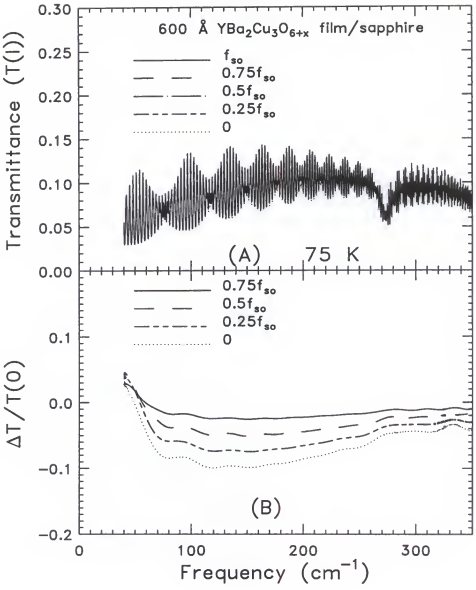

Figure 7–5: Simulations of the changes in the transmittance of a film on sapphire at 75 K with decreasing superfluid fraction $f_s(I)$. (A) The calculated transmittance at several values of the superfluid fraction $f_s(I)$. (B) The fractional change in transmittance calculated from the simulations in part (A), expressed as a fraction of the zero-current transmittance. The fringes have been smoothed to make the changes clearer.

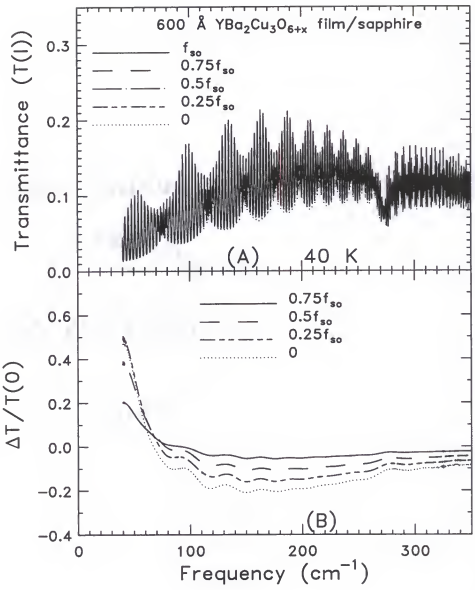

Figure 7–6: Simulations of the changes in the transmittance of a film on sapphire at 40 K with decreasing superfluid fraction $f_s(I)$. (A) The calculated transmittance at several values of the superfluid fraction $f_s(I)$. (B) The fractional change in transmittance calculated from the simulations in part (A), expressed as a fraction of the zero-current transmittance. The fringes have been smoothed to make the changes clearer.

where the kinetic energy of the supercurrents balances the condensation energy of the superconducting state. Here $\phi_0 = h/2e$ is the flux quantum, λ is the penetration depth and ξ is the Ginzburg-Landau coherence length.

If the magnetic field H at the surface of a type II superconductor exceeds the lower critical field H_{c1} the superconductor lowers its free energy by admitting quantized magnetic flux or vortices. The entry of vortices into a superconductor leads to a mixed state where small quasi-normal regions in the vortex cores and superconducting regions exist in thermal equilibrium. The macroscopic magnetic flux density $\boldsymbol{B}$ averaged over a few intervortex spacings has magnitude $B = n\phi_0$ where n is the local vortex density. The flux lines which enter the superconductor are pinned by inhomogeneities in the material. If the local current density J exceeds the critical current J_c the flux lines depin moving under the action of the Lorentz force $\boldsymbol{F} = \boldsymbol{J} \times \boldsymbol{B}/c$. This flux motion induces an emf and leads to dissipation. If the current is a transport current which is produced by an external source, a stationary dissipative state is formed. This J_c represents the critical current which is usually probed by nonlinear transport measurements which are used to plot the I-V characteristics of the superconducting state. The depairing current density J_0 which is associated with the full transition to the normal state forms an upper bound on the magnitude of the depinning critical current density J_c. It is expected, at least intuitively, that the most drastic changes in the electrooptic transmission should occur at current densities close to J_0.

We now consider the current density distribution predicted by the critical-state model in a simple geometry where exact analytic solutions are available. Fig. 7–7 shows an infinitely long thin film of width $2W$ and thickness d carrying a transport current I_T in the superconducting state. Here I_T flows in the y direction and the current density vector has only one component in the y direction $J_y(x)$. It has been shown that when I_T is very weak it generates a self field that curves around

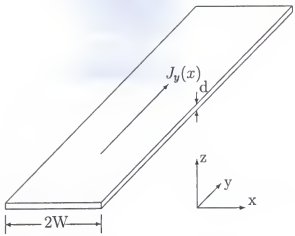

Figure 7–7: Schematic diagram of the thin film geometry considered here. The film has width $2W$ and its thickness d is smaller than the London penetration depth λ. The film is infinite in the Y direction where a transport current $J_y(x)$ flows in the superconducting state.

the sample so that there is a discontinuity in the magnetic induction B_x in the x direction between the top and bottom surfaces. The boundary conditions then mandate that currents flow across the entire width of the film not just near the film surface within a penetration depth λ. The strip is then in the Meissner state, and no magnetic flux has penetrated so that $B_z(x) = 0$ for $-W \leq x \leq W$. The analytic solutions for the macroscopic current density and magnetic induction $B_z(x)$ has been obtained by conformal mapping techniques and are given by:

$$J_y(x) = \frac{I_T}{\pi d\sqrt{W^2 - x^2}}, \qquad -W < x < W, \tag{7.5}$$

$$B_z(x) = -\frac{2xI_T}{c|x|\sqrt{x^2 - W^2}}, \qquad |x| > W. \tag{7.6}$$

At higher currents when the B field near the edges of the film exceeds the lower critical field H_{c1} vortices begin to penetrate. The depth of penetration depends on the critical current density J_c which is assumed to be independent of B. The

solutions for the critical state which is established after the flux penetration is:

$$J_y(x) = \begin{cases} \frac{2J_c}{\pi} \arctan\left(\sqrt{\frac{W^2-a^2}{a^2-x^2}}\right), & -a < x < a, \\ J_c, & a \leq |x| < W, \end{cases} \tag{7.7}$$

and the width of the field free region $2a$ is given by

$$a = W\sqrt{1-(I_T/I_c)^2} \tag{7.8}$$

where $I_c = 2dWJ_c$ is the strips critical current. The flux density distribution becomes:

$$B_z(x) = \begin{cases} 0, & -a \leq x \leq a, \\ \pm B_f \ln \frac{\sqrt{W^2-x^2}}{\sqrt{W^2-a^2}-\sqrt{x^2-a^2}}, & a < |x| < W, \\ \pm B_f \ln \frac{\sqrt{x^2-W^2}}{\sqrt{x^2-a^2}-\sqrt{W^2-a^2}}, & |x| > W, \end{cases} \tag{7.9}$$

where $B_f = \frac{4}{c} dJ_c$. The strip is therefore composed of two regions: a vortex free central region of width $2a$ and a flux penetrated region on either side of the flux free region of width $W - a$. It follows that as the current increases up to I_c the width of the field-free central region diminishes. The current density in the flux penetrated regions is J_c but $J_y(x) < J_c$ in the central region. As the transport current is increased beyond I_c the vortices begin to move and dissipation sets in.

It is not very obvious at this point how this inhomogeneous current and flux density distribution affects the infrared electrooptic transmittance. It is not believed that the self field of the current which produces vortices in the flux penetrated regions will produce noticeable changes in the measured electrooptic spectra. The main reason for this is that the magnetic field in the flux-penetrated region is of the order of a few Gauss which is quite small. In most previous studies of the effect of magnetic fields on the infrared spectra of the cuprates [100–104], changes in the spectra are observed only at very high fields of a few Tesla.

7.3 Summary

The results of our electro-optic transmittance measurements on a $YBa_2Cu_3O_{6+x}$ film on MgO at 75 K and on a similar film on sapphire at 75 and 40 K show differing results. The film on MgO showed no electro-optic effect up to a current level of 200 mA. This was expected from the fact that the measured voltage remained zero at all currents up to this value which meant that the current had little effect on the superconducting state. At 300 mA the film displayed switching but the underlying MgO substrate cracked. The cracking may be related to heating within the film and contacts which created a thermal strain on the substrate. The fairly high normal-state resistivity of the cuprates means that heating will always be a problem when the system switches to the resistive state.

In contrast, the film on sapphire showed an electro-optic effect at 15 mA and at 75 K. The measured voltage at this current was nonzero which means the film was no longer superconducting. We believe that this change in the transmittance observed at 15 mA is spurious and may be caused by heating. At 20 mA the fractional changes in the transmittance did not saturate and the voltage increase exceeded that which would be expected for the normal state resistivity at that temperature. This gave further evidence that the results are due to heating and not the pair breaking effect of the current. The 40 K electrooptic transmittance spectra showed changes at currents where the measured voltage was zero. These may be true changes associated with the current, but they may also be an artifact of the losses in the surface contacts. The larger currents which were passed at 40 K as compared to those at 75 K made such losses more likely even for contacts of resistance of the order of 1 Ω. The ensuing temperature rise could possibly lead to an effect similar to that of the current.

The simulations using two-fluid fits to the film on MgO from chapter 6 as starting parameters, with a current dependent superfluid fraction gave valuable

insights. The main result is that a decreasing superfluid fraction would lead to an increase in the low frequency transmittance below 50 cm^{-1} and a depression of the transmittance at higher frequencies up to 350 cm^{-1}. Because we were unable to observe an electro-optic effect in this film we were unable to make a comparison of the measured data with the simulations.

We compared the model simulations for the transmittance of the film on sapphire at 75 and 40 K with the electro-optic data at the same temperatures. There were stark differences between the simulations and data at 75 K. The fractional changes in the actual data far exceeded the fractional changes in the simulations at 75 K. This may be a sign of heating in the films. The simulations and electro-optic data agree much better at 40 K. The fractional changes at 40 cm^{-1} and at 80 and 100 mA, differ from the simulations at $0.75 f_{so}$ and $0.5 f_{so}$ by just a few percent. The difference between fractional changes between these spectra at 350 cm^{-1} are much larger. This may be an artifact due to heating in the contacts or due to errors in the parameters used to fit the film and substrate in this spectral region.

A consideration of the the current density distribution in a thin superconducting strip using the critical-state model shows that the current density distribution is inhomogeneous at sub-critical currents. This inhomogeneity results from the diamagnetic nature of the superconducting state which tends to screen fields and currents. This means that any quantitative analysis of electro-optic transmittance data at sub-critical currents will be quite complicated. The mixed state which is formed at $I > I_c$ will lead to small losses. In this simple experiment we cannot account for these losses which heat the film and substrate. The very long measurement times required for spectroscopic investigations means that even a small amount of dissipation leads to a pileup of heat after long times. This heating will invariably affect the electro-optic data.

CHAPTER 8
CONCLUSION

We have studied the the effect of a transport current on the superconducting state optical transmittance of two thin $YBa_2Cu_3O_{6+x}$ films over a frequency range from 40–350 cm^{-1} in the far infrared. The films were first characterized by fitting the the measured transmittance at several temperatures in the normal and superconducting states, with a simple two-component model. The electro-optic transmittance was then examined near T_c at 75 K for both films and in the low temperature regime at 40 K for the film on sapphire.

The results of the two-component fits in the normal state show that the strong temperature dependence of the transmittance of both films is related to the strong temperature dependence of the free carrier Drude conductivity centered at zero frequency. The mid infrared band at higher frequency is fairly inert and insensitive to temperature. There is close agreement between the linear dc resistivity measured by dc transport and the Drude conductivity $\sigma_{1D}(\omega = 0, T)$ extracted from the fits and extrapolated to zero frequency. The fairly narrow Drude peak at $\omega = 0$ has a width of the order k_BT which means the Drude scattering rate $1/\tau$ decreases linearly with decreasing temperature. The Drude plasma frequency ω_{pD} was found to be nearly temperature independent for both films. Within this simple two-component model the strong temperature dependence of the optical properties of the films is assigned to a strong temperature dependence of the free carrier relaxation rate. The origin of the mid infrared absorption is still a subject of intense debate.

The supercondcting state response was analyzed within the framework of a simple two-fluid model. It was found that the superconducting state was

marked by a transfer of spectral weight from the Drude band to the origin, which formed a delta function in the real part of the conductivity. This delta function response of the condensate had a marked effect on the measured transmittance. The slope of the transmittance changed below T_c and approached zero in the dc limit. The strength of the suppression of the low frequency transmittance increased with decreasing temperature down to 40 K. The most striking feature of the superconducting state is the observation of a depression of the quasiparticle scattering rate below the linear normal-state trend. The low temperature fits also demonstrate that a large fraction of the carriers do not condense at 40 K. The two latter observations are generic features of the superconducting state of all cuprates.

The electrooptic transmittance of both films appeared to be complicated by the effects of heating. The film on MgO had a critical current I_c in excess of 0.3 A at 75 K. We did not observe any change in the measured electro-optic transmittance up to 0.2 A. The film and substrate cracked at a current level of 0.3 A, this effect is believed to be a sign of contact heating. The critical current of the film on sapphire was between 10 and 15 mA at 75 K. The electro-optic transmittance showed no change up to 10 mA, but showed slight changes at 15 and 20 mA where the film was in the resistive state. There is ample evidence that heating played a role in these changes. The first observation is the lack of saturation of the changes in the electro-optic transmittance up to 20 mA. The second is related to the large differences in the resistivity calculated from the two-fluid fits and from the transport data at 15 and 20 mA. Then too, the low temperature electrooptic transmittance data at 40 K showed changes at 80 and 100 mA even though we were well below the critical current I_c of the film. We are reluctant to assign these changes exclusively to the depairing effect of the current. Although the effects of contact heating are not apparent at this temperature it could lead to similar changes.

We have also discussed the difficulties associated with carrying out a quantitative analysis of electro-optic data. The discussion of the critical-state model shows that the current and flux density distributions in the superconducting state are quite complex. It is quite difficult to analyze the results without a suitable theory of superconductivity of the cuprates. The simple simulations of the changes in the transmittance for the film on MgO and on sapphire showed what would be expected if the only effect of the current is to transfer spectral weight from the condensate to the Drude band. The simulations for the film on sapphire at 40 K compared favorably with the electro-optic data at the same temperature. The large differences between the simulations and electro-optic data at 75 K were probably a sign of heating.

It is worth mentioning, that it has been proposed that high temperature superconductors carrying a supercurrent are suitable candidates for use as optical modulators [105]. Optical modulators are key components of fiber optic communications technology. The idea is that by using pulses of current the films can easily be switched from an opaque state to a highly transmissive state. For a superconducting modulator of this kind one measure of the modulator's performance is its extinction ratio. The extinction ratio is the intensity of light transmitted in the resistive state to the intensity of light transmitted in the superconducting state. Most current commercial modulators have an extinction ratio between 6:1 and 100:1. The extinction ratios of the films in this study never exceed 1.5 if the simulations are correct. From this study it appears that such devices would offer no advantages over conventional modulators. The two main disadvantages are the small changes in transmittance induced by the current and the high critical current densities and high normal state resistivity of the cuprates which lead to sizeable heating.

REFERENCES

[1] J. G. Bednorz and K. A. Muller, *Z. Phys.* B 64, 189 (1986).

[2] T. Timusk and D. B. Tanner, *Physical Properties of High Temperature Superconductors I*, edited by D. M. Ginsberg (World Scientific, Singapore, 1989) p.339.

[3] T. Timusk and D. B. Tanner, *Physical Properties of High Temperature Superconductors III*, edited by D. M. Ginsberg (World Scientific, Singapore, 1992) p.363.

[4] R. K. Wangsness, *Electromagnetic Fields* (John Wiley and Sons, Inc., NY 1986).

[5] E. Hecht, *Optics*, second edition, (Addison-Wesley Publishing Company, Reading Massachusetts 1987).

[6] F. Wooten, *Optical Properties of Solids* (Academic Press, NY, 1972).

[7] J. D. Jackson, *Classical Electrodynamics*, third edition, (John Wiley & Sons Inc., NY, 1998).

[8] G. R. Fowles, *Introduction to Modern Optics*, second edition, (Holt, Rinehart and Winston, Inc., NY, 1975).

[9] F. Gao, Ph. D Dissertation, Department of Physics, University of Florida, Gainesville (1992)

[10] M. Born and E. Wolf, *Principles of Optics*, 7th expanded edition, (Cambridge University Press, 1999).

[11] J. Lekner, *Pure Appl. Opt.* **3**, 82 (1994).

[12] P. S. Wayland, M. E. Thomas, R. I. Joseph and M. J. Linevsky *Infrared Physics and Technology* **41**, 307 (2000).

[13] G. Bachet and R. Coulon, *Infrared Physics* **17**, 359 (1977).

[14] G. Horlik and W. K. Yeun, *Applied Spectroscopy* **32**, 38 (1978).

[15] R. L. Henry and D. B. Tanner, *Infrared Physics* **19**, 163 (1979).

[16] R. B. Sanderson and H. E. Scott, *Applied Optics* **10**, 1097 (1971).

[17] A. E. Martin, *Infrared Interferometric Spectrometers*, (Elsevier Scientific Publishing Company, NY 1980).

[18] L. Mertz, *Infrared Physics* **7**, 17 (1967).

[19] M. L. Forman, W. H. Steel, and G. A. Vanasse, *J. Opt. Soc. Am.* **56**, 59 (1966).

[20] C. D. Porter and D. B. Tanner, *International Journal of Infrared and Millimeter Waves* **4**, 273 (1982).

[21] P. Fellgett, Thesis, Univ. of Cambridge, Cambridge, England, (1951).

[22] H. Sakai, *Aspen Int. Conf. Fourier Transform Spectrosc.*, (1970) (G. A. Vanasse, A. T. Stair Jr., and D. J. Barker, eds.).

[23] J. E. Chamberlain, *The Principles of Interferometric Spectroscopy*, edited by G. W. Chantry and N. W. G Stone, Chichester Eng; NY Wiley, (1979).

[24] R. J. Birgeneau and G. Shirane, *Physical Properties of High Temperature Superconductors I*, edited by D. M. Ginsberg, (World Scientific, Singapore, 1989) p. 151.

[25] A. J. Mills and H. Monien, *Phys. Rev. Lett.* **70**, 2810 (1993).

[26] T. Timusk, *Solid State Commun.* **127**, 337 (2003).

[27] S. Oshugi, Y. Kitaika, K. Ishida and K. Asayama, *J. Phys. Soc. Jpn* **60**, 2351 (1991).

[28] D. Pavuna, *The Gap Symmetry and Fluctuations in High-T_c Superconductors*, edited by J. Bok, G. Deutscher, D. Pavuna and S. A. Wolf, (Nato ASI Series, Series B: Physics Vol. 371 Plenum Press NY 1997) p. 1.

[29] J. Zaanen, G. A. Sawatsky and J. W Allen, *Phys. Rev. Let.* **55**, 418 (1985).

[30] J. Orenstein, G. A. Thomas, A. J. Mills, S. L. Cooper, D. H. Rapkine, T. Timusk, L. F. Schneemeyer, and J. V. Waszczac, *Phys. Rev. B* **42**, 6342 (1990).

[31] S. Uchida, T. Ido, H. Takagi, T. Arima, Y. Tokura and S. Tajima, *Phys. Rev. B* **43**, 7942 (1991).

[32] S. L. Cooper, D. Reznik, A. Kotz, M. A. Karlow, R. Liu, M.V. Klein, W. C. Lee, J. Giapintzakis, D. M. Ginsberg, B. W. Veal and A. P. Paulikas, *Phys. Rev B* **47**, 8233 (1993).

[33] A. V. Puchkov, P. Fournier, T. Timusk and N. N. Kolesnikov, *Phys. Rev. Lett.* **77**, 1853 (1996).

[34] T. A. Friedmann, M. W. Rabin, J. Giapintzakis, J. P. Rice and D. M. Ginsberg *Phys. Rev. B* **42**, 6217 (1990).

[35] S. W. Tozer, A. W. Kleinsasser, T. Penney, D. Kaiser and F. Holtzberg, *Phys. Rev. Lett.* **59**, 1768 (1987).

[36] S. J. Hagen, T. W. Jing, Z. Z. Wang, J. Horvath, and N. P. Ong, *Phys. Rev. B* **37**, 7928 (1988).

[37] D. N. Basov, R. Liang, D. A. Bonn, W. N. Hardy, B. Dabrowsky, M. Quijada, D. B. Tanner, J. P. Rice, D. M. Ginsberg and T. Timusk, *Phys. Rev. Lett.* **74**, 598 (1995).

[38] C. C. Homes, D. A. Bonn, R. Liang, W. N. Hardy, D. N. Basov, T. Timusk, B. P. Clayman, *Phys. Rev. B* **60**, 9782 (1999).

[39] D. B. Romero, G. L. Carr, D. B. Tanner, L. Forro, D. Mandrus, L. Mihály, and G. P. Williams, *Phys. Rev. B* **44**, 2818 (1991).

[40] M. A. Quijada, D. B. Tanner, R. J. Kelly, M. Onellion, H. Berger and G. Margaritondo, *Phys. Rev. B* **60**, 14917 (1999).

[41] H. Liu, Ph. D dissertation, Department of Physics, University of Florida, Gainesville (1997).

[42] K. Kamarás, S. L. Herr, C. D. Porter, N. Tache, D. B. Tanner, S. Etemad, T. Venkatesan, E. Chase, A. Inam, X. D. Wu, M. S. Hegde, and B. Dutta, *Phys. Rev. Lett.* **64**, 84 (1990).

[43] G. A. Thomas, D. H. Rapkine, S. L. Cooper, S. W. Cheong, A. S. Cooper, L. F. Schneemeyer and J. V. Waszczak, *Phys. Rev. B* **45**, 2474 (1992).

[44] J. P. Falck, A. Levy, M. A. Kastner, and R. J. Birgeneau, *Phys. Rev. Lett.* **69** 1109 (1992).

[45] H. L. Dewing, and E. K. H. Salje, *Supercond. Sci. Technol.* **5**, 50 (1992).

[46] A. S. Alexandrov, A. M. Bratkovky, and N. F. Mott, *Physica C* **215**, 359 (1993).

[47] G. A. Thomas, J. Orenstein, D. H. Rapkine, M. Capizzi, A. J. Mills, R. N. Bhatt, L. F. Schneemeyer and J. V. Waszczak, *Phys. Rev. Lett.* **61**, 1313 (1988).

[48] Z. Schlesinger, R. T. Collins, F. Holtzberg, C. Field, G. Koren, and A. Gupta, *Phys. Rev. B* **41**, 11237 (1990).

[49] A. V. Puchkov, D. N. Basov, and T. Timusk, *J. Phys.: Cond. Mat.* **8** 10049 (1996).

[50] C. M. Varma, P. B. Littlewood, S. Schmitt-Rink, E. Abrahams, and A. E Ruckenstein, *Phys. Rev. Lett.* **63**, 1996 (1989).

[51] P. B. Littlewood and C. M. Varma, *J. Appl. Phys.* **69**, 4979 (1991).

[52] A. Virosztek and J. Ruvalds, *Phys. Rev. B* **42**, 4064 (1990).

[53] J. Ruvalds and A. Virosztek, *Phys. Rev. B* **43**, 5498 (1991).

[54] F. London and H. London, *Proc. R. Soc. London, Ser. A* **149**, 71 (1935).

[55] A. B. Pippard, *Proc. R. Soc. London, Ser. A* **216**, 547 (1953).

[56] M. Tinkham, *Far Infrared Properties of Solids*, edited by S. S. Mitra and S. Nudelman (Plenum, NY, 1974), p. 431.

[57] S. L. Cooper, G. A. Thomas, J. Orensten, D. H. Rapkine, A. J. Mills, S. W. Cheong, A. S. Cooper, and Z. Fisk, *Phys. Rev. B* **41**, 11605 (1990).

[58] M. Reedyk, D. A. Bonn, J. D. Garrett, J. E. Greedan, C. V. Stager, T. Timusk, K. Kamarás, and D. B. Tanner, *Phys. Rev. B* **38**, 11981 (1988).

[59] D. B. Tanner, D. B. Romero, K. Kamarás, G. L. Carr, L. Forro, D. Mandrus, L. Mihály, and G. P. Williams, *Electronic Structure and Mechanisms for High Temperature Superconductivity*, G. C. Vezolli *et al.*, editors, (Plenum Press, New York, 1991).

[60] G. A. Thomas, D. H. Rapkine, S. L. Cooper, S.-W. Cheong, and A. S. Cooper, *Phys. Rev. Lett.* **67**, 2906 (1991).

[61] F. Gao, G. L. Carr, C. D. Porter, D. B. Tanner, G. P. Williams, C. H. Hirschmugl, B. Dutta, X. D. Wu, and S. Etemad, *Phys. Rev. B* **54**, 700 (1996).

[62] F. Gao, D. B. Romero, D. B. Tanner, J. Talvacchio, and M. G. Forrester, *Phys. Rev. B* **47**, 1036 (1993).

[63] D. B. Romero, C. D. Porter, D. B. Tanner, L. Forro, D. Mandrus, L. Mihaly, G. L. Carr, and G. P Williams, Phys. Rev. Lett. **68**, 1590 (1992).

[64] D. N. Basov and T. Timusk, *Handbook on the Physics and Chemistry of Rare Earths* **31**, edited by K. A. Gschneidner. Jr., L. Eyring, and M. B. Maple, Elsevier Science B. V. (2001) p. 437.

[65] Y. Yoshinari, H. Yasouka, Y. Ueda, K. Koga, and K. Kosuge, *J. Phys. Soc. Jpn* **59**, 3698 (1990).

[66] D. S. Marshall, D. S. Dessau, A. G. Loeser, C. H. Park, Z.-X. Shen, A. Y. Matsuura, J. N. Eckstein, I. Bozovik, P. Fornier, A. Kapitulnik and W. E. Spicer, *Phys. Rev. Lett.* **76**, 4841 (1996).

[67] A. G. Loeser, Z.-X. Shen, D. S. Dessau, D. S. Marshall, C. H. Park, P. Fournier, and A. Kapitulnik, *Science* **273**, 325 (1996).

[68] S. Uchida, K. Tamasacu, and S. Tajima, *Physics. Rev. B* **53**, 14558 (1996).

[69] C. C. Homes, T. Timusk, D. A. Bonn, R. Liang, and W. N. Hardy, *Physica C* **254**, 265 1995.

[70] C. C. Homes, T. Timusk, D. A. Bonn, R. Liang, and W. N. Hardy, *Can. J. Phys.* **73**, 663 (1995).

[71] C. Bernhard, R. Henn, A. Wittlin, M. Kläser, Th. Wolf, G. Müller-Vogt, C. T. Lin, and M. Cardona, *Phys. Rev. Lett.* **80**, 1762 (1998).

[72] D. Dijkkamp, T. Venkatesan, X. D. Wu, S. A. Shaheen, N. Jisrawi, Y. H. Min-Lee, W. L. McLean and M. Croft, *Appl. Phys. Lett.* **51**, 619 (1987).

[73] B. F. Cole, G.-C. Liang, N. Newman, K. Char, G. Zaharchuk and J. S. Martens, *Appl. Phys. Lett.* **61**, 1727 (1992).

[74] http://www.guildoptics.com/properties.html

[75] Yu. A. Boĭkov, T. Claeson, and D. Érts, *Phys. Solid State* **40**, 183 (1998).

[76] T. R. Yang, S. Perkowitz, G. L. Carr, R. C. Budhani, G. P. Williams, and C. J. Hirschmugl, *Applied Optics* **29**, 332 (1990).

[77] K. Clausen, W. Hayes, J. E. Macdonald, R. Osborn, P. G. Schnabel, M. T. Hutchings and A. Magerl, *J. Chem. Soc.* **83**, 1109 (1987).

[78] M. M. Sinha, P. Ashdhir, H. C. Gupta, and B. B. Tripathi, *Phys. Stat. Sol. b* **191**, 101 (1995).

[79] S. Mochizuki, *Phys. Stat. Sol. b* **114**, 189 (1982).

[80] S. Mochizuki, *Phys. Stat. Sol. b* **128**, 23 (1985).

[81] F. Marabelli and P. Wachter, *Phys. Rev. B* **36**, 1238 (1987).

[82] E. V. Loewenstein, *J. Opt. Soc. Am.* **51**, 108 (1961).

[83] S. Roberts, and D. D. Coon, *J. Opt. Soc. Am.* **52** 1023 (1962).

[84] E. E. Russell, and E. E. Bell, *J. Opt. Soc. Am.* **57** 543 (1967).

[85] E. V. Loewenstein, D. R. Smith, and R. L. Morgan, *Appl. Opt.* **12**, 398 (1973).

[86] A. S. Barker, Jr., *Phys. Rev.* **132**, 1474 (1963).

[87] F. Gervais, and B. Piriou, *J. Phys. C: Solid State Phys.* **7**, 2374 (1974).

[88] M. E. Thomas, S. K. Andersson, R. M. Sova, and R. I. Joseph, *Infrared Physics and Technology* **39**, 235 (1998).

[89] E. H. Brandt, and M. Indenbom, *Phys. Rev. B* **48**, 12893 (1993).

[90] E. Zeldov, J. R. Clem, M. McElfresh, and M. Darwin, *Phys. Rev. B* **49** 9802 (1994).

[91] M. E. Gaevski, A. V. Bobyl, D. V. Shantsev, Y. M. Galperin, T. H. Johansen, M. Baziljevich, H. Bratsberg, and S. F. Karmanenko, *Phys. Rev. B* **59**, 9655 (1999).

[92] Ch. Jooss, J. Albrecht, H. Kuhn, S. Leonhardt, and H. Kronmüller, *Rep. Prog. Phys.* **65**, 651 (2002).

[93] I. Pethes, B. Sas, G. Kriza, F. Portier, F. I. B Williams, K. Vad, and S. Mészáros, *Synthetic Metals* **120**, 1013 (2001).

[94] S. R. Currás, J. Viña, M. Ruibal, M. T. González, M. R. Osorio, J. Maza, J. A Veira, and F. Vidal, *Physica C* **372–376**, 1095 (2002).

[95] B. Roas, L. Schultz, and G. Saemann-Ischenko, *Phys. Rev. Lett.* **64** 479 (1990).

[96] J. C. Campuzano, *private communication.*

[97] J. Ngai, J. Wei, F. Chen, and D. Perovic, *March Meeting 2003 Bulletin of the American Physical society* **part II**, Austin, Tx p. 372.

[98] A. Anthore, H. Pothier, and D. Esteve, *Phys. Rev. Lett* **90**, 127001-1 (2003).

[99] K. D. Usadel, *Phys. Rev. Lett* **25**, 507 (1970).

[100] K. Karrai, E. J. Choi, F. Dunmore, S. Liu, H. D. Drew, Q. Li, D. B Fenner, Y. D. Zhu, and F. C. Zhang, *Phys. Rev. Lett.* **69**, 152 (1992).

[101] K. Karrai, E. Choi, F. Dunmore, S. Liu, X. Ying, Q. Li, T. Venkatesan, H. D. Drew, and D. B. Fenner, *Phys. Rev. Lett.* **69**, 355 (1992).

[102] B. Parks, S. Spielman, J. Orenstein, D. T. Nemeth, F. Ludwig, J. Clarke, P. Merchant, and D. J. Lew, *Phys. Rev. Lett.* **74**, 3265 (1995).

[103] A. M. Gerrits, M. E. J. Boonman, A. Wittlin, P. J. M. van Bentrum, V. H. M. Duijn, and A. A. Menovsky, *Phys. Rev. B* **51**, 12049 (1995).

[104] R. Mallozzi, J. Orenstein, J. N. Eckstein, and I. Bozovic, *Phys. Rev. Lett.* **81**, 1485 (1998).

[105] W. J. Cottrell, T. G. Ference, and K. A. Puzey, *Solid State Communications* **120**, 479 (2001).

BIOGRAPHICAL SKETCH

Andrew Wint was born in Clarks Town, in the parish of Trelawny in Jamaica. He is the only child of Trevor and Ethnie Wint. His early years were spent at First Hill All Age School, before he was admitted to Munro College after passing the national Common Entrance exams. His high school career began inauspiciously, as after the first two years at Munro he was expelled after becoming diabetic. In 1987 he got admitted to Cornwall College where he excelled in the sciences, under the tutelage of his math teacher, Bevin Debruin. After taking the University of Cambridge A-level exams he attended the University of the West Indies (UWI) as an undergraduate in 1992. He graduated from the UWI with a BSc in mathematics and physics in 1995. Three years later he was accepted at the University of Florida to pursue a Ph.D in physics. In the fall of 1999 he joined professor David Tanner's research group where he researched the optical properties of high T_c superconductors.

I certify that I have read this study and that in my opinion it conforms to acceptable standards of scholarly presentation and is fully adequate, in scope and quality, as a thesis for the degree of Doctor of Philosophy.

David B. Tanner, Chairman
Professor of Physics

I certify that I have read this study and that in my opinion it conforms to acceptable standards of scholarly presentation and is fully adequate, in scope and quality, as a thesis for the degree of Doctor of Philosophy.

Arthur F. Hebard
Professor of Physics

I certify that I have read this study and that in my opinion it conforms to acceptable standards of scholarly presentation and is fully adequate, in scope and quality, as a thesis for the degree of Doctor of Philosophy.

Kevin Ingersent
Associate Professor of Physics

I certify that I have read this study and that in my opinion it conforms to acceptable standards of scholarly presentation and is fully adequate, in scope and quality, as a thesis for the degree of Doctor of Philosophy.

Christopher J. Stanton
Professor of Physics

I certify that I have read this study and that in my opinion it conforms to acceptable standards of scholarly presentation and is fully adequate, in scope and quality, as a thesis for the degree of Doctor of Philosophy.

Paul H. Holloway
Distinguished Professor of Materials
Science and Engineering

This thesis was submitted to the Graduate Faculty of the Department of Physics in the College of Liberal Arts and Sciences and to the Graduate School and was accepted as partial fulfillment of the requirements for the degree of Doctor of Philosophy.

December 2004

Dean, Graduate School

A SEARCH FOR AN INFRARED ELECTRO-OPTIC EFFECT IN THIN HIGH TEMPERATURE SUPERCONDUCTING FILMS

Andrew C. Wint
(352) 392–4715
Department of Physics
Chair: David B. Tanner
Degree: Doctor of Philosophy
Graduation Date: December 2004

Optical modulators are important elements in fiber optic communications. Fiber optic cables have been known to be superior to conventional cables as conduits of information. A modulator becomes more or less transparent to light when driven by an external current.

We have investigated the feasibility of using superconducting films as modulators of infrared light. This investigation has led us to the conclusion that the use of such films to build such a device, is not a feasible prospect at this time. There are various practical problems associated with these proposed modulators which are unavoidable. It was also shown that optical modulators based on superconductors would offer no advantage over conventional modulators which are currently in operation.